1 HLA-E and NKG2A Mediate Resistance to *M. bovis* BCG Immunotherapy in Non-Muscle-Invasive

2 **Bladder Cancer**

- 3
- 4 D. Ranti^{1,2,3,4,5*}, H. Yu^{1,2,3,4,5,11*}, Y.A. Wang^{1,2,3,4,5}, C. Bieber^{1,2,3,4,5}, T. Strandgaard^{6,7}, B. Salomé^{1,2,3,4}, Sean
- Houghton⁸, J. Kim⁸, H. Ravichandran⁸, I. Okulate^{1,2,3,4,5}, E. Merritt^{3,9}, S. Bang⁹, A. Demetriou^{1,2,3,4,5}, Z. 5
- Li^{1,2,3,4}, S. V. Lindskrog^{6,7}, D.F. Ruan^{1,2,3,4}, J. Daza^{1,2,3,4,5}, R. Rai⁴, E. Hegewisch-Solloa¹⁰, E.M. Mace¹⁰, R., 6
- Fernandez-Rodriguez^{2,4}, S. Izadmehr^{3,9}, G. Doherty^{11,12}, A. Narasimhan^{11,12}, A.M. Farkas^{3,4,11}, P. Cruz-7
- Encarnacion^{1,2}, S. Shroff^{7,13}, F. Patel^{3,14}, M. Tran^{3,4,11}, S.J. Park^{1,2,3,4}, J. Qi¹⁵, M. Patel¹⁵, D. Geanon¹⁵, G. 8
- 9 Kelly¹⁵, R.M.de Real¹⁵, B. Lee¹⁵, K. Nie¹⁵, S. Miake-Iye¹⁵, K. Angeliadis¹⁵, E. Radkevich¹⁵, T.H. Thin¹⁶, M. Garcia-Barros¹⁶, H. Brown¹⁶, B. Martin¹⁶, A. Mateo¹⁶, A. Soto¹⁶, R. Sussman¹⁶, S. Shiwlani¹⁶, S. Francisco-10
- Simon¹⁶, K.G. Beaumont^{9,13}, Y. Hu¹⁵, Y-C. Wang^{7,13}, L. Wang⁹, R.P. Sebra^{9,13,17}, S. Smith¹⁸, M. Skobe^{2,4}, E. 11
- Clancy-Thompson¹⁹, D. Palmer¹⁹, S. Hammond¹⁹, B. D. Hopkins¹⁵, P. Wiklund⁵, J. Zhu^{9,13}, J.J. Bravo-12
- 13 Cordero^{11,12}, R. Brody¹⁶, Hopkins, B., Z. Chen^{1,3,15}, S. Kim-Schulze^{1,3,15}, L. Dyrskjøt^{6,7}, O. Elemento⁸, A.
- Tocheva^{3,9}, W-M. Song⁹, N. Bhardwaj^{3,4,11}, M.D. Galsky^{4,11}, J.P. Sfakianos^{5#} & A. Horowitz^{1,2,3,4#} 14
- 15
- 16 ¹Department of Immunology and Immunotherapy, Icahn School of Medicine at Mount Sinai, New York, 17 NY, USA
- 18 ²Department of Oncological Sciences, Icahn School of Medicine at Mount Sinai, New York, NY, USA
- 19 ³The Marc and Jennifer Lipschultz Precision Immunology Institute, Icahn School of Medicine at Mount 20
- Sinai, New York, NY, USA
- 21 ⁴Tisch Cancer Institute, Icahn School of Medicine at Mount Sinai, New York, NY, USA
- 22 ⁵Department of Urology, Icahn School of Medicine at Mount Sinai, New York, NY, USA
- 23 ⁶Department of Molecular Medicine, Aarhus University Hospital, Aarhus, Denmark
- 24 ⁷Department of Clinical Medicine, Aarhus University, Aarhus, Denmark
- 25 ⁸Caryl and Israel Englander Institute for Precision Medicine, Weill Cornell Medicine, New York, NY, USA
- 26 ⁹Department of Genetics and Genomic Sciences, Icahn School of Medicine at Mount Sinai, New York, NY,
- 27 USA
- 28 ¹⁰Department of Pediatrics, Vagelos College of Physicians and Surgeons, Columbia University, New York 29 NY, USA
- 30 ¹¹Division of Hematology and Medical Oncology, Department of Medicine, Icahn School of Medicine at
- 31 Mount Sinai, New York, NY, USA
- 32 ¹²Microscopy and Advanced Bioimaging Core, Icahn School of Medicine at Mount Sinai, New York, NY, 33 USA
- 34 ¹³Icahn Institute for Data Science and Genomics Technology, Icahn School of Medicine at Mount Sinai, 35 New York, NY, USA
- 36 ¹⁴Department of Microbiology, Icahn School of Medicine at Mount Sinai, New York, NY, USA
- 37 ¹⁵Human Immune Monitoring Center, Icahn School of Medicine at Mount Sinai, New York, NY, USA
- 38 ¹⁶Department of Pathology, Molecular and Cell-Based Medicine, Icahn School of Medicine at Mount Sinai,
- 39 New York, NY
- 40 ¹⁷Black Family Stem Cell Institute, Icahn School of Medicine at Mount Sinai, New York, NY, USA
- 41 ¹⁸Center for Inflammation research and Translational Medicine, Brunel University London, London, UK
- 42 ¹⁹AstraZeneca, Oncology R & D Unit, Gaithersburg, Maryland, USA
- ²⁰Department of Physiology and Biophysics, Weill Cornell Medicine, New York, NY, USA 43
- 44 * These authors contributed equally
- 45 # Co-Senior author
- 46
- 47 **Running title.** HLA-E and NKG2A in BCG Resistance 48

- 49 Keywords. Non-muscle-invasive bladder cancer; BCG-unresponsive; NK cells;
- 50 Immunotherapy.
- 51
- 52

53 Corresponding Author:

- 54 Amir Horowitz, PhD
- 55 Associate Professor of Immunology & Immunotherapy and Oncological Sciences
- 56 Lipschultz Precision Immunology Institute and Tisch Cancer Institute
- 57 Icahn School of Medicine at Mount Sinai
- 58 1425 Madison Ave., Box 1630
- 59 New York, New York 10029
- 60 Tel: (212) 659-9391 | Fax: (646) 537-9577
- 61 Email: <u>amir.horowitz@mssm.edu</u>
- 62
- **63** John P. Sfakianos, MD
- 64 Associate Professor of Urology
- 65 Icahn School of Medicine at Mount Sinai
- 66 1425 Madison Ave., L6-58, Box 1272
- 67 New York, New York 10029
- 68 Tel: (212) 659-9375
- 69 Email: john.sfakianos@mountsinai.org
- 70
- 71
- 72
- 73 Conflict of Interest Disclosure Statement: The authors declare no potential conflicts of interest.
- 74
- 75 Word Count (excluding methods and references):
- 76 Fig. Count: 7
- 77 Table Count: 1
- 78

79 Abstract:

80	Mycobacterium bovis Bacillus Calmette-Guerin (BCG) is the primary treatment for non-muscle-
81	invasive bladder cancer (NMIBC), known to stimulate inflammatory cytokines, notably interferon
82	(IFN)-y. We observed that prolonged IFN-y exposure fosters adaptive resistance in recurrent
83	tumors, aiding immune evasion and tumor proliferation. We identify HLA-E and NKG2A, part of
84	a novel NK and T cell checkpoint pathway, as key mediators of resistance in BCG-unresponsive
85	NMIBC. IFN-γ enhances HLA-E and PD-L1 expression in recurrent tumors, with an enrichment
86	of intra-tumoral NKG2A-expressing NK and CD8 T cells. CXCL9 ⁺ macrophages and dendritic
87	cells and CXCL12-expressing stromal cells likely recruit CXCR3/CXCR4-expressing NK and T
88	cells and CXCR7 ⁺ HLA-E ^{HIGH} tumor cells. NK and CD8 T cells remain functional within BCG-
89	unresponsive tumors but are inhibited by HLA-E and PD-L1, providing a framework for combined
90	NKG2A and PD-L1 blockade strategy for bladder-sparing treatment of BCG-unresponsive
91	NMIBC.
92	
93	
94	
95	
96	
97	
98	
99 100	
100	
101	
102	
104	
105	
106	
107	
108	

109 Introduction

110

111 Intravesical Mycobacterium bovis Bacillus Calmette-Guerin (BCG) is the only FDA-approved, first-line 112 treatment for high risk non-muscle-invasive bladder cancer (NMIBC), and is hypothesized to act in part via 113 the release of inflammatory cytokines, notably interferon (IFN)- γ^{-1} . Unfortunately, tumor recurrence 114 following BCG treatment is common, with local recurrence rates between 32.6 to 42.1% and progression 115 rates between 9.5 to 13.4%². Radical cystectomy is the only definitive treatment option for BCG-116 unresponsive disease, leaving patients at high risk for complications and the need for urinary diversion 117 which can lead to diminished quality of life ^{3,4}. Currently, there is substantial interest and numerous ongoing 118 clinical trials to identify novel therapeutic options for BCG-unresponsive NMIBC.

119 Despite the use of BCG as the first-line immunotherapy for NMIBC for over 40 years, the 120 mechanisms underlying resistance to BCG's therapeutic benefits are poorly understood. This lack of 121 understanding has further hindered progress in developing novel approaches to treat tumors resistant to 122 BCG. The six-dose weekly induction regimen was devised anecdotally based on rudimentary urine studies 123 performed in the 1970's ⁵. Only a single dosing study has ever been performed to assess the immunologic 124 response with this dosing regimen, which concluded that six doses stimulated an immune response, but did 125 not investigate the ramifications of the magnitude nor the duration of that immune response ⁶. Contributing 126 to the difficulty in predicting BCG response is the variety of immune lineages implicated in both its success 127 and failure, including neutrophils, monocytes, macrophages, dendritic cells (DCs), T cells, and natural killer 128 (NK) cells ⁷.

129 Adaptive immune resistance, in which cancers are recognized by immune cells, but accommodative 130 changes prevent effective clearance, is an important mechanism of the apeutic resistance 8 . IFN- γ has been 131 shown to have both pro- and anti-tumorigenic functions across an array of tumor types⁹. The equilibrium 132 established by IFN- γ signaling may be critical in preventing therapeutic resistance. In melanoma and lung 133 cancer, dysfunctional and overactive IFN- γ signaling is known to drive T cell inhibition via upregulation 134 of PD-L1 10 . In muscle-invasive and metastatic urothelial carcinoma, IFN- γ associates with improved as 135 well as poor responses to PD-1/PD-L1 blockade and exists as part of a balance (coined 2IR score) between 136 pro- and anti-tumorigenic pathways expressed in the TME¹¹. The impact of long-term intravesical BCG, 137 which drives chronic immune stimulation via IFN-y production, and its role in immune dysregulation and 138 exhaustion in BCG unresponsive NMIBC is emerging but still unclear ^{12, 13}.

Previous work comparing BCG-unresponsive to treatment-naïve tumors showed a significant increase in PD-L1 expression, but only in a minority of unresponsive samples ¹⁴. Immunotherapeutic strategies, especially those engaging the PD-1/PD-L1 axis to unleash exhausted immune cells, have modestly improved NMIBC treatment. Unfortunately, response rates to PD-1 blockade monotherapies in
 NMIBC remain low, at ~19% durable response ^{15, 16, 17, 18}. Further, PD-L1 expression levels alone have failed
 to accurately predict response to immunotherapy in NMIBC, suggesting that alternative mechanisms of
 immune suppression are engaged ¹⁹.

146 The HLA-E/NKG2A axis has been identified as a potent immune checkpoint regulating both CD8 147 T and NK cells ^{20,21,22,23,24}. Abrogation of HLA-E interactions with NKG2A on NK cells increased effector 148 activity against tumor cells and potentiated anti-tumor function. Further, blocking NKG2A on CD8 T cells 149 in a murine model increased tumor vaccine response, even in a PD-1 resistant setting ^{20,22}. Additionally, the 150 combination of anti-NKG2A antibody (monalizumab) and antiPD-L1 antibody (durvalumab) has been 151 studied in a Phase 2 clinical trial in patients with nonresectable, stage III NSCLC. The combination 152 demonstrated an objective response rate of 35% vs 17.9% with durvalumab alone, as well as improved 153 progression-free survival (PFS) with durvalumab and monalizumab (72.7%) compared to durvalumab alone 154 (33.9%)²⁵.

155 Most recently, BCG was shown to directly infect a proportion of bladder tumor cells in NMIBC 156 patients driving impairment in autophagy flux resulting in downregulation of HLA class I expression along 157 with a shift towards epithelial-to-mesenchymal transitioning (EMT) by BCG-infected tumor cells ²⁶. In a 158 cohort of BCG-treated NMIBC patients with tumor recurrence, the authors observed that abundance of 159 class I HLA-negative tumor cells associated with disease progression and metastasis and overall survival. 160 This study highlighted two different tumor cell types within BCG-unresponsive settings and suggested that 161 a tumor phenotype defined by high HLA class I expression correlated with improved long-term survival 162 post-cystectomy.

163 In this study, we confirm the presence of both tumor cell phenotypes but focus on their interactions 164 with stromal and immune cells. We present a novel mechanism of resistance, whereby HLA class I-positive 165 tumor cells are activated in response to NK and CD8 T cell-derived IFN-γ and recruited to CXCL12-166 expressing stromal-rich regions of the tumor where myeloid cells, regulatory T cells (Tregs), and immune 167 effector cells (NK, CD8 T cells) are enriched. Consequently, class I HLA-negative tumor cells can subvert 168 immune cell trafficking. We pose a novel hypothesis that BCG more broadly induces changes in the bladder 169 tumor microenvironment (TME), promoting expression of NKG2A and PD-1 on CD8⁺ T cells, NKG2A on 170 NK cells, and HLA-E, PD-L1, and CXCR7 on recurring, cytokine-activated tumor cells, and these 171 phenotypic changes are mechanistically linked to treatment resistance and immune evasion by recurring 172 tumors. This study investigates HLA-E and NKG2A as a novel axis of resistance induced by chronic 173 inflammation and provides a mechanistic framework for a bladder-sparing combination immunotherapy 174 strategy of NKG2A and PD-L1 blockade for overcoming resistance to BCG immunotherapy for treating 175 high-grade NMIBC.

176

177 <u>Results</u>

178

179 Clinical cohort description.

Cohort descriptions of patient samples used for the experiments below are described in Table 1. Patient samples were collected and processed at The Mount Sinai Hospital, and the validation cohort was collected and processed at Aarhus University Hospital, Denmark. Median patient age ranged from 64 to 70.7 years old; median months to recurrence ranged from 1.7 to 2.9 months; median months to progression ranged from 4.43 to 23.28 (**Table 1**).

185

186 IFN-γ initiates adaptive resistance including increased tumor expression of HLA-E and PD-L1.

187 To investigate potential mechanisms underlying BCG resistance in NMIBC, we used tumor 188 specimens from BCG-naïve patients, prior to initiating induction intravesical BCG therapy and BCG-189 unresponsive tumors, with a recurrence after at least an induction course of intravesical BCG, collected 190 from a prospective cohort of NMIBC patients. Targeted in situ hybridization and mRNA sequencing and 191 gene-set enrichment analysis (GSEA) comparing BCG-unresponsive tumors to pre-treatment timepoints 192 were performed (Fig. 1A)²⁷. Significant gene sets are shown ranked by their normalized enrichment score 193 (NES) (Fig. 1A, Supplemental Table S1). The top enriched gene-sets comparing BCG-unresponsive to 194 BCG-naïve tumors (n=36) included, but were not limited to, IFN-γ response, cytotoxic lymphocytes, T cell 195 checkpoint modulation, tumor inflammation, TH1 response, and lymphocyte trafficking (Supplemental 196 **Table S1**). Of note, the "Lymphocyte trafficking" pathway was largely driven by a combination of genes 197 encoding activating cytokines and receptors as well as inhibitory immune checkpoint genes (PDCD1 (PD-198 1), CD274 (PD-L1), PDCD1LG2 (PD-L2), CTLA4, TIGIT, KLRC1 (NKG2A), HLA-E) indicating a balance 199 between antitumor and pro-tumorigenic features in the TME. Gene sets downregulated in the BCG-200 unresponsive state and upregulated in the BCG naïve state included TGF beta signaling, hypoxia, 201 peroxisome, oxidative phosphorylation, P53 pathway, DNA repair, and stress toxicity (Fig. 1A).

To better understand the inflammatory state observed in BCG-unresponsive tumors, we used cellfree urine supernatants from a prospective cohort of BCG-treated NMIBC patients and performed an analysis using the OLINK ProteomicsTM "inflammation" panel, a 92-analyte protein proximity extension assay, to profile urine cytokines reflective of the urothelial microenvironment ^{28, 29}. Independent of clinical response to BCG therapy, all patients experienced elevated cytokine levels in their urine. Significantly upregulated cytokines of interest at the sixth dose compared with the BCG-naïve state included IFN- γ , Flt3L, IL2RB, CCL8, CCL13, CCL19, CCL23, CXCL1, CXCL9, CXCL10, CXCL11, and TWEAK (**Fig.** 209 **1B**; all p<0.05). Importantly, urine cytokine levels kept increasing with each consecutive dose of BCG, 210 where even after a six-week treatment interruption (time of first cystoscopy,) urine cytokine levels never 211 equilibrated back to baseline, although the differences were not significant. The inflammatory signature 212 was validated in an independent cohort, "Aarhus" (Aarhus University Hospital, Denmark), consisting of 213 BCG-treated patients with long term clinical follow-up. Urine samples from 66 patients were collected at 214 the BCG-naïve time point and compared to patient-matched urine samples collected within four months 215 after completion of BCG induction course. CXCL9, CXCL10, CXCL11, CCL19, and CCL23 had lasting 216 upregulation at the post-BCG timepoint (p < 0.05) (Fig. 1C). Additionally, urinary protein profiles at these 217 timepoints were compared between responsive and unresponsive patients considering whether visible 218 bladder tumors were present at the time of urine sampling (Fig. 1D). With exception of CXCL5, when 219 assessing urine from BCG-unresponsive patients (before the start of BCG induction therapy) we identified 220 significantly elevated levels of cytokines and chemokines only when tumors were present at time of 221 sampling, where the presence of CCL3, CCL20, CXCL11, IL-8, MMP7 and MMP12 were attributable to 222 bladder tumors rather than in response to BCG. Patients unresponsive to BCG showed a distinct urinary 223 protein profile after BCG treatment with a greater magnitude of inflammatory cytokine and chemokine 224 production as well as Caspase-8 (a marker of apoptosis) and TGF- β 1 in its pre-processed inactive state 225 interacting with its latency associated peptide (LAP) (Fig. 1D).

226 To better understand the effects of IFN- γ on recurring bladder tumors, primary tumor cells from 227 NMIBC patients (n=10) and urothelial tumor lines were cultured for 24 hours in the presence or absence of 228 recombinant human IFN- γ (Fig. 1E) and HLA-E and PD-L1 expression were measured via fluorescence 229 flow cytometry. Tumor cells expressed significantly higher levels of PD-L1 and HLA-E following 230 stimulation with IFN- γ , which was also observed across the collection of bladder tumor lines (n=11) (Fig. 231 1E). We saw no effects of IFN-y on wild type (WT) K562 tumors (lack expression of HLA class I, including 232 HLA-E). HLA-E-stably-transduced K562 cells were used as a positive control for maximal HLA-E 233 expression. Overall, these results suggest adaptive resistance by recurring tumor cells after BCG therapy 234 that respond to IFN- γ by increasing HLA-E and PD-L1 expression and in a microenvironment replete with 235 immune effector cells.

236

237 Selective upregulation of tumor HLA-E in regions near NKG2A-expressing NK and CD8 T cells

To validate *in situ* hybridization *mRNA* analyses and to better understand the spatial relationship between tumor cells and tumor infiltrating lymphocytes (TILs), we performed multiplex imaging analyses using both immunofluorescence (IF) as well as immunohistochemistry (IHC) with whole slide scanning for targeted high-resolution analyses on a cohort BCG naïve (N=17) and BCG unresponsive (N=24) NMIBC patients (**Fig. 2**). We first performed a subset analysis of NMIBC sections (N=4) using a PhenoCyclerTM

243 (formerly CODEX) imaging system (Akoya Biosciences). Representative imaging for one BCG-244 unresponsive NMIBC section highlights \$100A4⁺ tumor cells intermixed with stroma (Vimentin) (Fig. 245 **2A**). We observed a large abundance of NKp46⁺ NK cells and CD8 T cells with variegated expression of 246 NKG2A and/or PD-1 (Figs. 2B and 2C). While the analysis was underpowered for robust analyses, the data 247 demonstrated substantially greater abundance of NKG2A-expressing NK and CD8 T cells in BCG-248 unresponsive sections and in regions of tumor tissue with high HLA-E expression by tumor cells and 249 stroma. 250 To validate the observation, we stained the cohort of 41 NMIBC sections by multiplexed IHC for Pan-251 cytokeratin (pan-CK), HLA-E, CD3, and NKG2A (Fig. 2D). Among tumors from the cohort, we analyzed 252 840,348 tumor cells in total (277,315 for BCG-naïve and 563,033 for BCG-unresponsive). We used Halo 253 digital pathology software (Indica Labs, Albuquerque, NM) to annotate cell lineages, and to measure tumor 254 HLA-E expression within the for density and spatial relationships with stromal and T/NK cell infiltration 255 and proximity (Fig. 2E-2I). Here, we confirmed that HLA-EBRIGHT tumor cells were significantly more 256 abundant in BCG-unresponsive tumors (p=0.0002) and represented 43.6%% of total tumor cells compared

- 257 to 10.3% in BCG-naïve tumors (Fig. 2G). Further, we identified NKG2A⁺ CD3⁻ NK cells and NKG2A⁺
- CD3⁺ T cells (Fig. 2H) and determined they were in significantly closer proximity to HLA-E^{BRIGHT} tumor 258
- cells (p<0.00001)(Fig. 2I). Finally, we performed a proximity ligation assay by immunofluorescence using 260 antibodies targeting HLA-E and NKG2A to quantify the numbers of interactions between NKG2A⁺
- 261 NK/CD8 T cells and HLA-E⁺ tumor cells and found a significantly greater number of interactions in BCG-
- 262 unresponsive tumors (p = 0.009) (Fig. 2J and 2K).
- 263

259

264 Chronic activation of tumor-infiltrating NK and CD8 T cells in BCG-unresponsive tumors

265 To better understand the composition of the tumor microenvironment and to characterize the 266 potential drivers of adaptive resistance, single-cell RNA sequencing (scRNA-seq) of nine tumors (BCG-267 naïve (n=3) and unresponsive (n=6)), was performed. In total, 65,324 tumor-derived cells containing 26,520 268 gene features passed quality control and were used for subsequent analyses, with a median of 958 genes 269 detected per cell.

270 Twenty-two identifiable cell populations, including CD4 and CD8A T cells, regulatory T cells 271 (Tregs), NK cells, dendritic cells (DCs), monocytes and macrophages, granulocytes, B cells, plasma cells, 272 and nonhematopoietic stromal, and tumor cells were identified after graph-based clustering (Fig. 3A and 273 **3B**, **Supplementary Table S3 and S4**). To identify the cell origin(s) of IFN- γ and related pro-inflammatory 274 gene signatures, we examined the expression of *IFNG* in each of the cell populations. NK cells, CD8 T 275 cells, and a subset comprised of both CD4 and CD8 T cells defined by cell cycle genes (T cell-cycle) 276 demonstrated the highest levels of IFNG expression among all cell clusters and had distinct IFN-y^{high} cell

populations (Extended data Fig. S1A). Additionally, we profiled the median gene expression across all
major canonical checkpoint receptors and observed variegated expression on T cell subsets. However,
tumor-derived NK cells mostly expressed *KLRC1*, and to a lesser extent *HAVCR2* (Tim3) and *TIGIT*(Extended data Fig. S1B).

281 To better understand the functional significance associated with NKG2A expression, we stratified 282 NK cells, CD8 T and T cell-cycle cells by low and high *KLRC1* expression and performed a differential 283 expression of genes (DEG) analysis (Fig. 3C). Our analysis revealed a balance between cytokine and 284 cytolytic activity and expression of inhibitory checkpoint receptors. KLRC1^{high} NK cells expressed 285 significantly higher CCL5, CSF1, XCL2, IL2RB, and FCER1G, but additionally expressed higher levels of 286 TIGIT. Tumor-infiltrating NK cells also expressed significantly higher levels of CD2, ITGA1 (CD49a), 287 ITGAE (CD103) and RGS1 suggesting they are tissue-resident. Additionally, we observed that KLRC1^{high} 288 CD8 T cells expressed elevated levels of CCL3, CSF1, GNLY, GZMA, GZMB, and PRF1 (perforin), but 289 they additionally expressed higher levels of CTLA4, ENTPD1 (CD39), HAVCR2, LAG3, KIR2DL4 and 290 TIGIT. KLRC1^{high} T cell-cycle cells showed significant upregulation in CCL5, CSF1, CXCL13, NKG7, 291 GNLY, GZMA, GZMB, but additionally expressed LAG3, KIR2DL4, and TIGIT. Collectively, the data 292 suggest that BCG therapy drives strong immune activation and that many repeated doses of treatment 293 sustain activation over prolonged period driving upregulation of inhibitory checkpoint pathways.

294

Functionally distinct states of bladder tumor-derived NK and CD8 T cells in BCG-unresponsiveNMIBC

297 NK cells are very heterogenous and remain poorly described in solid tumors with virtually nothing 298 known in human bladder cancer. We performed unbiased clustering on all NK cells to derive five major 299 clusters (Fig. 3D), which were divided across conventional definitions of CD56^{bright} and CD56^{dim} NK cells 300 (Fig. 3E). A pathway analysis revealed significant enrichment in CD56^{bright} NK cells for genes involved in 301 metabolism, IL-2 signaling, and immune 'stress' (ROS and DNA repair) (Fig. 3F). Conversely, CD56^{dim} 302 NK cell enriched pathways included response to TNF α and IFN α and apoptosis, MAPK activity but also 303 reflect immune 'stress' (hypoxia, complement regulation). Building on two recent seminal resources for transcriptional reference mapping of human NK cells in solid tissues^{30, 31}, we integrated the newly defined 304 305 gene signatures to annotate 'functional states' to bladder tumor-derived NK cells (Fig. 3G, Extended data 306 Fig. S2). Our analysis confirmed that clusters 1 and 2 are very similar to Group 2 typical CD56^{bright} NK 307 cells, and cluster 5 strongly correlates with Group 1 "stressed" CD56^{bright} NK cells, described by Netskar et al.³⁰. Collectively clusters 1,2, and 5 reflecting Groups 1 and 2 NK cells represent ~50% of the total 308 309 tumor-infiltrating NK cells. Additionally, the remaining fraction of CD56^{dim} NK cells were distributed

among groups 3-6 NK cells, defined by effector functions (Gr. 3), adaptive NKG2C⁺ NK cells (Gr. 4),
activated (Gr. 5), and typical (Gr. 6) NK cells.

312 We similarly applied gene signatures for NK1, NK2, and NK3 subsets as recently demonstrated by Rebuffet et al^{31, 32}, and these definitions more closely reflect a developmental or ontogeny trajectory of NK 313 314 cells across human tissues, NK1 and NK-intermediate cells represent immature CD56^{bright} NK cells and 315 NK3 cells include terminally mature and adaptive NK cells (Extended data Fig. S2). Our comparative 316 analysis revealed an enrichment of NK-intermediate cells representing the original clusters 1 and 2, and 317 NK1B cells representing the original clusters 3 and 4. Both NK1B and NK-intermediate signatures were 318 shared among the original cluster 5 suggesting transitional properties of this NK cell subset. Finally, we 319 profiled tumor-infiltrating NK cells according to the six functional states (Gr. 1-6) (and CD8 T cells and T cell-cycle cells according to KLRC1^{+/-}) for expression of tissue residency genes as well as 320 321 cytokines/chemokines and cytokine/chemokine receptors to understand how NK cells and T cells are 322 trafficking to the bladder, and we confirmed they are functionally competent (Fig. 3H and 3I). We also 323 observed clear evidence suggesting functional specialization within the NK cells and within the T cells. For 324 instance, KLRC1⁺ CD8 T cells express high levels of IL2RB, TNFRFS9 (4-1BB), CSF1 and FASLG 325 compared to their KLRC1⁻ counterparts. However, KLRC1⁻ CD8 T cells expressed higher levels of IFNG, 326 and FLT3LG (Fig. 3I).

327

BCG-unresponsive tumors are characterized by a segregated microenvironment, where activated HLA-E^{HIGH} tumor cells are recruited to stromal regions replete with immune cells.

330 We next sought to understand the composition of tumor cells in tumors from both treatment-naïve 331 (N=14,852) and BCG-unresponsive (N=29,858) NMIBC patients. UMAP clustering of scRNAseq analysis 332 revealed seven major subsets of tumor cells (Fig. 4A), where clusters B1 and B3 had significantly higher 333 HLA-E expression (Fig. 4B) and were significantly more responsive to cytokines and inflammatory signals 334 (Fig. 4C). We profiled tumor clusters for expression of known inhibitory and activating ligands as well as 335 for cytokines/chemokines and cytokine/chemokine receptors (Figs. 4D and 4E). Importantly, of all 336 chemokine receptors, we observed that HLA-E^{HIGH} bladder tumor cells had significantly higher ACKR3 337 (CXCR7) expression, and pseudo-bulking the scRNAseq data revealed that HLA-E and CXCR7 tumor 338 expression were strongly correlated (Fig. 4F). Additionally, we profiled the abundance of each tumor 339 cluster according to BCG treatment status and observed cluster B2 was uniquely enriched in BCG-naïve 340 tumors (Fig. 4G). The other tumor clusters were either evenly distributed between naïve and unresponsive 341 tumors or they were disproportionately skewed towards unresponsive.

Collectively, our analyses of NK cells, T cells and tumor cells suggest immune crosstalk within the
 TME. Further, the data are supported by our observations that NKG2A⁺ NK and CD8 T cells are

significantly closer in proximity to HLA-E^{HIGH} tumor cells (Fig. 2). NK cells and T cells expressed a 344 variegated array of CXCR3, CXCR4, and CCR7 (Fig. 3I) and HLA-E^{HIGH} tumor cells uniquely express 345 346 ACKR3 (CXCR7) (and to lesser extent CXCR4) (Fig. 4E), indicating an important axis with CXCL12. 347 Additionally, KLRC1-expressing NK and CD8 T cells expressed significantly higher AREG (amphiregulin) 348 which signals through EGFR. To test the hypothesis that chemokine signaling explains why NKG2A⁺ NK 349 and CD8 T cells are biased towards HLA-E^{HIGH} tumor cells, we measured across all major clusters 350 expression of chemokines and their receptors: a) CCL19, CCL21 \rightarrow CCR7; b) CXCL9, CXCL10, CXCL11 351 \rightarrow CXCR3; c) CXCL12 \rightarrow CXCR4 and CXCR7; and d) amphiregulin \rightarrow EGFR (Fig. 4H). We observed 352 HLA-E^{HIGH} tumor cells expressed higher levels of EGFR compared to HLA-E^{DIM/NEG} tumor cells, whereas AREG was expressed by NK cells as well as dendritic cells (DCs), monocytes, mast cells, and even HLA-353 E^{HIGH} tumor cells at low levels. CXCL12 was mostly expressed by stromal cells, whereas CXCR4 was 354 355 expressed by NK cells, B and T cells (including Tregs), and myeloid cells. CXCR3 was mostly relegated 356 to NK and T cells and DC1 cells, and CXCL9, CXCL10, and CXCL11 were mostly expressed by 357 monocytes, macrophages and DCs. Finally, CCL19 was very specific for mregDCs and CCL21 by 358 endothelial cells suggesting important interactions with CCR7-expressing B and T cells.

In a recent study of BCG-unresponsive NMIBC by Rouanne et al²⁶, the authors demonstrated that 359 360 BCG can directly infect bladder tumor lines driving epithelial to mesenchymal transitioning (EMT), 361 autophagy flux impairment, a loss of class I HLA expression, and increased cell cycling. The study focused 362 on BCG-unresponsive NMIBC and found that patients with a dominant tumor phenotype showing these 363 hallmarks experienced significantly poorer metastasis-free survival. In our study, we next sought to stratify 364 tumor cells according to their HLA-E expression and measure average gene expression across the hallmark 365 pathways for EMT, autophagy, and cell cycle (Extended data Fig. S3). We observed a remarkably similar 366 phenotype of HLA-E-negative tumors as *in vitro* BCG-infected tumor lines showing significantly higher 367 EMT phenotype along with reduced autophagy flux genes and increased cell cycle. The data might suggest 368 that a proportion of recurring tumor cells in the face of BCG therapy, undergo *in vivo* infection rendering 369 them less sensitive to cytokine stimulation and chemokine attraction and promoting this stratification where 370 HLA-E^{HIGH} tumor cells are in significantly closer proximity to CXCL12⁺ stromal cells and immune cells.

To study the potential interactions between NK and CD8 T cells and HLA-E^{HIGH} tumor cells, we modeled the interactions using NicheNet, an algorithm that uses a combination of transcriptomic data, known ligand-receptor interactions, and gene-gene signaling and regulatory relationships to predict potential interactions between cells of interest (**Fig. 4I**) ³³. The top twelve ranked ligands from KLRC1⁺ NK, KLRC1⁺ CD8 T cells, and KLRC1⁺ T cell-cycle cells predicted to interact with HLA-E^{BRIGHT} tumor cells were *IFNG*, *TNF*, *TNFSF12* (TWEAK), *APOE*, *TNFSF14* (LIGHT), SEMA4D, *TNFSF10* (TRAIL), *AREG*, *GZMB*, *ALOX5AP*, *GPI*, *NUCB2* (**Fig. 4J**). KLRC1-expressing T cell-cycle and CD8 T cells 378 expressed the highest levels of IFNG, while AREG expression was highest in NK cells. Putative receptors 379 for these ligands, including IFNGR1, IFNGR2, TNFRSF1A/10B/12A/14/21, SORL1, LDLR, AMFR, 380 ALOX5, EGFR, IGF2R, and PLXNB1 were most highly expressed in the BCG-unresponsive samples, 381 suggesting the presence of corresponding signaling activity by recurring tumors (Fig. 4J). To further 382 examine genes upregulated in the tumor as a consequence of signals from NK and T cells, a circos plot 383 revealed the ligand-target weights of the top third of predicted relationships between 'sender' or effector 384 ligands and 'receiver' or target genes, defining the 'putative effects of the HLA-E/NKG2A axis" in bladder 385 tumors as well a targeted 'IFNγ-mediated' and 'AREG-mediated' adaptive resistance signatures (Fig. 4K). 386

000

387 Organization of the TME through immune crosstalk with stroma and HLA-E^{bright} tumors

388 To spatially resolve the relationships between tumor cells, stroma and immune infiltrates, we 389 performed spatial transcriptomics (ST-seq) analysis of bladder tumor sections from four treatment-naïve 390 and four BCG-unresponsive tumors (Fig. 5). Clustering analysis revealed 12 unique clusters, where cluster 391 12 remained unclassified and was removed from subsequent analyses (Fig. 5A-5C). Clusters were 392 annotated by their proportional composition by immune, stromal, and/or tumor cells defined using gene 393 signatures derived from scRNAseq analysis (Figs. 3 and 4). Clusters were defined both by the gene content 394 defining immune, stromal, and/or tumor cells but additionally integrating regional features of the tumor 395 tissue (Fig. 5C and 5D, Extended Figure S4). We profiled the relative abundance of each spatial cluster 396 between BCG-naïve (pre-BCG) and BCG-unresponsive (post-BCG) tumors (Fig. 5E). We observed clear 397 differences, where spatial clusters #0, 3, 4, and 6 were substantially enriched in BCG-unresponsive tumors. 398 Conversely, there was a trend for enrichment of clusters # 1, 2, 5, 7, 8, and 11 in BCG-naïve tumors. Only 399 spatial cluster # 8 lacked the presence of immune cells, and cluster 10 was defined by neutrophils 400 exclusively, where they were near regions enriched with DCs, Tregs, T cell-cycle and tumor cells.

401 ST-seq VisiumTM spots are 55 μ m in diameter and require deconvolution to understand which cell 402 lineages are represented as well as their relative abundances (**Fig. 5F**). We performed neighborhood 403 analyses to measure proximity of *HLA-E*^{HIGH} and *HLA-E*^{DIM/NEG} tumor Visium spots to CD8 T cells and NK 404 cells (**Fig. 5G**) as well as Tregs (**Fig. 5H**). A summary of the average distances to *HLA-E*^{HIGH} and *HLA-*405 $E^{DIM/NEG}$ tumor Visium spots from BCG-naïve and BCG-unresponsive tumors revealed significantly closer 406 proximity of *HLA-E*^{HIGH} tumor spots to NK cells, Tregs, and CD8 T cells. This observation was restricted 407 to BCG-unresponsive tumors (**Fig. 5I**).

408 To better understand the mechanisms underlying preferential interactions of immune cells with 409 $HLA-E^{HIGH}$ tumor cells, we tested the hypothesis that stroma-produced CXCL12 mediates recruitment of 410 CXCR7⁺ HLA-E^{HIGH} tumor cells to regions where macrophages and DCs produce CXCL9, CXCL10, and/or 411 CXCL11 that mediate recruitment of NK cells and T cells (**Fig. 4H**). Spatial relationships were investigated 412 on the 'nano-environment' level, defined as a Visium spot with a radius of 2.5 adjacent Visium spots, or 413 ~138 microns. A representative BCG unresponsive tumor section with brightfield image of underlying tissue is shown with HLA-E^{HIGH} tumor/stroma Visium spots shown in blue, and HLA-E^{DIM/NEG} Visium spots 414 415 shown in tan represented in Fig. 6A. Additional profiling of NK and CD8 T cells and Tregs revealed their 416 distribution being close in proximity to HLA- E^{HIGH} tumor/stroma Visium spots. BCG-unresponsive tumors 417 revealed significantly higher levels of tumor/stroma spot infiltration with cytotoxic NK and CD8 T cells 418 (7.05 times closer) and regulatory T cells (Tregs, 2.66 times closer) when compared to the BCG-naïve state 419 (p < 0.0001 for both). Using the same representative BCG-unresponsive tumor section, a topographical 420 map of HLA-E expressing tumor/stroma spot density is shown overlaid on top of a neighborhood analysis 421 highlighting the intensity of neighboring NK and CD8 T cell infiltration (Fig. 6B).

422 To investigate the biased distribution of NK and T cells near $HLA-E^{HIGH}$ tumor-stroma spots, we 423 profiled bladder tumor-stroma spots for expression of cytokines and chemokines (Fig. 4H). Among the 424 chemokines with detectable gene expression by ST-seq analysis, we observed a strong correlation between 425 CXCL9 (Fig. 6C-6E, Extended Figure S5) and HLA-E expression as well as between CXCL12 and HLA-426 E expression (Fig. 6F and 6G). We next applied our neighborhood analysis to profile tumor expression of 427 known checkpoint ligands, HLA class I expression as well as the IFN-response pathway as a function of 428 proximity to neighboring NK cells and CD8 T cells (Fig. 6H). Analysis of 5,319 tumor-stroma spots 429 (defined by >95% tumor- and stroma-specific genes revealed a clear program by tumor/stroma regions 430 increasing expression of inhibitory ligands CD47, CD274 (PD-L1), and HLA-E as a greater number of NK 431 cells and CD8 T cells were in contact with tumor-stroma spots (Fig. 4G). Additionally, we observed 432 increased tumor-stroma spot expression of the apoptotic genes PDCD2 and FAS and the adhesion molecule 433 CD58 (LFA-3), known to interact with CD2-expressing NK and T cells. Finally, tumor-stroma spot 434 expression of IFNGR1 and IFNGR2 along with JAK1/JAK2, STAT1, IRF1 and IRF9 were increased as a 435 greater number of NK and CD8 T cells were in contact. STAT3 expression did not change as a function of 436 neighboring NK and CD8 T cells, and SOCS1 expression was reduced with neighboring NK and CD8 T 437 cells, suggesting that tumor-stroma regions are actively responding to IFN signals. Tumor-stroma 438 expression of these genes was further stratified according to high vs dim/negative expression of HLA-E 439 (Fig. 6I).

To validate the ST-seq analyses, we used immunofluoresecence and the PhenoCycler/CODEX
platform to profile 59 antibodies (Supplemental Table S2) in order to better define the interactions between
tumor cells and multiple cell lineages. Antibodies targeted markers distinguishing tumor cells (pancytokeratin (CK), GATA-3, S100A4) from stromal endothelial cells and fibroblasts (Collagen Type IV,
podoplanin, vimentin, PECAM1/CD31), and immune cells (CD45), including monocytes, macrophages,
dendritic cells (CD14, CD16, CD68, CD11b, CD11c, HLA-DR), neutrophils (CD66b, CD16), B cells

446 (CD20, CD138), CD4 and CD8 T cells (CD3, CD4, CD8), Tregs (CD3, CD4, FoxP3), and NK cells
447 (NKp46, Gzm.B, CD16) (Fig. 6J and 6K).

448

449 Tumor-derived NK and CD8 T cells retain functional competence at time of tumor recurrence.

450 To better understand if an elevated expression of cytolytic genes in tumor-derived NKG2A-451 expressing NK and CD8 T cell populations correlated with improved functional sensitivity, we used mass 452 cytometry (CyTOF) to profile the *in vitro* responsiveness of tumor-derived cells from BCG-unresponsive 453 NMIBC patients at time of tumor recurrence. We tested their ability to respond to HLA-E⁺ PD-L1⁺ tumors 454 in the presence/absence of durvalumab (anti-PD-L1 antibody) and/or monalizumab (anti-NKG2A 455 antibody), using an artificial K562 acute myeloid leukemia tumor model that allows for uniform HLA-E 456 and PD-L1 expression via pre-stimulation of tumor lines with exogenous recombinant IFN-γ. Briefly, after 457 24 hours incubation with recombinant IFN- γ [400ng/ml], stably transduced HLA-E⁺ K562 cells saw 2.7-458 fold and 2.1-fold-increase in expression of HLA-E and PD-L1, respectively, when compared with baseline 459 expression levels (Fig. 7A). Separately, tumor-infiltrating lymphocytes from four BCG-unresponsive 460 tumors were isolated and then expanded up to 13 days in the presence of low dose IL-2, IL-7, and IL-15 as 461 well as tetramers targeting CD3 and CD28. Finally, TGF- β , was included in the stimulation cocktail for an 462 additional three days to promote NKG2A expression by CD8 T cells ²⁴. Phenograph clustering analysis ³⁴ 463 of expanded TILs revealed NK cells uniformly expressing NKG2A as well as 10 unique clusters of CD8 T 464 cells with variegated expression of inhibitory checkpoint receptors (CD161, GITR, LAG3, PD-1, TIGIT, 465 Tim-3, NKG2A) as well as markers of activation, trafficking, and tissue residence (CD25, CCR4, CCR6, 466 2B4, CD103, CXCR3) (Fig. 7B and 7C). Four clusters (ID#: 2, 9, 15, 17) expressed elevated levels of 467 NKG2A, representing \sim 32.5% of the total CD8 TILs and reflecting the fraction of TILs predicted to react 468 to NKG2A-blockade. Additionally, ~9% (range, 3.91% - 14.04%) of all expanded TILs were comprised of 469 NK cells (CD14⁻ CD19⁻ CD3⁻ CD56⁺) and NK and CD56⁺ CD8 T cells were strongly enriched for co-470 expression of NKG2A. CD56 was then used as a surrogate for NKG2A as use of monalizumab precluded 471 our ability for detecting NKG2A with antibodies by CyTOF. Further, NKG2A and PD-1 expression by 472 CD8 T cells was variegated highlighting the dynamic and non-redundant mechanisms for regulating CD8 473 T cell activation ²⁴.

Following expansion and characterization, we performed 6-hour co-cultures of TILs with K562 cells with and without HLA-E and/or PD-L1 expression (**Fig. 7D-7F**). Additionally, we measured the effects of PD-L1-blockade or combined PD-L1- and NKG2A-blockade on NK and CD8 T cell degranulation (CD107a) and expression of IFN- γ . WT K562 cells were used as positive control condition for measuring NK and NKG2A-expressing CD8 T cell activation. We observed that NK cells and CD56⁺ CD8 T cells were sensitive to HLA class I^{-/-} K562 cells compared to *ex vivo* activity, and their response was

480 diminished when K562 cells stably expressed HLA-E or HLA-E and PD-L1. NK cell activation was 481 restored in response to both HLA-E⁺ and HLA-E⁺ PD-L1⁺ K562 cells when pre-treated with anti-NKG2A 482 Ab alone or in combination with anti-PD-L1 Ab (CD107a: 2.1-fold increase, p=0.02; IFN- γ : 1.6-fold 483 increase, p=0.05).

484 Unlike NK cells, CD56⁺ CD8 T cells were more dynamic in their co-expression profiles for 485 NKG2A and PD-1 staining. Similar to NK cells, untreated CD56⁺ CD8 TILs were not reactive to HLA-E⁺ 486 K562 cells with or without co-expression of PD-L1. Activation of CD56⁺ CD8 TILs was only significant 487 in the presence of both anti-NKG2A and anti-PD-L1 Abs (CD107a: 1.75-fold increase, p=0.02; IFN- γ : 1.8-488 fold increase, p=0.007) (**Fig. 7F**). Collectively, the data strongly suggest sensitivity of NK and CD8 T cells 489 to combination immunotherapy strategies following tumor recurrence after failing BCG therapy.

490

491 Discussion:

492 Adaptive resistance can be driven by tumor-intrinsic and/or extrinsic mechanisms in overcoming 493 immune pressures ^{11, 12, 13, 35}. Evidence from mouse and human studies demonstrates that interferons, while 494 stimulating a robust anti-tumor response, also upregulate immune-suppressive factors in the setting of 495 prolonged activation. In melanoma, IFN- γ from CD8 T cells was shown to upregulate tumor PD-L1 expression and mediate infiltration of FOXP3⁺ regulatory T cell pathways within the TME ³⁶. In a broader 496 497 meta-analysis across 18 tumor indications, including bladder cancer, inflammatory mediators including 498 IFN- γ were associated with inhibitory immune checkpoints, including PD-L1/L2 ^{37, 38}. Despite emerging 499 evidence positioning pro-tumorigenic roles for IFN- γ , there are well-established anti-tumor functions 500 mediated through IFN- γ that are critical for anti-PD-L1 immunotherapy ³⁹. Anti-tumor inflammation, 501 therefore, exists along a continuum where an equilibrium is necessary for appropriate immunotherapeutic 502 efficacy⁴⁰.

In a recent investigation conducted by Rouanne et al.²⁶, distinct patterns of disease progression after BCG therapy and cystectomy were identified in the context of NMIBC. The study revealed that BCGunresponsive NMIBC patients characterized by tumors bearing a 'BCG infection' phenotype correlated with poorer survival. Conversely, BCG-unresponsive patients exhibiting HLA class I proficiency in tumor cells after BCG therapy (before cystectomy) demonstrated greater abundance of CD8 T cell tumor infiltrates, upregulation of inflammatory cytokines, and the presence of inhibitory checkpoint molecules. This latter group experienced significantly improved metastasis-free long-term survival post-cystectomy.

510 In our own investigation, we delved into the primary resistance mechanisms to BCG therapy and 511 explored the impact of BCG-induced inflammation on the dynamic interplay between tumor and immune 512 cell populations. Utilizing both prospective and retrospective NMIBC specimens collected before, during, and after BCG treatment, our study uncovered a pervasive inflammatory response in both BCG responders and non-responders alike. Our findings implicated IFN- γ in directly contributing to the upregulation of HLA-E by approximately 43% of recurring NMIBC tumor cells, and uniquely evident in all BCGunresponsive patients. Spatial analyses of tumor cells, stratified by their proximity to infiltrated NK and T cells, unveiled a program of tumor activation (and potential dysregulation) and selective recruitment to stromal-rich regions replete with immune effector and regulatory cells that are responding to the same collection of chemotactic signals.

520 Distinctive to BCG-unresponsive tumor cells, localized areas or 'nests' exhibiting elevated 521 expression of HLA-E were enriched for expression of CXCL9 and CXCL12. This activation correlated 522 with the infiltration of NK cells, CD8 T cells, and Tregs. Notably, even within confined regions of tumor tissue featuring a mix of HLA-E^{DIM/NEG} and HLA-E^{HIGH} tumor cells, a significant preference was observed 523 for the proximity of NK and CD8 T cells to HLA-E^{HIGH} tumor cells. These findings hint at an evasion 524 mechanism wherein HLA-E^{HIGH} tumor cells (responding to stroma-derived CXCL12) appear to play a role 525 526 in safeguarding HLA class I negative tumor cells. The expression of the NKG2A receptor also emerged as 527 a critical factor in categorizing the anti-tumor cytolytic functions of NK and CD8 T cells. However, our 528 observations revealed that NKG2A⁺ NK and CD8 T cells also expressed several well-established secondary 529 checkpoint receptors, emphasizing the necessity for a comprehensive understanding of the inhibitory 530 landscape within patients' tumors to inform effective second-line immunotherapy strategies.

531 Upon removing NK and CD8 T cells from their suppressive microenvironment, these cells 532 demonstrated retained functional capacity. Both NK and CD8 T cells, enriched for NKG2A expression, 533 exhibited highly enhanced cytolytic reactivity to HLA-E⁺ PD-L1⁺ K562 tumors in the presence of 534 combination NKG2A/PD-L1 blockade. Collectively, these findings portray a landscape of immune 535 dysregulation prominently characterized by elevated tumor expression of HLA-E and PD-L1 in the context of BCG-induced chronic activation and inflammation. Importantly, HLA-E^{HIGH} tumor cells similarly 536 537 expressed higher levels of CD47, Nectin-2 (CD112), Nectin-4, PVR and at higher levels compared to PD-L1 expression. Further, HLA-E^{HIGH} tumor cells expressed higher levels of decay accelerating factor (DAF, 538 539 CD55) and CD59, which block C3 convertase and formation of the membrane attack complex, two critical 540 steps in driving complement-mediated inflammation and phagocytosis, and apoptosis, respectively. Finally, 541 the trophoblast-2 (Trop2) antigen was highly expressed on all recurring NMIBC tumor cells. These data 542 suggest future combination immunotherapy strategies may benefit from additional targets that are strongly 543 engaged in BCG-unresponsive NMIBC patients. Emphasizing this point, antibody-drug conjugates targeting Trop2 (sacituzumab govitecan)⁴¹ and Nectin4 (enfortumab vedotin)⁴² have demonstrated 544 545 promising improvements in patient outcomes for metastatic triple-negative breast cancers and muscle-546 invasive bladder cancer, respectively; the latter which, when combined with pembrolizumab (PD-1

blockade), has recently been approved FDA clearance in an all comer population for 1st line treatment of
 metastatic urothelial carcinoma ⁴³.

549 Intravesical administration of BCG is initiated as adjuvant immunotherapy, as complete tumor 550 resection is the initial diagnostic and therapeutic step. Thus, initiation of standard of care (SOC) BCG 551 immunotherapy presupposes inflammation without an active tumor to clear ⁴⁴. Treatment improvements for 552 NMIBC and BCG-resistant disease have lagged. This may be, in part, because few studies have attempted 553 to understand the relationship between the timing of tumor recurrence, reasoning for the recurrence, and 554 the state of the immune system at the time of recurrence. Poor dosing study designs and lack of 555 understanding of the mechanisms underlying a therapeutic response to intravesical BCG have led to a 556 significant gap in knowledge and benefit for patients with NMIBC compared to muscle-invasive or 557 metastatic disease.

558 Our findings suggest that all NMIBC patients at the time of tumor recurrence show signs of a 559 hallmark anti-tumor immune response dominantly driven by IFN-y. BCG-unresponsive tumors see uniform 560 increases in chemotactic cytokines and inflammatory pathways that should otherwise function to suppress 561 tumor growth. Further, increased expression of inhibitory ligands on BCG-unresponsive tumor cells was 562 observed, suggesting that inflammatory stimuli had been prolonged and triggered feedback mechanisms 563 responsible for immune evasion. These results are seen on multiple levels, including bulk and single-cell 564 RNA sequencing, spatial sequencing, multiplex imaging, and mass cytometry. This implies that when 565 tumors recur, for reasons beyond the scope of this study, they are met by an overactive status of the immune 566 system ill-equipped to combat them.

567 Previous analyses profiling urine analytes between the BCG naïve and third dose timepoints 568 demonstrated that three doses of BCG induced an inflammatory response hundreds of times above baseline 569 levels of cytokines, including but not limited to IP-10, MIP-1 β , IL-8, IL-6, and TNF α ⁴⁵. Importantly, the 570 third dose-response dwarfed the magnitude of the first dose-response, suggesting that repeated exposure 571 increases the magnitude of inflammation ⁴⁵. While these data did not profile out to the time of tumor 572 recurrence, they lend credence to the theory that all patients experience a ubiquitous and increasingly 573 powerful immune response to repeated doses of BCG. Importantly, our findings confirm these previous 574 observations. Further, they demonstrate that inflammation is sustained even throughout the six-week 575 treatment interruption at time of first cystoscopy and do not equilibrate to baseline levels.

576 Novel to our study is the spatially-resolved insights into potential consequences of IFN- γ 577 dysregulation and tumor cell and immune homing patterns. Preferential trafficking of *HLA-E*^{HIGH} tumor 578 cells to immune-rich regions was seen in areas of high expression of *CCL19*, *CCL21*, *CXCL9/10/11*, and 579 CXCL12, and chemokines were detected in the urine early following start of therapy and were sustained 580 throughout therapy. Further, BCG unresponsive tumor-stroma proximity to cytolytic cells and Tregs was

increased by a median of 7-fold and 2.6-fold, respectively, when comparing $CXCL9/10/11^{\text{HIGH}}$ to 582 $CXCL9/10/11^{\text{DIM/NEG}}$ tumor nests.

583 Clinical efficacy in checkpoint blockade is dependent on reinvigorating effector cells expressing 584 high levels of the targeted checkpoint(s). Congruent with analogous studies, we found that NKG2A⁺ NK 585 and CD8 T cells were enriched in BCG-unresponsive tumors and tumor-derived NK and CD8 T cell anti-586 tumor functions were intact at the time of tumor recurrence. Additionally, co-culture experiments with 587 patient TILs and K562s with and without HLA-E and PD-L1 confirmed the ability of combination anti-588 NKG2A plus anti-PD-L1 blockade to enhance the cytolytic function of stimulated TILs from patients at 589 time of tumor recurrence. This reinforces both the use of NKG2A to reinvigorate cytolytic effector 590 functions by NK and CD8 T cells, as well as the potential to exploit a critical mechanism of tumor 591 resistance, whereby chemokines lure in effector cells to take on exhausted phenotypes.

592 Recent clinical evidence emerging from interim results of the randomly controlled Phase II COAST 593 trial demonstrated significantly prolonged survival in non-small cell lung cancer (NSCLC) patients treated 594 with monalizumab combined with durvalumab compared to standard of care durvalumab alone for 595 treatment of unresectable stage 3 NSCLC²⁵. This combination is being further evaluated in a larger planned 596 Phase III trial (PACIFIC-9, NCT05221840) following these promising early results. Collectively, our data 597 demonstrate that elevated tumor expression of HLA-E and PD-L1 and chronic activation of NKG2A-598 expressing NK and CD8 T cells are hallmark features of resistance to BCG immunotherapy in NMI bladder 599 tumors and that integrating NKG2A-blockade into combination immunotherapy strategies may prove 600 particularly effective in settings of BCG-unresponsive, high-grade NMIBC. Based on the data generated 601 from this study, we recently designed a Phase 2 trial of durvalumab (MEDI4736) and monalizumab in 602 NMIBC. The Phase 2 ENHANCE (Elevated NKG2A and HLA-E Amplify NK and CD8 T-cell Engagers) 603 (clinicaltrials.gov ID: NCT06503614) will investigate the effects of monalizumab (anti-NKG2A Ab) plus 604 durvalumab (anti-PD-L1 Ab) for combination checkpoint blockade in high-grade BCG-unresponsive 605 NMIBC as a bladder-sparing immunotherapy strategy. In this trial, an exploratory objective is to assess the 606 relationship between baseline tumor HLA-E expression and clinical outcomes to facilitate development of 607 HLA-E as a potential biomarker for patient selection in future clinical trials intending to target NKG2A.

608 Our study has notable limitations. Our sample sizes, while being the largest NMIBC spatial 609 sequencing and single-cell RNA sequencing cohorts available, are small and present a potentially limited 610 view of the disease. Additionally, as BCG is administered as an adjuvant therapy, we are only afforded 611 access to bladder tissues after treatment if tumor recurs. Thus, it was not feasible to profile bladder tissues 612 in the absence of tumor following exposure to BCG. Future studies might benefit from a neoadjuvant 613 approach, where tumor tissue can be sampled and profiled for potential therapeutic responses to BCG.

614 Collectively, our analyses suggest that the current guidelines on immunotherapy for BCG-615 unresponsive NMIBC could be improved via a multi-cell-targeting immunotherapy approach focused on 616 NK cells alongside T cells. Randomized trials from bladder and other tumor indications have shown that 617 PD-1/PD-L1 stratification fails to predict response to immunotherapy with anti-PD-1/PD-L1 antibodies: 618 IMvigor210, JAVELIN bladder 100, and CheckMate-275 (NCT02108652, NCT01772004, NCT02387996) 619 all saw that PD-1/PD-L1 biomarker stratification alone did not effectively stratify response rates. In 620 comparison, recent results using KLRC1 (NKG2A) expression in the pre-treatment tumor significantly 621 improved predicted anti-PD-L1 response rates in the IMvigor210 cohort, but only in the CD8^{HIGH} PDCD1 622 (PD-1)^{HIGH} group ²⁴. In fact, where IHC stratification of PD-L1 expression has failed to predict 623 immunotherapeutic responses, KLRC1 stratification in IMvigor210 showed protective effects were 624 restricted to the PD-L1 IC high group. In conclusion, while our analysis does not exclude the presence of 625 alternative checkpoints, it lends evidence to the hypothesis that combination NK and T cell 626 immunotherapeutic approaches may hold the key to improved outcomes for NMIBC patients.

627

628 Methods

629 Patients and samples

630 Patients at Mount Sinai Hospital (MSH) were enrolled in the study following Institutional Review 631 Board (IRB) approval (protocol 10-1180). 10-1180 covers the use of patient tissues in a biorepository and 632 allows for prospective collection of blood, urine, and tissue samples from enrolled patients. Formalin-fixed 633 paraffin-embedded (FFPE) blocks from BCG patients were obtained retrospectively from the biorepository 634 and prospectively for patients receiving treatment. For prospective patients, samples were collected on the 635 day of surgery and throughout BCG immunotherapy. Due to IRB limits on the collection, blood and urine 636 samples were taken at the first dose, third dose, and sixth dose of the induction cycle; at every follow-up 637 cystoscopy; and at the third maintenance cycle dose. Tumor samples were taken at every possible timepoint. 638 BCG naïve was defined as any patient who had yet to receive BCG, regardless of past treatment with other 639 chemotherapies. BCG-unresponsive was defined as any patient with recurrent tumors following at least five 640 of six induction doses of BCG at time of first evaluation.

641

642 Sample processing

Blood and urine samples from bladder cancer patients were processed to collect PBMCs, serum,
and cell-free urine. Blood was spun down (4C, 2000rpm, 10 min) to isolate serum, and PBMCs were
collected using Ficoll-Paque isolation. PBMCs were frozen down in a Mr. Frosty at -80 C for 24 hours and

stored at -160 C in 10% DMSO and 90% fetal bovine serum; PBMCs and cell-free urine were stored at -80C.

Tumor tissues obtained from transurethral resections of bladder tumor (TURBT) were placed into RPMI medium immediately after removal and transferred to the laboratory for additional processing. Bladder and lymph nodes obtained from radical cystectomies were sent from the operating room directly to the pathology suite after completion of the lymph node dissection. The bladder was bivalved; samples of visible tumor were extracted and placed in RPMI medium, and the tumor was transferred to the laboratory for additional processing.

Fresh tumor samples underwent a variety of different processing techniques based on the planned
experiment. Tumor used for spatial sequencing was placed in a 10 mm x 10 mm cryomold with optimal
cutting temperature (OCT) media and frozen down on a thermal block immersed in liquid nitrogen. Tumor
tissues were digested using tumor dissociation enzymes (Miltenyi, 130-095-929) and a GentleMACS
machine (program 37C_h_TDK_3) at 37C. Mechanically and enzymatically separated tissues were filtered
through a 70µM cell strainer and assessed on Countess II (ThermoFisher) for viability and cell numbers.

660

661 In situ hybridization and targeted RNA sequencing

662 FFPE sections from 40 retrospective NMIBC cases were obtained from the institutional 663 biorepository and used for targeted RNA sequencing. RNA was extracted from five and ten μm sections. 664 HTG EdgeSeq lysis buffer was added to lyse and permeabilize the samples. Nuclease protection probes 665 (NPPs) were added to the lysed samples and hybridized to the target mRNA. A nuclease was added to 666 digest non-hybridized mRNA and excess NPPs. The nuclease digestion reaction was finalized with a 667 termination solution followed by heat-mediated denaturation of the enzyme.

Each sample was used as a template for PCR reactions with specially designed primers. Each primer contains a unique barcode that is used for sample identification and multiplexing. Samples were analyzed simultaneously on an Illumina sequencing platform to prepare the library. All samples and controls were quantified in triplicates. No template control (NTC) reactions were made for each master mix used during the qPCR process to test the absence of a probe or qPCR contamination. Molecular-grade water was used in place of a test sample in the NTC reactions using the same volume as the template.

Sufficient concentration of sample for library pooling, appropriate dilution for the library pool, and
volume of denaturation reagents to add to the library were determined by HTG library calculator. 2N NaOH
and heat (98C, 4 minutes) were used for library denaturation. The denatured library was loaded into the
well of the NextSeq sequencing cartridge. Sequencing was performed using an Illumina NextSeq sequencer.

The sequencing data on mRNA expression of target genes were imported into HTG EdgeSeq parser software. HTG biostatistics department performed quality control analyses and normalized the data. Data were returned from the sequencer as demultiplexed FASTQ files with four files per assay well. The HTG EdgeSeq parser software aligned the FASTQ files to the probe list and collated the data.

Prior to any analyses, clinical data on all patients was gathered. The following items were collected for all samples processed by HTG Molecular: patient date of birth; gender; age at BCG induction; BCG status (unresponsive vs. naïve vs. exposed); date of sample collection; stage at collection; grade at collection; recurrence date; time to recurrence; time to progression; BCG start date; BCG last exposure; BCG induction cycle last dose; prior chemotherapy; cystectomy; date of cystectomy; stage at cystectomy.

Following clinical data collection, a gene set enrichment analysis (GSEA) was performed on the targeted RNA sequencing data. Specifically, we used paired patient samples before and after BCG exposure in the BCG recurrent patient population only. We used custom gene sets, as well as all Hallmark gene sets from the Broad Institute's MSigDB, as inputs for the enrichment analysis ²⁷. Statistical significance was set at p < 0.05, and gene sets found to be significant are listed in **Supplementary Table S1**. All gene sets found to be statistically significant were evaluated for leading-edge genes, defined as the genes that contribute most to the enrichment score and associated p-value.

The leading-edge genes from statistically significant gene sets in the GSEA were collated and used to assess for group differences between the paired HTG patient samples. We performed these analyses specifically on the BCG-recurrent cohort. Prior to any analyses, a Shapiro-Wilk test, chosen for suitability in small sample sizes, was used to assess for normality ⁴⁶. All samples with p < 0.05 were considered not normally distributed, and a Kruskal-Wallis test was performed to assess for group differences ⁴⁷. All other samples were assessed using an independent T-test. Genes with statistically significant differences between the BCG naïve and the BCG-unresponsive populations were then visualized on radar plots.

701

702 Protein concentration measurement

Cell-free urine supernatant and serum samples were randomized in a 96-well plate. Diluted samples and positive and negative controls were incubated overnight with an incubation mix (incubation solution, incubation stabilizer, A-probes, and B-probes) at 4°C. Samples were then incubated with an extension mix (High purity water, PEA solution, PEA enzyme, PCR polymerase) for 5 min and placed on a thermal cycler. Following the thermal cycler, samples were incubated with a detection mix (detection solution, High purity water, detection enzyme, PCR polymerase) and transferred to a chip. Primers were loaded onto the chip, and the chip was profiled using the Fluidigm IFC controller HX with the Fluidigm Biomark Reader. Data

were normalized using extension and interplate controls and a correction factor. The resulting data werereported in normalized protein expression (NPX) units on a log2 scale.

712

713 IFN-γ co-culture

Cell lines and CD45- isolated primary tumor cells were incubated in media optimized for high
viability for 72 hours (RPMI-1640 supplemented with 20% fetal bovine serum). Tumor cells were expanded
until they were confluent in 2 T175 flasks. Following expansion, cells were culture in 100 ng / mL of IFNγ for a total of 24 hours in a 24 well plate. Following co-culture, cell lines were trypsinized (immortalized),
and primary tumors were gently removed from the solid phase by a cell scraper. Samples with and without
IFN-γ stimulation were measured for HLA-E and PD-L1 protein expression levels.

720 HLA-E and PD-L1 levels were assessed via FlowCytometry. Cells were stained in 4C FACS buffer 721 (phosphate-buffered saline (PBS) with 2% heat-inactivated FBS and EDTA 2 mM) for 30 minutes. 722 Subsequently, cells were washed in PBS, incubated for 20 minutes in a viability dye, washed again with 723 PBS, and resuspended in 2% paraformaldehyde. The experiment was performed in triplicate, with three 724 readouts per cell line per experimental condition. FlowCytometry acquisition was performed using an LRS-725 Fortessa (BD Biosciences), and data were analyzed using the CytoBank software. When staining for HLA-726 E, cells were first stained 20 minutes with HLA-E prior to staining with additional PD-L1. In CytoBank, 727 several gates were applied to generate the final dataset. A live/dead gate was applied, followed by a gate to 728 remove doublets and isolate singlets. Lastly, the data was arcsinh transformed prior to analysis.

729 Once the final dataset had been generated, statistical significance between unstimulated and 730 stimulated cell lines was assessed. An independent t-test was run with a significance cutoff of p < 0.05.

731

732 Plasma and cell-free urine supernatant protein concentration analysis

733 We used the OLINK Proteomics[®]- inflammation panel to profile cell-free urine supernatant. 734 Protein levels were visualized at BCG naïve, third dose, sixth dose, and first-cystoscopy timepoint, 735 comparing NPX values for all patients between the BCG naïve timepoint and the sixth dose timepoint. 736 Additionally, urine supernatants from a validation cohort of NMIBC patients treated with BCG were used 737 from the Aarhus University as previously described ¹³. In order to determine the suitable statistical test, a 738 Shapiro-Wilk's test was used to assess for normality, and a Kruskal-Wallis test was used in every instance 739 in which one or both samples were not normally distributed. An independent T-test was used in the event 740 both samples were normally distributed. All statistically significant p values were then used to assess 741 adjusted p values via the Benjamini-Hochberg correction, with an alpha of 0.05. All statistically significant 742 genes between the BCG naïve and sixth induction dose time points are shown.

743

744 Multiplex Immunohistochemistry:

745 Sections of tumor for immunohistochemical (IHC) staining were taken at a thickness of 3-mm from 746 formalin fixed paraffin-embedded (FFPE) blocks. H&E-stained sections were performed every 5 - 10 slices. 747 The Ventana Discovery Ultra (Roche Diagnostics) machine was used to automatically bake, deparaffinize, 748 and condition the slices. The RUO Discovery Universal (v21.00.0019) was used to perform chromagen 749 IHC on sequential slices. Primary antibodies included (CD3, HLA-E, NKp46, and NKG2A) and were 750 utilized for staining on NMIBC tumors. All slices followed the same protocol, which included a 60 minute 751 incubation at 37°C; secondary antibodies using OmniMap HRP or NP DISCOVERY (Roche Diagnostics); 752 signal detection using Discovery OmniMap. Nuclear counterstaining with Mayer's hematoxylin; and 753 conversion to high-resolution images via the NanoZoomer S10 Digital slide scanner (Hamamatsu).

754

755 Tumor and CD3⁺ T cell expression and proximity analyses

756 Prior to analysis, all slides were reviewed and regions of interest were annotated by a board-certified 757 pathologist (R.B.). Tissue artifacts, including torn, folded, and damaged tissue, were excluded from any 758 analyses. The HALOTM (Indica Labs, Inc.) digital image analysis platform, a semi-automated platform using 759 machine learning to segment and label stained sections, was utilized for quantitative analyses. Halo AITM 760 and train-by-example classification, segmentation, and random forest classification was used to separate 761 chromogenic stains and generate tabular data for downstream analysis. Slide features of each tumor, 762 including cell lineages (tumor, stroma, and immune) and slide features (such as glass) were characterized. 763 Glass was excluded from all downstream analysee. Classified cell classes were tabulated, and positive 764 staining cells were stratified into expression tertiles (dim, moderate, and bright). Calibration for intensity 765 expression was performed using tonsil tissues from healthy human tonsil. In addition to cell counts, total 766 surface area (mm²) was recorded to facilitate density calculations. Statistical analyses were performed using 767 Python 3.8.1.

768

769 Proximity Ligation Assay

The NaveniFlex[™] Proximity Ligation Assay (PLA) was performed according to the manufacturer's instructions using NaveniFlex Tissue MR ATTO647N (Navinci, Sweden). PLA was performed on sections of tumor taken at a thickness of 3-mm from formalin fixed paraffin-embedded (FFPE) blocks. H&E-stained reviewed with pathologist. Briefly, after deparaffinization, rehydration, and antigen retrieval, slides were blocked with Block NT blocking solution (Navinci, NT.1.100.01) for 60 min at 37 °C in a preheated humidity chamber and then incubated with mouse anti-HLA-E (clone: MEM-E/02, Abcam, 1:200) and rabbit anti-NKG2A (clone: EPR23737-127, Abcam, 1:2000) diluted in Diluent 1 NT solution (Navinci,

777 NB.1.100.02) overnight at 4°C. As negative controls, two (tonsillectomy) slides were incubated in antibody 778 diluent with only one primary antibody each. After washing, the slides were incubated with the PLA probes 779 corresponding to the primary antibodies using anti-mouse Navenibody M1 NT (Navinci, NB.1.100.06) and 780 anti-rabbit Navenibody R2 NT (NB.1.100.07) in Diluent 2 NT solution (Navinci, NAvinci, NF.1.100.03) 781 for 60 min at 37 °C. Slides were then processed for ligation using reaction 1 reagent containing Buffer 1 782 NT (Navinci, NB.2.100.17) and Enzyme 1 NT (Navinci, NF.2.100.11) and subsequently reaction 2 reagent 783 containing Buffer 2 NT (NT.2.100.01) and Enzyme 2 NT (Navinci, NF.2.100.15) and incubated for 30 min 784 at 37 °C and 90 min at 37 °C, respectively. The slides were washed and incubated with post-block NT 785 reagent (Navinci, NF.1.100.01) in post-block supplement NT (Navinci, NT.2.100.04) for 30 min at 37 °C, 786 then processed for detection, counter-stained with DAPI, and mounted with coverslips using Prolong Gold 787 Antifade reagent (Invitrogen, P36930).

788

789 Images were captured at the Microscopy and Advanced Bioimaging Core of the Icahn School of Medicine 790 at Mount Sinai. A Leica DMi8 (Leica Microsystems, Germany) was equipped with a HC PL APO CS 791 10x/0.4 (Part Number 506285; Leica Microsystems, Germany) objective lens. A SpectraX fluorescence 792 illuminator (Lumencor, Oregon, USA) with multiple narrow-band light emitting diodes provided 793 illumination (LEDs used: 395/25nm for DAPI, 470/24nm for autofluorescence channel, and 640/30nm for 794 Navinci signal). The microscope and light source were controlled by LAS X software, version 3.7.5.24914 795 (Leica Microsystems, Germany). For fluorescence excitation, the following illumination settings were used: 796 a 395nm LED set to 50% (147mW at the SpectraX output port) for DAPI signal, captured at 20 milliseconds 797 of exposure; a 470nm LED set to 44% (86mW), captured at 70 milliseconds for an autofluorescence 798 channel; and a 640nm LED set to 100% (231mW), captured at 150 milliseconds for the target signal. A 799 multi-band pass filter set (Part Number 11525366; Leica Microsystems, Germany) was used to separate 800 fluorophore emission (Dichroic 415/490/570/660nm; Emission bands: 430/35, 515/40, 595/40, 801 720/100nm). Images were captured using a Leica DFC9000GT monochrome camera set to 12-bit depth, 802 2x2 (4-pixel) binning and "Low Noise" Gain mode. Images were captured in montage at 10% overlap, 803 merged ("Smooth" blending option) and then saved in the proprietary LIF ("Leica Image File") format 804 before being converted to IMS (Imaris) format for analysis.

805

Image analysis was performed using Imaris software 10.1.1 (Oxford Instruments, Concord MA). A surface
for the green background channel was created using the surface creation wizard with the following
parameters – Enable Region Of Interest = false, Enable Region Growing = false, Enable Tracking = false,

- 809 Enable Classify = false, Enable Shortest Distance = false, Enable Smooth = true, Surface Grain Size = 2.00
- 810 μ m, Enable Eliminate Background = false, Active Threshold = true, Enable Automatic Threshold = false,

811 Manual Threshold Value = 1900, Active Threshold B = false. Masked channels were created by subtracting 812 the intensities within the green surface from the blue and far-red channels: the mask intensity was set to 0 813 for inside the green surface while the outside was set to the original channel's value. A new surface was 814 created using the surface creation wizard for the masked far-red channel using the following parameters – 815 Enable Region Of Interest = false, Enable Region Growing = false, Enable Tracking = false, Enable Classify = false, Enable Shortest Distance = false, Enable Smooth = true, Surface Grain Size = $2.00 \mu m$, Enable 816 817 Eliminate Background = false, Active Threshold = true, Enable Automatic Threshold = false, Manual 818 Threshold Value = 1600, Active Threshold B = false. An area filter was applied to this far-red surface to 819 remove surfaces whose area was larger than 50um². A DAPI surface was created using surface creation 820 wizard with the parameters – Enable Region Of Interest = false, Enable Region Growing = true, Enable 821 Tracking = false, Enable Classify = false, Enable Shortest Distance = true, Enable Smooth = true, Surface 822 Grain Size = $2.00 \,\mu$ m, Enable Eliminate Background = true, Diameter Of Largest Sphere = $7.50 \,\mu$ m, Active 823 Threshold = true, Enable Automatic Threshold = false, Manual Threshold Value = 10, Active Threshold B 824 = false, Region Growing Estimated Diameter = $6.00 \ \mu m$, Region Growing Morphological Split = false, 825 Filter Seed Points = "Quality" above 60.0, Filter Surfaces = "Number of Voxels Img=1" between 10.0 and 826 500, to obtain individual nulcei within the field of views. Finally, a fourth surface was created by applying 827 the filter – Overlapped Area to Surfaces (Minimum = 0.050 um^2 , Maximum = false) to obtain the DAPI 828 surfaces that were in contact with the far-red channel. The counts of total number of nuclei and nuclei 829 overlapping with the masked far-red surfaces were extracted from the statistics tab of Imaris.

830

831 Single-cell RNA sequencing:

832 Data preprocessing

833 Single-cell RNA sequencing (scRNA-seq) analysis was performed using Scanpy package in Python 834 and Seurat package in R. After loading, genes expressed in fewer than three cells were excluded from later 835 analyses. Cells with < 200 or > 8000 unique genes, as well as cells containing >20% mitochondrial gene 836 transcripts, were discarded. Cells then go through scrublet to detect doublet population. Subsequent data 837 normalization was performed by dividing feature counts for each cell by total counts for that cell, scaling 838 by a factor of 10,000, and natural log transformation. Next, scvi model was set up to correct batch-effects. 839 Then we performed scaling and principal component analysis (PCA) on the batch-corrected data. Using the 840 first 50 principal components (PCs), graph-based clustering and UMAP dimensionality reduction was 841 performed to reveal 16 cell clusters. Cluster-specific marker genes were identified using the FindAllMarkers 842 function, and marker genes with a natural-log fold change (FC) > 0.25 and expressed in $\geq 25\%$ of cells 843 were used to annotate cell cluster identities based on known cell type markers ^{48,49,50}: CD8 T cells (CD8A, CD3E), CD8- T cells (CD3E), tumor cells (MUC1, KRT7/8/13/17/18), B cells (MS4A1, CD79A), 844

845 monocytes/macrophages (CD14, LYZ, FCGR3A, MS4A7), T regulatory cells (CD3E, FOXP3), granulocytes

846 (C1QA/B/C, ITGAM, FCGR3A), NK (NKG7, GNLY, KLRD1, KLRF1), fibroblasts (COL1A1, SPARC),

epithelium (*EMP1*), DC (*FCER1A*, *CST3*, *ITGAX*), plasma cells (*MZB1*, *JCHAIN*, *IGHG3*), and CD8 TRM

848 cells (*CD3E*, *CD8A*, *KLRD1*). Clusters 22, 24, 25, and 26 containing 224, 142, 141, and 101 cells,

respectively, were ultimately excluded from further analyses due to unclear cell identities. All scRNAseq

analyses were performed using distinct samples without repeated measurements.

851

852 Tumor subclustering analysis

853 We performed subclustering analysis on 18,520 bladder cancer (Blca) cells. Preprocessing steps 854 for the Blca subset included normalization, scaling, and PCA analysis. We then applied Canonical 855 Correlation Analysis (CCA) integration using the IntegrateLavers() function (dimensional reduction for 856 correction = pca) in Seurat v5 to correct batch effects 51 . Leiden clustering (resolution = 0.4) was applied to 857 the shared nearest neighbors (SNN) (dims = 1:10). This resulted in the identification of 9 heterogeneous 858 tumor subclusters, distinctly separated on the UMAP plot. Each subcluster was profiled by the expression 859 of tumor marker genes (EPCAM, UPK2) and cytokines (CXCL1, CXCL2, CXCL3, IFNGR1, etc.). 860 Subcluster B1 was removed from further analysis as it was identified as normal bladder cells with low 861 EPCAM (tumor-related marker genes), and subcluster B8 was removed due to high PTPRC expression, 862 indicating a high presence of immune cells (CD45+). Differentially expressed gene (DEG) analysis (MAST, R version 1.2.1) ⁵² and enrichment pathway analysis ⁵³ further characterized the subclusters, highlighting 863 864 their distinct biological profiles (Figure 2).

865

866 NicheNet Analysis

867 We used the NicheNet R package to infer potential ligand-receptor interactions between NK and T 868 cells and tumor cells, as well as potential regulatory effects in tumor gene expression as a result of these 869 interactions ³³. We added known ligand-receptor interactions between ligands IgG1 and IgG3 and the 870 receptor CD16 (weight = 1) to NicheNet's default ligand-receptor interactions database, and also integrated 871 the Harmonizome Pathway Commons Protein-Protein Interactions database: 872 (https://maayanlab.cloud/Harmonizome/dataset/Pathway+Commons+Protein-Protein+Interactions) with 873 NicheNet's default signaling network (weight = 1) 54, 55. We used the modified ligand-receptor interaction 874 and signaling networks for subsequent analyses. We defined the NK and T cell populations as senders and 875 tumor cells as receivers and derived a list of 92 receptors expressed in the receiver population by 876 intersecting the list of receptors from the ligand-receptor interaction network with genes expressed in at 877 least 10% of tumor cells in the RNA assay. Fifty potential ligands expressed in greater than 10% of the

sender NK and T cells were then derived based on their interaction with the list of 92 receptors. We then
calculated activity scores for each ligand based on its potential to affect the expression of Hallmark
interferon gamma response genes ^{27, 56}. Statistical analyses including Wilcoxon rank-sum tests and Pearson

- and Spearman correlations were performed using R v4.0.3.
- 882

883 Differential gene expression analysis

884 Spatial transcriptomic data were generated by Visium Spatial Gene Expression which is a spatial 885 transcriptomics solution by 10x Genomics. We obtained eight spatial sections consisting of four preBCG 886 and four postBCG samples. Sequencing data was aligned on GRCh38 and quantified using the Space Ranger Software Suite (version 1.0, 10x Genomics). We processed the ST data to characterize major cell 887 types and their spatial patterns using Giotto workflow ⁵⁷. Per section, Low quality spots (number of 888 889 expressed genes > 100), and lowly expressed genes (expressed in < 10 spots) were removed. The raw counts 890 were log2(x+1) transformed, followed by adjusting for batch effects and spot wise number of features using Pearson residuals approach by Lause et al ⁵⁸. The spatial network of nearest spots by Delaunay triangulation 891 892 was calculated to identify spatially co-expressed genes in neighboring spots via BinSpect-kmeans algorithm ⁵⁷, and distinct spatial domains by Hidden Markov Random Field (HMRF) model ⁵⁷. Then, different sections 893 894 were combined into a pan-section transcriptome by Harmony to identify pan-section clusters ⁵⁹. The pansection clusters will be identified by Leiden clustering ⁵⁷ to detect transcriptionally similar spots shared 895 896 across different sections. Subsequently, we identified 12 spatial clusters to profile the spatial transcriptomic 897 landscape. Differentially expressed genes (DEGs) between KLRC1⁺ versus KLRC1⁻ cells were found using 898 the FindMarkers function from the Seurat R package, where cells with KLRC1 expression greater than 0 899 in the RNA assay were labeled as KLRC1+.

900

901 Identification of HLA-E high/low tumor subsets in spatial transcriptome

902 As HLA-E expressions are not specific to tumors and HLA-E high/low tumor markers have not been 903 established, we performed a customized cell type presence inference workflow by utilizing Cell Atlas 904 Reconstruction from Spatially mapped Data (CARD) method ⁶⁰. CARD is a computational approach that 905 reconstructs cell-type-specific expression profiles from spatially mapped transcriptomic data, facilitating 906 the estimation of cell-type proportions within tissue sections. First, we generated reference single-cell transcriptomes of HLA-E^{high} and HLA-E^{low} tumor subsets by explicitly labeling tumors with HLA-E 907 908 expressions (high: HLA-E > 0, low: HLA-E=0). These tumor labels were utilized as the inputs to calculate 909 the relative abundances of the tumor subsets on the spatial voxels by CARD.

910 To further scrutinize the detection of HLA-E high tumors in the spatial transcriptome (ST) data, we 911 applied additional thresholds to require voxels with i) high HLA-E expressions, and ii) highly abundant HLA-E high tumor/stromal cells as inferred by CARD ⁶⁰. Per section, high HLA-E expression voxels were 912 913 identified as those with HLA-E expression values greater than zero (SCT normalized assay) and a z-score 914 of inferred HLA-E^{high} tumor/stromal cell abundance > 1.645 (90% confidence). Conversely, low HLA-E 915 expression voxels were identified as those with an absence of HLA-E expression (HLA-E expression equal 916 to zero) and a z-score of inferred HLA- E^{low} tumor/stromal cell abundance > 1.645 (90% confidence). 917 Similarly, we detected high confidence voxels with NK cells, CD8 T-cells and Treg cells by further applying 918 the abundance z-score > 1.645 for further analyses.

919 Proximity analysis between different cell types

920 We evaluated the proximity between different immune subsets (NK, CD8+ T, and regulatory T (Treg) cells) and HLA-E^{high/low} tumor cells to observe if distinct cytotoxic immune micro-environments are present, 921 922 conditioned on tumoral HLA-E expression status. Upon identifying high confidence voxels with HLA-923 E^{high/low} tumor/stromal cells and the immune cell types, we calculated the pairwise Euclidean distances 924 between the tumor/stromal cells and each immune cell type. To retrieve actual distance between voxels, the 925 matrix was refined using the computeCellDistance function from the CellChat v2 library in R⁶¹. For each voxel with HLA-E^{high/low} tumor/stromal cell presence, its overall distance to an immune cell type was 926 927 calculated as the mean distance over the 10 nearest neighboring voxels with the respective immune cell 928 presence. These distances were summarized across each section by taking the average over all HLA-E^{high/low} 929 tumor/stroma voxels, yielding the overall proximity with each immune cell type per section. These overall 930 proximity values were compared between pre-BCG and post-BCG groups by Wilcoxon Rank-sum test 931 (Figs. 5 and 6).

932

In-depth analysis of cell type enrichment across spatial clusters

933 We tested if each pan-section cluster shows enriched presence of distinct cell populations and subsets 934 as characterized by the scRNA-seq. To this end, for each section, we leveraged the inferred abundances of 935 different cell types in the spatial voxels by CARD, and tested if a cell type has significantly higher 936 abundances in each pan-section cluster than the other voxels by Wilcoxon Rank-sum test. Then, the overall 937 enrichments of each cell type within pre-BCG or post-BCG group were summarized by combining the 938 Wilcoxon test p-value across the sections via aggregated Cauchy association test (ACAT). The enriched 939 cell types per pan-section cluster in pre-BCG or post-BCG group were called with ACAT summarized FDR 940 < 0.05 and number of sections with significant enrichments (Wilcoxon FDR < 0.05) > 1 (Figure 4.3).

941

942 Mass cytometry antibody preparation and staining

943 PBMCs from BCG-treated bladder cancer patients at the time of tumor recurrence were isolated 944 using Ficoll-Paque and resuspended in cell medium (RPMI-1640 medium supplemented with 10% heat-945 inactivated FBS, 1% Penicillin, 1% Streptomycin and 1% L-glutamine). PBMCs were conjugated to 946 antibodies purchased from Fluidigm using the Maxpar X8 and MCP9 labeling kits. Platinum barcodes were 947 prepared as previously described. All antibodies were titrated prior to conjugation.

948 Prior to mass cytometry staining, all cells were incubated for 20 minutes at 37C in RPMI cell 949 medium (described above) and IdU (Fluidigm, t#201127), Rh103 (Fluidigm, #201103A). Following the 950 incubation, cells were centrifuged, washed with PBS and 0.2% bovine serum albumin (BSA), and incubated 951 for 3 minutes on ice with an Fc-blocking reagent. Samples were washed again with PBS and 0.2% BSA; 952 barcoded samples were pooled together and washed; finally, samples were stained with extracellular 953 antibodies for 30 minutes on ice and in PBS and 0.2% BSA.

When staining four samples, cells were single-barcoded using 194Pt, 195Pt, 196Pt or 198Pt. When staining five or six samples, cells were stained with combination of barcodes. Cells were again washed using PBS 0.2% BSA; barcoded samples were pooled together; samples were washed again and stained with extracellular antibodies for 30 minutes on ice in PBS 0.2% BSA. Cells were co-cultured in the presence of either WT or HLA-E-transduced K562 cells for a total of 6 hours.

959 Samples were washed with PBS 0.2% BSA and resuspended in Fixation/Perm buffer (Invitrogen, 960 #00-5523-00) for 30 minutes on ice. Cells were centrifuged and washed with Maxpar Barcode Perm Buffer 961 (Fluidigm, #201057) and barcoded using the Cell-ID 20-Plex Pd Barcoding kit (Fluidigm, #201060). 962 Barcoded samples were washed with permeabilization buffer (Invitrogen, #00-5523-00) and pooled. 963 Intracellular staining was then performed in permeabilization buffer with Heparin at a concentration of 964 100U/mL for 30 minutes on ice. Stained cells were washed with permeabilization buffer and resuspended 965 in PBS with PFA 2.4%, saponin 0.08%, Osmium tetroxide 0.075nM and Ir 0.125uM (Fluidigm, #201192A). 966 Finally, samples were washed and resuspended in PBS 0.2% BSA and data were acquired within four days, 967 or frozen in FBS/DMSO 90/10. The antibody panel in Supplemental Table S4 was used to stain bladder 968 cancer patient samples.

969

970 Mass cytometry sample acquisition and processing:

Prior to acquisition, samples were washed with cell staining buffer and acquisition solution
(Standard Biotools). Following washing, samples were resuspended in acquisition solution (1 million cells
/ 1 mL) containing a 1:20 dilution of EQ normalization beads. Data were then acquired using the Standard
Biotools Helios mass cytometer with a wide bore injector configuration at an acquisition speed of < 400
cells per second. The output files were normalized and concatenated using Standard Biotools' CyTOF
software, and outputted as FCS files.

977 The Mount Sinai Human Immune Monitoring Core's (HIMC) pipeline for processing and cleaning 978 was used to clean the resulting FCS files. Aberrant acquisition time-windows and low DNA intensity events 979 were stripped out by the sample preprocessing pipeline. Samples were then demultiplexed via the cosine 980 similarity of the Palladium barcoding channel on a cell-by-cell basis to every possible barcode used in a 981 batch. Once the cell-barcode labeling has been established, the signal-to-noise (SNR) ratio was calculated 982 by taking the difference between the highest and second highest similarity scores. Cells with low SNR 983 ratios were flagged as multiplets and removed. Finally, acquired multiplets are removed based on the 984 Gaussian parameters residual and offset acquired by the Helios mass cytometer.

985

986 Data processing and analysis:

987 Data were uploaded onto Cytobank and processed for downstream analyses. Several gates were 988 applied: a live dead gate and a doublets gate in sequential order. All data were arc-sinh transformed, and 989 no batch corrections were performed given all samples were run in a single batch. NK cells and CD8 T cell 990 subsets were identified via manual gating assignment. Files were downloaded onto Mount Sinai's 991 supercomputing cluster, Minerva, concatenated into a single object, and clinical data were assigned to each 992 sample. A phenograph analysis was performed to cluster the cellular data. Wilcoxon tests were run for 993 statistical significance and the Benjamini-Hochburg correction was applied.

- 994
- 995 '

Tumor Invading Lymphocyte Expansion

996 TILs were expanded by seeding single cells tumor dissociate at 10⁵ cells/well in 48-well Costar® 997 flat-bottom plates (Corning Inc., NY) in complete TIL medium, consisting of RPMI 1640 with L-glutamine 998 (Corning Inc., NY), 10% human AB serum (MiliporeSigma, MO), 1% nonessential amino acids (Thermo 999 Fisher Scientific, MA), 1% sodium pyruvate (Thermo Fisher Scientific, MA), 1% penicillin/streptomycin 1000 (Thermo Fisher Scientific, MA), and 3000 IU/ml interleukin-2 (Proleukin®, kindly provided by Clinigen). 1001 Cells were stimulated using 25 µl ImmunoCult[™] Human CD3/CD28/CD2 T Cell Activator (STEMCELL 1002 Technologies, Vancouver, BC) and seeded on 1.5 x 10⁶ feeder cells, which were derived from healthy 1003 control PBMCs (New York Blood Center, NY) and irradiated at 50 Gy. TILs were incubated at 37°C, 5% 1004 CO₂ and maintained by replacement with fresh complete TIL medium every 2 days. After three weeks, 1005 expanded TIL lines were frozen in 10% DMSO (MiliporeSigma, MO), 90% FBS (MiliporeSigma, MO) 1006 and stored in LN₂.

1007

1008 IFN-γ Stimulation of K562 tumors

1009 Two separate rounds of stimulation were performed on K562 tumors after reaching steady-state 1010 expansion. First, K562 tumors were co-cultured at a concentration of 0.5 X 10⁶ viable cells / mL with 200 1011 and 400 ng / mL of IFN- γ in R10 media in order to assess the induction of HLA-E and PD-L1 with high 1012 doses of IFN-y. At every 24-hour interval, cell concentration and viability were assessed using a 1013 hemocytometer, and K562 tumors were split to a concentration of 0.5 X 10⁶ live cells / mL. At 72 hours of incubation, cells were spun at 1650 RPM, washed with FACS buffer (PBS, 5% FBS, 0.2% EDTA), 1014 1015 resuspended in 5 mL of FACS buffer, and assessed for concentration and viability. 0.5 X 10⁶ live cells were 1016 removed, and spun to remove the FACS buffer. K562 tumors were first incubated with zombie near infrared 1017 (NIR) at a dilution of 1 in 1000 for 20 minutes at room temperature. Following the zombie stain, cells were 1018 washed in 1 mL of FACS buffer, and incubated with PD-L1 (PE; Biolegend cat #124308), and HLA-E (per-1019 CP CY5.5; Biolegend cat #342609) antibodies in a 1:25 dilution cocktail for 30 minutes on ice in the dark. 1020 Cells were washed again in FACS buffer and suspended in 400µLof fixative buffer (2% paraformaldehyde 1021 in PBS). HLA-E and PD-L1 levels were then assessed using flow cytometry.

1022

1023 <u>TIL Co-culture with K562s Expressing Checkpoints</u>

1024 For co-culture and surface stain of PD-L1 and HLA-E, three separate K562 tumor lines of K562 cells 1025 were generated using 400 ng/ml of IFN- γ for 72 hours, as described by the protocol listed above: WT, E+, 1026 and E+/PD-L1+ lines. Tumor-infiltrating lymphocytes (TILs) from four BCG-unresponsive NMIBC 1027 patients which had been expanded using the protocol listed above were thawed and seeded at a 1028 concentration of 1 X 106 live cells / mL in a stimulatory media consisting of ImmunoCult, CD3/CD28 1029 tetramer (25 uL/mL), IL-2 (10 IU/mL), IL-7 (10 ng/mL), and IL-15 (10 ng/mL). Cells were seeded and 1030 plated in a 96 round-bottom plate. At days three, five, seven, and nine, 50% of the media was aspirated and 1031 replaced with fresh media at twice the initial concentration of cytokines, without CD3/28 tetramer. At day 1032 10, TGF-β (Immunocult, IL-2 (10IU/mL), IL-7 (10ng/mL), IL-15 (10ng/mL), CD3/CD28 tetramer 1033 $(25\mu L/mL)$, TGF- β (5ng/mL)) was provided to stimulate expression of NKG2A on the TILS.

At day 13, the stimulation was complete, and the TILs were co-cultured with combinations of the K562 cells expressing forms of PD-L1 and HLA-E. In total, 12 experimental co-culture conditions were conducted for each patients' TIL sample (n=4): two control wells (ex-vivo, and stimulated with a CD3/28 spike); with K562 WT cells, HLA-E⁺ cells, or HLA-E⁺ PD-L1⁺ cells without antibody; TILs in the presence of HLA-E⁺ or HLA-E⁺PD-L1⁺ K562s with durvalumab alone, or both durvalumab plus monalizumab; and lastly, TILs and WT K562s in the presence of monalizumab and durvalumab.

<u>TILs were cultured in TIL medium, consisting of RPMI 1640 with L-glutamine (Corning Inc., NY),</u>
10% human AB serum (MiliporeSigma, MO), 1% nonessential amino acids (Thermo Fisher Scientific,
MA), 1% sodium pyruvate (Thermo Fisher Scientific, MA), 1% penicillin, streptomycin (Thermo Fisher

1043 Scientific, MA). Cultures were performed in 96-well u-bottom plates (Corning Inc., NY). TILs were added 1044 to each well at a concentration of at 3×10^5 cells/condition in TIL medium. K562s were resuspended in TIL 1045 medium and added at 5 x 10⁴ singe-cell equivalents/condition. Anti-CD28 (BioLegend, CA) was added to 1046 each well at 1 µg/ml and anti-CD107a-BV785 (BioLegend, CA) was added to each well at 0.3 µg/ml. 1047 Monalizumab was added to the TILs a final concentration of 10 μ g/ml, and durvalumab was added to the 1048 K562s for a final concentration of 10 µg/ml. TILs and K562s were cultured separately for 20 minutes at 1049 37°C prior to co-culture. The K562s and TILs were then combined, thoroughly resuspended, and gently 1050 spun for 5 seconds before being returned to the incubator. Plates were incubated at 37°C and 5% CO₂, and 1051 after 1 hour of incubation, 0.5X Brefeldin (BioLegend, CA) and 0.5X Monensin (BioLegend, CA) was 1052 added to each tube for a final volume of 500 μ l, followed by an additional 15 hours of incubation. At hour 1053 16 plates were spun and supernatant was removed; all samples were washed with 200µLof PBS. Samples 1054 were resuspended in 50µLof zombie near infrared (NIR) at a 1:3000 dilition, and incubated for 20 minutes 1055 in the dark at room temperature. Samples were washed again, spun, supernatant was removed, and 1056 incubated in 50µLof TruStain FCX, diluted 1:200, for 20 minutes in the dark at 4°C. 50µLof the surface 1057 antibody master mix was added at 20 minutes, and returned to the fridge to incubate in the dark at 4°C for 1058 30 more minutes. Plates were washed twice more in FACS buffer, and were suspended in 0.2% FBS FACS 1059 buffer for storage until intracellular staining.

1060 12 hours prior to acquisition by CyTOF, intracellular staining was performed for IFN- γ . 100 µL of 1061 intracellular staining permeabilization wash buffer (BioLegend) was added to each well, the plates were 1062 spun, and supernatant discarded. This was performed 2 additional times with 200 µL of permeabilization 1063 wash buffer. 50 µL of the intracellular staining antibody mix was added to each well, and the plates were 1064 incubated for 20 minutes at 4°C. The plates were washed in 0.2% FBS FACS buffer and resuspended for 1065 storage in 0.2% FBS FACS buffer.

1066

1067 Data Availability Statement: data were generated by the authors and have been uploaded to the Gene
1068 Expression Omnibus (GSE276014 and GSE276015) and will be made publicly available upon publication
1069 of this manuscript.

1070

1071 ACKNOWLEDGMENTS

We thank Mary Anne O'Donnell (Precision Immunology Institute, Icahn School of Medicine at Mount
Sinai) for critically reviewing the manuscript; Deepta Bhattacharya '(University of Arizona) for kindly
providing HLA-E⁺ K562 tumors. We acknowledge the expertise and assistance of the Dean's Flow
Cytometry Center of Research Excellence at Mount Sinai. The A.H. and J.P. labs were supported by funding

- 1076 from P30CA196521, R01 CA269954-01, R21 CA274148, BCAN No. 961726, and R21AI130760A. The
- 1077 N.B. lab was supported by funding from the Department of Defense Peer Review Cancer Research program
- 1078 Translational team Award No. W81XWH1910269 and from the Parker Institute for Cancer Immunotherapy
- 1079 No.AGR-11611SOW1.
- 1080

1081 AUTHOR CONTRIBUTIONS

- D.R., H.Y., Y.A.W., C.B., J.D., B.S., M.G., N.B., J.P.S., and A.H. conceived the project and experiments,
 analyzed the data and wrote the manuscript. J.P.S., R.M., P.W., M.G., and R.B. provided access to the
 human samples. Additionally, L.D. provided analyses on data derived from human samples at Aarhus
 University Hospital. D.R., H.Y., Y.A.W., C.B., A.D., S.B., W-M.S., J.D., B.S., D-F.R., F.P. E.M., A.T., JA.C-F., B.D.H., T.S., S.V.L., S.H., J.K., performed the experiments or analyzed data. A.M.F, M.T., J.Z.,
 K.G.B, L.W, R.P.S, S.S, Y-C.W, and Y.A.W. collected the RNA sequencing data. D.G., G.K., R.M.d-R,
 B.L., S.K-S. acquired sample data using mass cytometry and Olink proteomics. T.H.T, M.G-B, R.B., E.H-
- 1089 S, E.M.M, C.B., R.F-G, M.S, H.R, A.N., G.D., and J.J.B-C. performed the imaging experiments. S.S., E.C-
- 1090 T., D.P., and S.H. provided intellectual input.
- 1091

1092 DECLARATION OF INTERESTS

L.W., R.P.S., and J.Z. are employees of Sema4. A.H. receives research funds from Astra Zeneca and has
recently served on the advisory boards of Immunorizon, Purple BiotechUroGen, and Takeda. N.B. is an
extramural member of the Parker Institute for Cancer Immunotherapy, receives research funds from
Regeneron, Harbor Biomedical, DC Prime, and Dragonfly Therapeutics and is on the advisory boards of
Neon Therapeutics, Novartis, Avidea, Boehringer Ingelheim, Rome Therapeutics, Rubius Therapeutics,
Roswell Park Comprehensive Cancer Center, BreakBio, Carisma Therapeutics, CureVac, Genotwin,
BioNTech, Gilead Therapeutics, Tempest Therapeutics, and the Cancer Research Institute.

1100

1101 LEGENDS TO FIGURES

1102

Fig. 1: Chronic activation within the tumor microenvironment of BCG-unresponsive tumorspromotes adaptive resistance.

- 1105 A, Targeted mRNA gene-set enrichment analysis showing statistically significant differences between
- 1106 BCG-naïve (N=20) and BCG-unresponsive cases (N=20). All gene sets are significant at p<0.05 by
- 1107 Kruskal-Wallis or independent two-sided t-test.

B, Longitudinal protein analysis of urine supernatants across four timepoints in BCG-naïve patients with
 NMIBC (N=27) with comparisons between BCG-naïve and 6th induction dose timepoints (* p<0.05, **
 p<0.001).

1111 C, An additional validation cohort of patients with NMIBC receiving BCG therapy at Aarhus University
1112 (N=66) showing BCG-naïve vs BCG-exposed timepoints in urine samples (p-values in both cohorts
1113 assessed via independent two-sided t-test or Kruskal-Wallis with Benjamini-Hochberg correction for
1114 multiple comparisons).

- 1115 **D**, Differential protein expression analysis of urine before (top row) and after (bottom row) BCG exposure 1116 and sampled before (left-side) and after (right-side) transurethral resection of bladder tumors. Number of 1117 patients included in analyses: (Top-left) BCG-naïve when tumor present, non-responders, N= 47; 1118 responders, N=60. (Top-right) BCG-naïve after tumor resection, non-responders, N=5; responders, N=6. (Bottom-left) BCG-exposed when tumor present, non-responders, N= 49; responders, N= 34. (Bottom-1119 1120 right) BCG-exposed after tumor-resection, non-responders, N= 19; responders, N= 26. P-values assessed 1121 with two-sided Wilcoxon rank sum. Proteins listed in orange text indicate unadjusted p-values <0.05. BCG-1122 unresponsive NMIBC was defined as high-grade recurrence within two years after receiving BCG therapy. E, Median fluorescence intensity (MFI) for PD-L1 and HLA-E staining on primary CD45- cells from 1123 1124 patients with NMIBC and immortalized bladder tumor lines ex vivo or after 24 hours of incubation with 1125 recombinant human (rh) IFN-g stimulation (all comparisons, p<0.05). All stimulation experiments were 1126 performed in triplicate.
- 1127

Fig: 2: HLA-E tumor expression is highest when near tumor-infiltrating NKG2A⁺ NK and CD8 T cells.

1130 A, Representative multiplexed immunofluorescence (IF) analysis by PhenoCyclerTM (also known as

1131 CODEX) of bladder tumor sections from one patient with BCG-unresponsive NMIBC. Representative

staining of the entire section is shown for presence of stroma (vimentin, blue) and tumor (S100A4, yellow).

- **1133** Scale bar indicates 2mm.
- **B**, Magnified inset from Panel A, highlighting tumor HLA-E expression of and use of digital pathology

software to identify NKp46⁺ NK and CD8 T cells with and without co-expression of NKG2A +/- PD-1.

1136 Left image scale bar indicates 400µm and right image scale bar indicates 50µm.

1137 C, Magnified inset from Panel B, right image, highlighting individual cells expressing CD8, PD-1, and

1138 NKG2A. Scale bars indicate 20µm.

1139 D, Representative multiplexed immunohistochemistry (IHC) of bladder tumor from one patient with BCG-

- unresponsive NMIBC measuring expression of pan-cytokeratin (pan-CK), HLA-E, CD3, and NKG2A.
- 1141 Scale bar indicates 100µm.
- 1142 E, Representative digital pathology analyses identifying tumor (red) and adjacent/non-tumor (green) tissue
- along with exposed areas of glass (yellow) to be excluded from subsequent analyses. Scale bar indicates1144 1mm.
- 1145 F, Density map highlighting regions of high HLA-E tumor expression. Blue-red color scale indicates HLA-
- 1146 E expression intensity. Scale bar indicates 1mm.
- G, Summary analysis of frequency of tumor cells that are HLA-E-bright (green) and HLA-E-dim/negative
 (dim/neg, yellow) in BCG-naïve (N=17) and BCG-unresponsive (unresp., N=24) NMIBC tumors.
- 1149 H, Representative digital pathology analysis on one BCG-naïve (top row) and one BCG-unresponsive
- 1150 (bottom row) NMIBC tumor section highlighting nuclear expression of DAPI (blue) and identification of
- 1151 CD3+NKG2A+ CD8 T cells (black), CD3- NKG2A+ NK cells (red), and tumor cells with bright (green) or
- 1152 dim/negative (yellow) expression of HLA-E.
- 1153 I, Proximity analysis (N=41) measuring cell distance (0-150µm) from HLA-E-bright and HLA-E-
- dim/negative tumors by NKG2A+ NK cells (left side) and NKG2A+ T cells (right side). ****, p<0.00001.
- 1155 P-values were assessed via independent two-sided t-test.
- 1156 J, Representative proximity ligation assay (PLA) using immunofluorescence to profile interactions between
- 1157 HLA-E and NKG2A in one BCG-naïve (top row) and one BCG-unresponsive (bottom row) patient with
- 1158 NMIBC.
- 1159 K, Summary analysis of PLA measuring interactions between HLA-E and NKG2A. P-values were assessed
 1160 via independent two-sided t-test.
- 1161
- 1162

Fig. 3: Single-cell RNA sequencing analysis of NKG2A⁺ NK and CD8 T cells from bladder tumors reveals strong antitumor potential but with co-expression of inhibitory receptors.

- 1165 A, UMAP visualization of cell lineages from single-cell RNA sequencing analysis of urothelial tumor samples (N=9,
- **1166** 65,324 cells).
- **1167 B**, Heatmap summary of genes most differentially expressed on each cell lineage identified.
- 1168 C, Differentially expressed gene (DEG) analysis of bladder tumor-derived NK cells (left), CD8 T cells
- 1169 (center), and proliferating T cell cycle cells (right) when stratified by high versus dim/negative KLRC1
- 1170 expression.

- 1171 D and E, UMAP visualizations of bladder tumor-derived NK cells from unsupervised clustering revealing
- (D) five clusters or (E) expression of *NCAM1*/CD56 for annotation of CD56^{BRIGHT} and CD56^{DIM} NK cells
 (N=2,580 cells).
- 1174 F, Pathway analysis of Hallmark gene networks that are significantly differentially expressed (at least
- p<0.05) on bladder tumor-derived CD56^{BRIGHT} and CD56^{DIM} NK cells. P-values were determined using a
 two-sided t-test.
- 1177 G and H, UMAP visualization of bladder tumor-derived NK cells (G) clustered according to Groups 1-6
- defined by Netskar et al. ³⁰ and (H) highlighting expression and distribution of representative tissue
 residency genes.
- 1180 I, Heatmap summary showing average expression for genes associated with tissue residency, chemokines,
- 1181 cytokines, and their receptors on bladder tumor-derived Group 1-6 NK cells (top heatmap) and CD8 T cells
- and T cell cycle cells when stratified according to *KLRC1* expression (bottom heatmap).
- 1183

Fig. 4: Single-cell RNA sequencing analysis of bladder tumor cells reveals functional differences that segregate the tumor microenvironment.

- **A**, UMAP visualization of bladder tumor cells from unsupervised clustering revealing seven clusters (B1B7).
- 1188 B, UMAP visualization of HLA-E expression defined by tertiles, highlighting the top tertile (red dots) as
- 1189 HLA-E-bright (N=5,461) and bottom tertile (blue dots) as HLA-E-dim/negative (N=9,256) tumor cells.
- 1190 C, Pathway analysis of Hallmark gene networks that are significantly differentially expressed (at least
- p<0.05) on HLA-E-bright and HLA-E-dim/negative bladder tumor cells. P-values were determined using
 a two-sided t-test.
- 1193 D, Bubble plot showing targeted gene expression across bladder tumor clusters B1-B7 and stratified by
- 1194 HLA-E^{HIGH} or HLA-E^{LOW} tumor clusters. Size of bubble indicates percent of cluster or group and color
- 1195 indicates average gene expression.
- 1196 E, Scatterplot highlighting pseudobulking of bladder tumor cells and expression of HLA-E and ACKR3
- 1197 (CXCR7). P-value was determined using a two-sided correlation.
- 1198 F, Stacked bar plot showing the frequency of bladder tumor clusters, B1-B7 that are identified in BCG-
- 1199 naïve (green) and BCG-unresponsive (grey) NMIBC tumors.
- 1200 G, Heatmap summary of average gene expression of select chemokines, chemokine receptors, amphiregulin
- 1201 (AREG) and EGFR across all major clusters identified by scRNAseq of bladder tumors (N=9, 65, 324 cells).
- 1202 H, Ligand-receptor interaction analysis of KLRC1^{HIGH} cells (NK cells, CD8 T cells, T cell cycle) and HLA-
- 1203 *E*-bright tumor cells (schematic diagram at top) showing the top 12 ranked ligands by KLRC1-expressing

1204 cells and cognate receptors expressed by HLA- E^{HIGH} tumor cells. Ligand-receptor pairs were selected by 1205 rank-ordering and using cut-off weight of 0.2.

- 1206 I, Circos plot showing top ranked ligands by KLRC1-expressing cells at the bottom and significant genes
- 1207 expressed by HLA- E^{HIGH} tumor cells as a result of ligand-receptor interactions highlighting putative effects
- 1208 of the HLA-E/NKG2A axis (top) or the *IFNG*-mediated (middle) or *AREG*-mediated (bottom) resistance
- signatures.
- 1210

1211 Fig. 5: Spatial analysis of NMIBC tumors reveals an organization within the TME.

- 1212 A and B, UMAP visualization of spatial transcriptomics sequencing (ST-seq) analysis of BCG-naïve (N=4)
- and BCG-unresponsive (N=4) NMIBC tumors identifying 12 ST-clusters and their distributions acrossNMIBC specimens.
- 1215 C, Bubble plot showing ST-clusters 1-11 (rows) and their relative composition across immune, stromal,
- and tumor subtypes (columns) as defined by scRNAseq analysis. Size of bubble indicates its relative
- 1217 enrichment and shading of surrounding boxes indicate significance by FDR (corrected p values).
- 1218 D, Representative ST-seq images showing the distribution of ST-clusters 1-11 in one BCG-naïve (left) and
- 1219 one BCG-unresponsive (right) NMIBC tumor specimens.
- 1220 E, Summary histogram comparing relative enrichment of each ST-cluster in BCG-naïve (grey, N=4) and
- 1221 BCG-unresponsive (green, N=4) NMIBC tumor specimens.
- 1222 F, Schematic diagram illustrating deconvolution of NK cells and tumor cells across 10x Visium spots.
- 1223 Cutoff of 20% of spot's composition was used for defining a true signal.
- 1224 G and H, Representative ST-seq images from one BCG-naïve (left) and one BCG-unresponsive (right)
- 1225 NMIBC tumor specimens showing proximity analyses of *HLA-E*^{LOW} (black circles) and *HLA-E*^{HIGH} (red
- 1226 circles) tumor cells to (G) NK/CD8 T cells (blue spots) or (H) NK cells, CD8 T cells, and Tregs alone or
- in combination (colored spots).
- I, Summary comparisons of proximity of *HLA-E^{HIGH}* (red bars) and *HLA-E^{LOW}* (grey bars) tumor cells to
 NK cells (left), Tregs (middle) and CD8 T cells (right). P-values were determined using two-sided
 Wilcoxon test.
- 1231

Fig. 6: Recruitment of *HLA-E*^{HIGH} tumor cells to stromal regions replete with immune infiltration correlates with BCG-unresponsive NMIBC.

- 1234 A-C, Representative ST-seq images from one BCG-unresponsive NMIBC tumor highlighting (A)
- 1235 proximity of NK cells, CD8 T cells, and Tregs to tumor and stromal cells according to *HLA-E* expression,
- 1236 (B) overlaid topographical map of *HLA-E* tumor/stromal cell expression with color indicating abundance

- 1237 of NK and cytolytic CD8 T cells, and (C) proximity of NK cells, CD8 T cells, and Tregs to myeloid cells
- 1238 expressing any combination of *CXCL9*, *CXCL10*, and/or *CXCL11*.
- 1239 D, Correlation analysis of Visium spots, defined as tumor cell with or without stromal cells, for co-
- 1240 expression of CXCL9 and HLA-E expression in BCG-naïve (N=4, left) and BCG-unresponsive (N=4, right)
- 1241 NMIBC tumor specimens.
- 1242 E, Correlation analysis of Visium spots, defined as tumor cell with or without stromal cells, for co-
- 1243 expression of CXCL12 and HLA-E expression in BCG-naïve (N=4, left) and BCG-unresponsive (N=4,
- 1244 right) NMIBC tumor specimens.
- F, Meta-analysis of all tumor/stroma-labelled Visium spots showing row-scaled expression of pertinent genes
 stratified by number of neighboring infiltrating NK cells and/or CD8 T-cells.
- 1247 G, Z-scored heatmap showing HLA- E^{LOW} , low-cytotoxic infiltrating tumor spots (N = 1,200 Visium spots) vs HLA-

1248 E^{HIGH} and high-NK/CD8 T cell-infiltrated tumor spots (N = 242 Visium spots).

- 1249 H, Representative multiplexed IF analysis by PhenoCycler[™] of bladder tumor sections from one patient
- 1250 with BCG-unresponsive NMIBC highlighting the presence of stroma (vimentin, blue) and tumor (S100A4,
- 1251 yellow). Scale bar indicates 2mm.
- 1252 I, Magnified inset from Panel H, highlighting tumor S100A4 expression of and use of digital pathology
- 1253 software to identify NKG2A⁺ NK and CD8 T cells along FoxP3+ CD4+ Tregs, macrophages (CD68 and
- 1254 CD163) and dendritic cells (CD11c and/or HLA-DR). Image scale bar indicates 20µm.
- 1255

Fig. 7: In vitro combination NKG2A and PD-L1 blockade restores tumor-derived NK and CD8 T cell-mediated antitumor activity.

- 1258 A, Median fluorescence intensity (MFI) of HLA-E and PD-L1 expression by wild-type (WT) or HLA-E⁺
- 1259 K562 tumors cultured overnight in the presence or absence of recombinant human IFN- γ .
- **B** and C, Phenograph clustering meta-analysis of tumor-derived and expanded CD56⁺ CD8 T cells by
- 1261 CyTOF before co-culture with K562 tumors showing **B**, tSNE analysis of identified CD8 T cell clusters,
- and C, expression of individual inhibitory and activating receptors by CD8 T cells and their distribution
- across clusters.
- 1264 D, Representative CyTOF analysis of CD56 and NKG2A expression on tumor-derived NK (top row) and
- 1265 CD8 T cells (bottom row) profiled before (left column) and after (right column) expansion with low dose1266 recombinant human IL-2, IL-7, IL-15 and CD3/CD28 tetramers.
- 1267 E, Representative fluorescence flow cytometric analysis of IFN-g and CD107a expression by CD56⁺ NK
- 1268 (top row) and CD8 T cells (bottom row) after 6-hour culture alone or in presence of K562 tumor lines with
- 1269 or without pre-treatment with anti-PD-L1 antibodies or with anti-PD-L1 + anti-NKG2A antibodies.

- 1270 F, Fold-change differences between the frequencies of NK and CD56⁺ CD8 T cells when comparing
- 1271 between experimental conditions (defined by "+"). Individual comparisons are indicated at the bottom. *,
- 1272 p<0.05; **, p<0.001. P values determined by paired Wilcoxon matched rank test.

1273

1275

1277 References

1280

1283

1287

1291

1294

1297

1300

1303

1306

1309

1312

- 12781.Redelman-Sidi, G., Glickman, M.S. & Bochner, B.H. The mechanism of action of BCG1279therapy for bladder cancer--a current perspective. Nat Rev Urol 11, 153-162 (2014).
- 12812.Kamat, A.M. *et al.* Predicting Response to Intravesical Bacillus Calmette-Guerin1282Immunotherapy: Are We There Yet? A Systematic Review. *Eur Urol* **73**, 738-748 (2018).
- 12843.Müller, G. et al. Association between Development of Metabolic Acidosis and1285Improvement of Urinary Continence after Ileal Neobladder Creation. J Urol 203, 585-5901286(2020).
- Hedgepeth, R.C., Gilbert, S.M., He, C., Lee, C.T. & Wood, D.P., Jr. Body image and bladder
 cancer specific quality of life in patients with ileal conduit and neobladder urinary
 diversions. Urology **76**, 671-675 (2010).
- 12925.Morales, A. BCG: A throwback from the stone age of vaccines opened the path for bladder1293cancer immunotherapy. Can J Urol 24, 8788-8793 (2017).
- 12956.Zlotta, A.R. *et al.* What is the optimal regimen for BCG intravesical therapy? Are six weekly1296instillations necessary? *Eur Urol* **37**, 470-477 (2000).
- Sfakianos, J.P. *et al.* Bacillus Calmette-Guerin (BCG): Its fight against pathogens and cancer.
 Urol Oncol 39, 121-129 (2021).
- 13018.Sharma, P., Hu-Lieskovan, S., Wargo, J.A. & Ribas, A. Primary, Adaptive, and Acquired1302Resistance to Cancer Immunotherapy. *Cell* **168**, 707-723 (2017).
- 13049.Gocher, A.M., Workman, C.J. & Vignali, D.A.A. Interferon-γ: teammate or opponent in the1305tumour microenvironment? Nat Rev Immunol (2021).
- 130710.Benci, J.L. *et al.* Opposing Functions of Interferon Coordinate Adaptive and Innate Immune1308Responses to Cancer Immune Checkpoint Blockade. *Cell* **178**, 933-948.e914 (2019).
- 131011.Wang, L. *et al.* Myeloid Cell-associated Resistance to PD-1/PD-L1 Blockade in Urothelial1311Cancer Revealed Through Bulk and Single-cell RNA Sequencing. *Clin Cancer Res* (2021).
- 131312.Strandgaard, T. et al. Field Cancerization Is Associated with Tumor Development, T-cell1314Exhaustion, and Clinical Outcomes in Bladder Cancer. Eur Urol (2023).
- 131613.Strandgaard, T. et al. Elevated T-cell Exhaustion and Urinary Tumor DNA Levels Are1317Associated with Bacillus Calmette-Guérin Failure in Patients with Non–muscle-invasive1318Bladder Cancer. European Urology (2022).
- 1319

- 1320 14. Kates, M. *et al.* Adaptive Immune Resistance to Intravesical BCG in Non-Muscle Invasive
 1321 Bladder Cancer: Implications for Prospective BCG-Unresponsive Trials. *Clin Cancer Res* 26,
 1322 882-891 (2020).
- 132415.Rosenberg, J.E. *et al.* Atezolizumab in patients with locally advanced and metastatic1325urothelial carcinoma who have progressed following treatment with platinum-based1326chemotherapy: a single-arm, multicentre, phase 2 trial. *Lancet* **387**, 1909-1920 (2016).
- 1328 16. Powles, T. *et al.* Efficacy and Safety of Durvalumab in Locally Advanced or Metastatic
 1329 Urothelial Carcinoma: Updated Results From a Phase 1/2 Open-label Study. *JAMA Oncol*1330 3, e172411 (2017).
- 133217.Sharma, P. et al. Nivolumab in metastatic urothelial carcinoma after platinum therapy1333(CheckMate 275): a multicentre, single-arm, phase 2 trial. Lancet Oncol 18, 312-3221334(2017).
- 1336 18. Patel, M.R. *et al.* Avelumab in metastatic urothelial carcinoma after platinum failure
 1337 (JAVELIN Solid Tumor): pooled results from two expansion cohorts of an open-label, phase
 1338 1 trial. *Lancet Oncol* **19**, 51-64 (2018).
- 134019.Grossman, J.E., Vasudevan, D., Joyce, C.E. & Hildago, M. Is PD-L1 a consistent biomarker1341for anti-PD-1 therapy? The model of balstilimab in a virally-driven tumor. Oncogene 40,13421393-1395 (2021).
- 134420.Kamiya, T., Seow, S.V., Wong, D., Robinson, M. & Campana, D. Blocking expression of1345inhibitory receptor NKG2A overcomes tumor resistance to NK cells. J Clin Invest 129, 2094-13462106 (2019).
- 134821.Pereira, B.I. *et al.* Senescent cells evade immune clearance via HLA-E-mediated NK and1349CD8(+) T cell inhibition. *Nat Commun* **10**, 2387 (2019).
- 135122.van Montfoort, N. *et al.* NKG2A Blockade Potentiates CD8 T Cell Immunity Induced by1352Cancer Vaccines. *Cell* **175**, 1744-1755.e1715 (2018).
- 135423.Andre, P. et al. Anti-NKG2A mAb Is a Checkpoint Inhibitor that Promotes Anti-tumor1355Immunity by Unleashing Both T and NK Cells. Cell **175**, 1731-1743 e1713 (2018).
- 135724.Salomé, B. *et al.* NKG2A and HLA-E define a novel alternative immune checkpoint axis in1358bladder cancer. *Cancer Cell* **40**, 1-17 (2022).
- 136025.Herbst, R.S. et al. COAST: An Open-Label, Phase II, Multidrug Platform Study of1361Durvalumab Alone or in Combination With Oleclumab or Monalizumab in Patients With1362Unresectable, Stage III Non-Small-Cell Lung Cancer. J Clin Oncol, JCO2200227 (2022).
- 1363

1323

1327

1331

1335

1339

1343

1347

1350

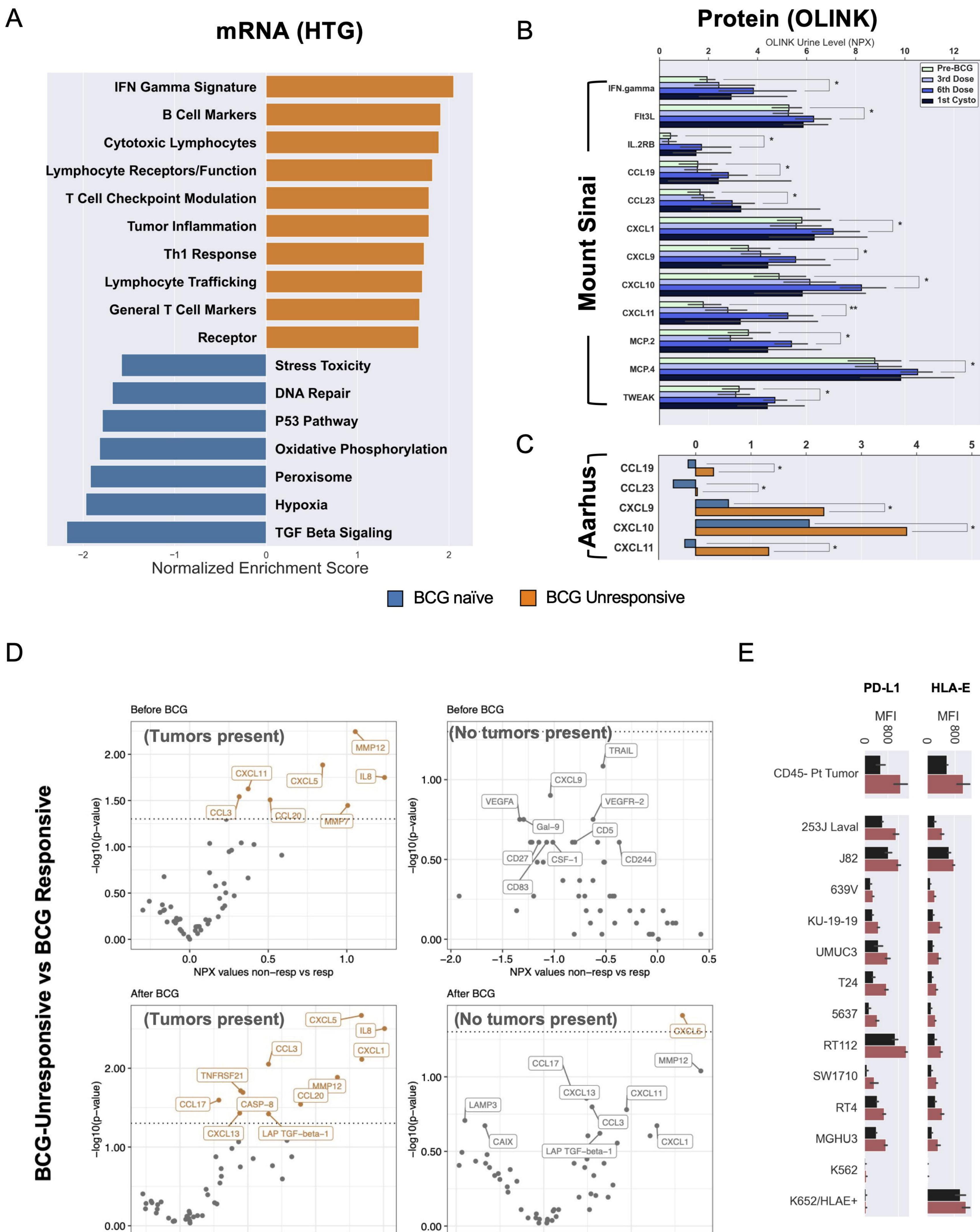
1353

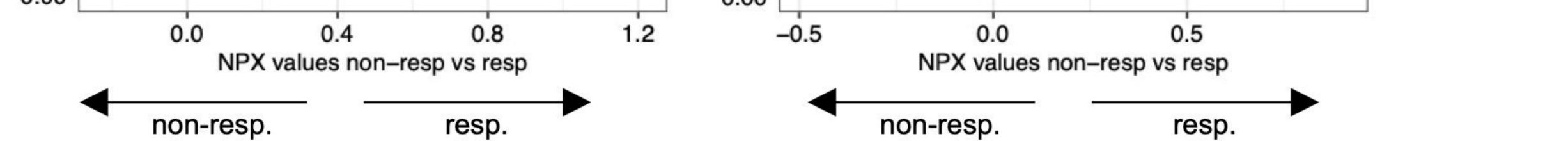
1356

1364 1365 1366	26.	Rouanne, M. et al. BCG therapy downregulates HLA-I on malignant cells to subvert antitumor immune responses in bladder cancer. J Clin Invest 132 (2022).
1367 1368 1369	27.	Liberzon, A. <i>et al.</i> The Molecular Signatures Database (MSigDB) hallmark gene set collection. <i>Cell Syst</i> 1 , 417-425 (2015).
1370 1371 1372 1373	28.	Jiang, Y.H. <i>et al.</i> Urine cytokines as biomarkers for diagnosing interstitial cystitis/bladder pain syndrome and mapping its clinical characteristics. <i>Am J Physiol Renal Physiol</i> 318 , F1391-f1399 (2020).
1374 1375 1376	29.	Tyagi, P. <i>et al.</i> Urine cytokines suggest an inflammatory response in the overactive bladder: a pilot study. <i>Int Urol Nephrol</i> 42 , 629-635 (2010).
1377 1378 1379	30.	Netskar, H. et al. Pan-cancer profiling of tumor-infiltrating natural killer cells through transcriptional reference mapping. Nat Immunol (2024).
1375 1380 1381 1382	31.	Rebuffet, L. <i>et al.</i> High-dimensional single-cell analysis of human natural killer cell heterogeneity. <i>Nat Immunol</i> (2024).
1382 1383 1384	32.	Vivier, E. et al. Natural killer cell therapies. Nature 626, 727-736 (2024).
1385 1386 1387	33.	Browaeys, R., Saelens, W. & Saeys, Y. NicheNet: modeling intercellular communication by linking ligands to target genes. <i>Nat Methods</i> 17 , 159-162 (2020).
1388 1389	34.	Amir el, A.D. <i>et al.</i> viSNE enables visualization of high dimensional single-cell data and reveals phenotypic heterogeneity of leukemia. <i>Nat Biotechnol</i> 31 , 545-552 (2013).
1390 1391 1392	35.	Cristescu, R. <i>et al.</i> Pan-tumor genomic biomarkers for PD-1 checkpoint blockade-based immunotherapy. <i>Science</i> 362 (2018).
1393 1394 1395 1396 1397	36.	Spranger, S. <i>et al.</i> Up-regulation of PD-L1, IDO, and T(regs) in the melanoma tumor microenvironment is driven by CD8(+) T cells. <i>Sci Transl Med</i> 5 , 200ra116-200ra116 (2013).
1398 1399 1400 1401	37.	Rooney, M.S., Shukla, S.A., Wu, C.J., Getz, G. & Hacohen, N. Molecular and genetic properties of tumors associated with local immune cytolytic activity. <i>Cell</i> 160 , 48-61 (2015).
1402 1403	38.	Ribas, A. Adaptive Immune Resistance: How Cancer Protects from Immune Attack. <i>Cancer Discov</i> 5 , 915-919 (2015).
1404 1405 1406 1407	39.	Grasso, C.S. <i>et al.</i> Conserved Interferon-γ Signaling Drives Clinical Response to Immune Checkpoint Blockade Therapy in Melanoma. <i>Cancer Cell</i> 38 , 500-515.e503 (2020).

1408 1409 1410	40.	Gocher, A.M., Workman, C.J. & Vignali, D.A.A. Interferon-γ: teammate or opponent in the tumour microenvironment? <i>Nat Rev Immunol</i> 22 , 158-172 (2022).
1411 1412 1413	41.	Bardia, A. <i>et al.</i> Sacituzumab Govitecan in Metastatic Triple-Negative Breast Cancer. <i>N Engl J Med</i> 384 , 1529-1541 (2021).
1414 1415 1416	42.	Powles, T. et al. Enfortumab Vedotin and Pembrolizumab in Untreated Advanced Urothelial Cancer. N Engl J Med 390 , 875-888 (2024).
1417 1418 1419	43.	Heath, E.I. & Rosenberg, J.E. The biology and rationale of targeting nectin-4 in urothelial carcinoma. <i>Nat Rev Urol</i> 18 , 93-103 (2021).
1420 1421 1422	44.	Chang, S.S. <i>et al.</i> Diagnosis and Treatment of Non-Muscle Invasive Bladder Cancer: AUA/SUO Guideline. <i>J Urol</i> 196 , 1021-1029 (2016).
1422 1423 1424 1425 1426	45.	Bisiaux, A. <i>et al.</i> Molecular analyte profiling of the early events and tissue conditioning following intravesical bacillus calmette-guerin therapy in patients with superficial bladder cancer. <i>J Urol</i> 181 , 1571-1580 (2009).
1420 1427 1428 1429	46.	Shapiro, S.S. & Wilk, M.B. An Analysis of Variance Test for Normality (Complete Samples). <i>Biometrika</i> 52 , 591-611 (1965).
1430 1431 1432	47.	Kruskal, W.H. & Wallis, W.A. Use of Ranks in One-Criterion Variance Analysis. <i>Journal of the American Statistical Association</i> 47 , 583-621 (1952).
1433 1434 1435	48.	Zhang, X. et al. CellMarker: a manually curated resource of cell markers in human and mouse. Nucleic Acids Res 47, D721-d728 (2019).
1435 1436 1437 1438	49.	Glass, D.R. <i>et al.</i> An Integrated Multi-omic Single-Cell Atlas of Human B Cell Identity. Immunity 53 , 217-232.e215 (2020).
1438 1439 1440 1441 1442	50.	Magri, G. <i>et al.</i> Human Secretory IgM Emerges from Plasma Cells Clonally Related to Gut Memory B Cells and Targets Highly Diverse Commensals. <i>Immunity</i> 47 , 118-134.e118 (2017).
1443 1444 1445	51.	Hao, Y. et al. Dictionary learning for integrative, multimodal and scalable single-cell analysis. Nature biotechnology 42 , 293-304 (2024).
1445 1446 1447 1448 1449	52.	Finak, G. <i>et al.</i> MAST: a flexible statistical framework for assessing transcriptional changes and characterizing heterogeneity in single-cell RNA sequencing data. <i>Genome biology</i> 16 , 1-13 (2015).
1450 1451	53.	Liberzon, A. <i>et al.</i> Molecular signatures database (MSigDB) 3.0. <i>Bioinformatics</i> 27 , 1739- 1740 (2011).

1452		
1453	54.	Rouillard, A.D. et al. The harmonizome: a collection of processed datasets gathered to
1454		serve and mine knowledge about genes and proteins. Database (Oxford) 2016 (2016).
1455		
1456	55.	Galon, J. et al. Affinity of the interaction between Fc gamma receptor type III (Fc
1457		gammaRIII) and monomeric human IgG subclasses. Role of Fc gammaRIII glycosylation.
1458		Eur J Immunol 27 , 1928-1932 (1997).
1459		
1460	56.	Liberzon, A. et al. Molecular signatures database (MSigDB) 3.0. Bioinformatics 27, 1739-
1461		1740 (2011).
1462		
1463	57.	Dries, R. et al. Giotto: a toolbox for integrative analysis and visualization of spatial
1464		expression data. Genome biology 22 , 1-31 (2021).
1465		
1466	58.	Lause, J., Berens, P. & Kobak, D. Analytic Pearson residuals for normalization of single-cell
1467		RNA-seq UMI data. <i>Genome biology</i> 22, 1-20 (2021).
1468		
1469	59.	Korsunsky, I. et al. Fast, sensitive and accurate integration of single-cell data with
1470		Harmony. <i>Nature methods</i> 16, 1289-1296 (2019).
1471	60	
1472	60.	Ma, Y. & Zhou, X. Spatially informed cell-type deconvolution for spatial transcriptomics.
1473		Nature biotechnology 40 , 1349-1359 (2022).
1474 1475	61	lin S. Dikus MV & Nig O. CollChat for systematic analysis of coll call communication
1475	61.	Jin, S., Plikus, M.V. & Nie, Q. CellChat for systematic analysis of cell-cell communication from single-cell and spatially resolved transcriptomics. <i>BioRxiv</i> , 2023.2011. 2005.565674
1470		(2023).
1477		(2023).
1478		
1480		

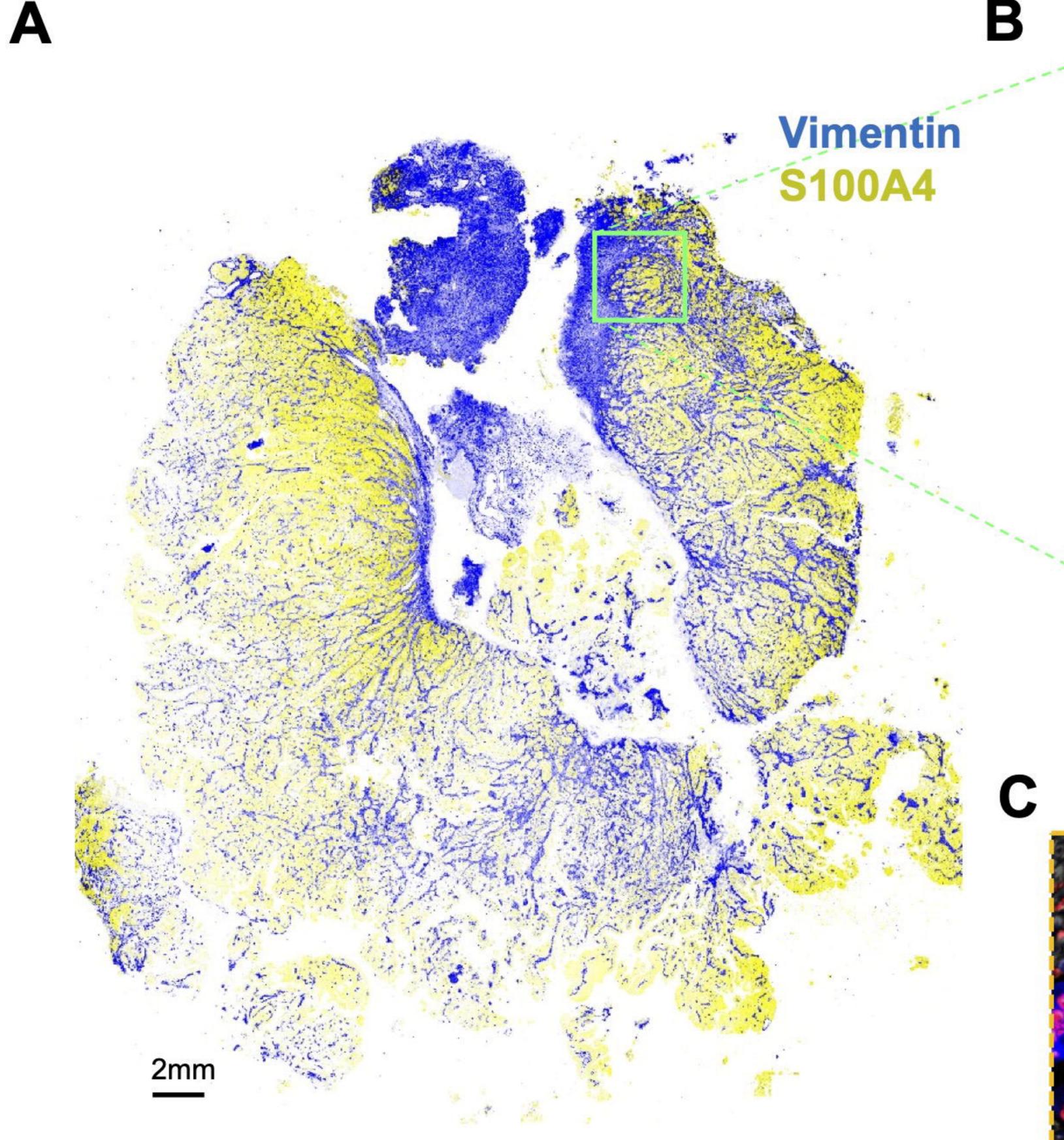


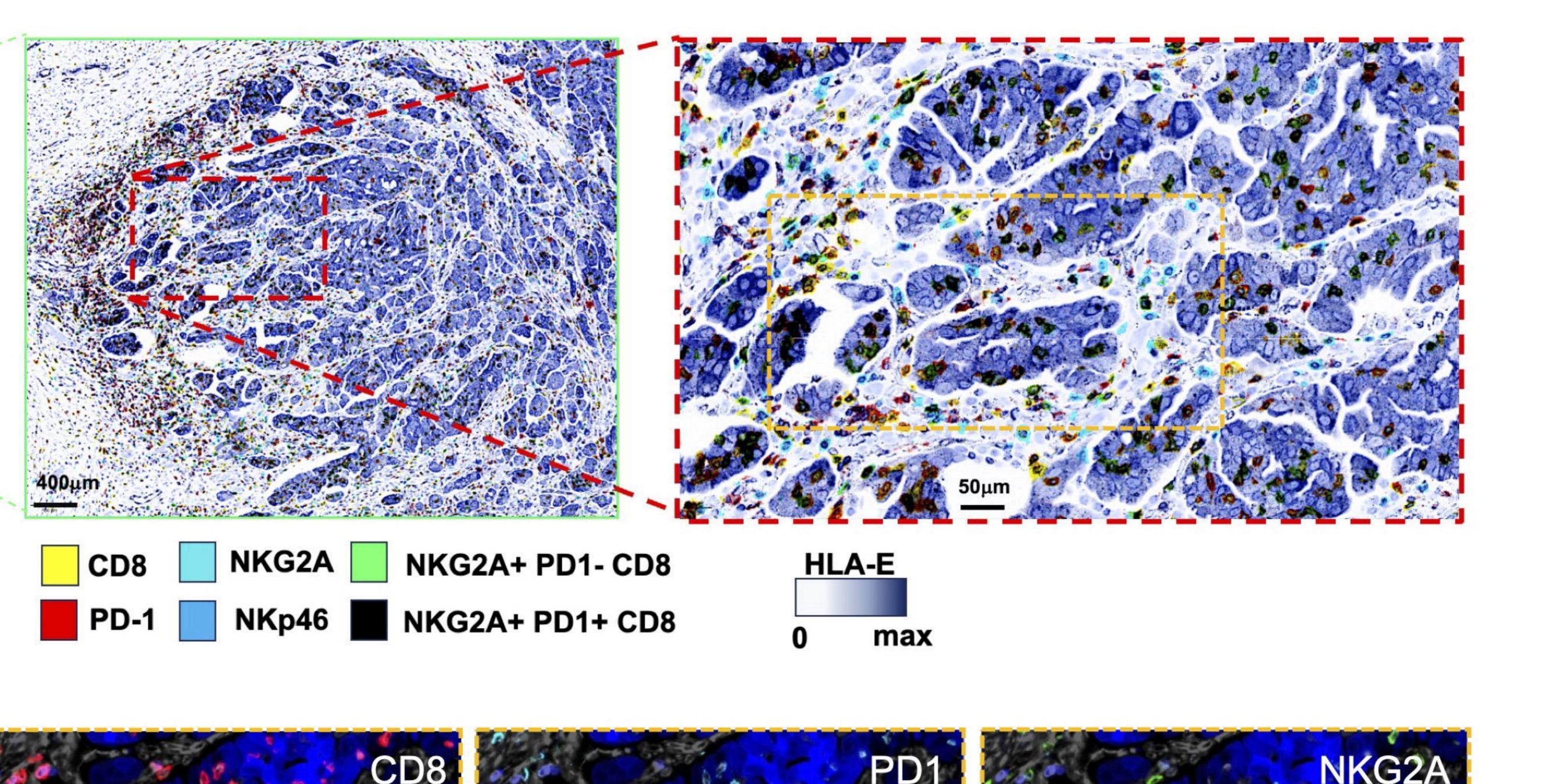


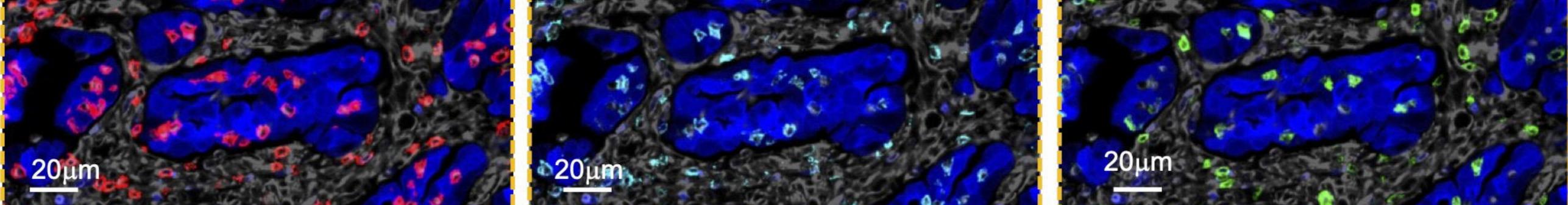
Ex-Vivo IFN-G Stimulation

bioRxiv preprint doi: https://doi.org/10.1101/2024.09.02.610816; this version posted September 3, 2024. The copyright holder for this preprint (which was not certified by peer review) is the author/funder, who has granted bioRxiv a license to display the preprint in perpetuity. It is made available under aCC-BY-ND 4.0 International license.

Figure 1.

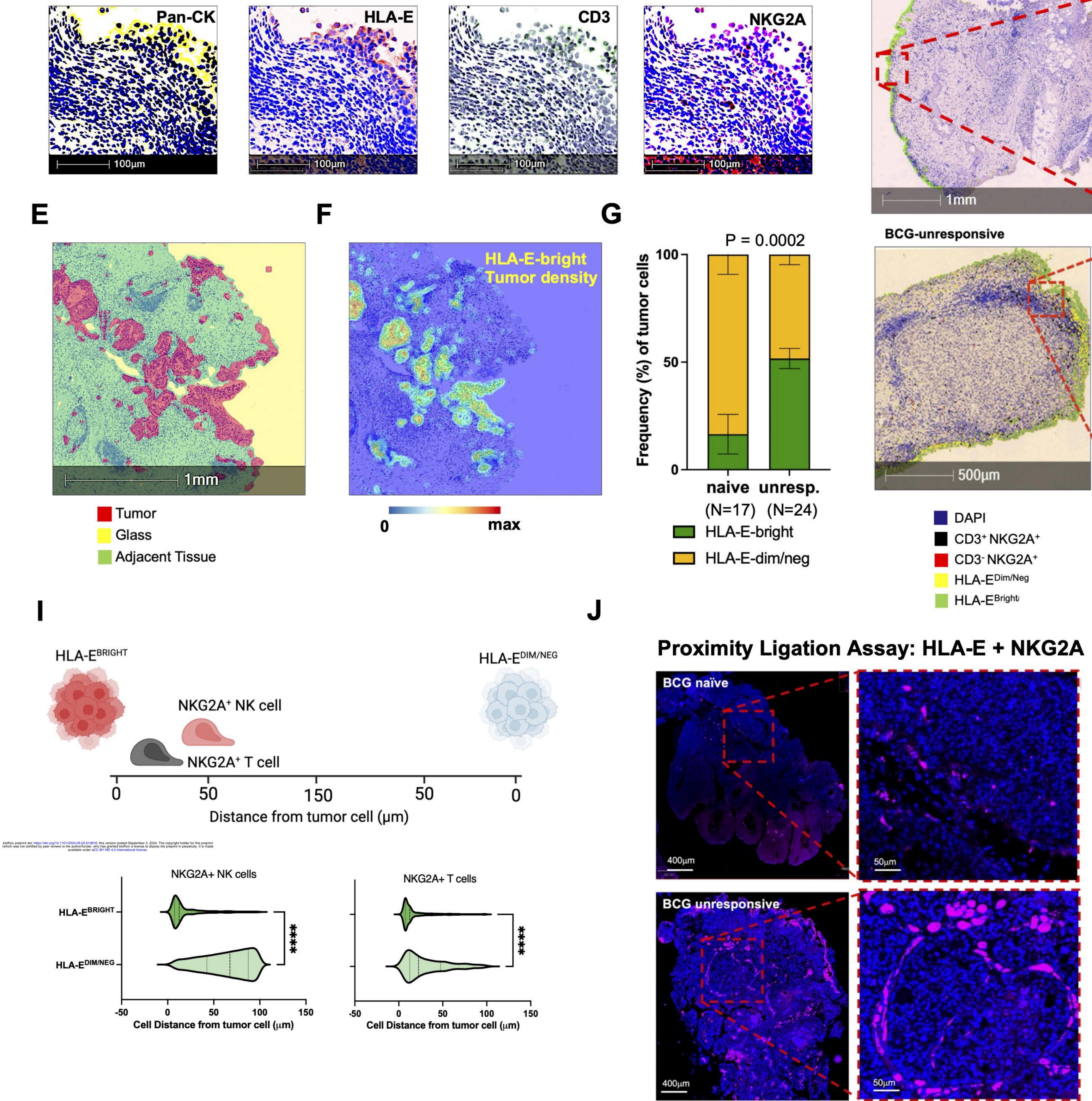


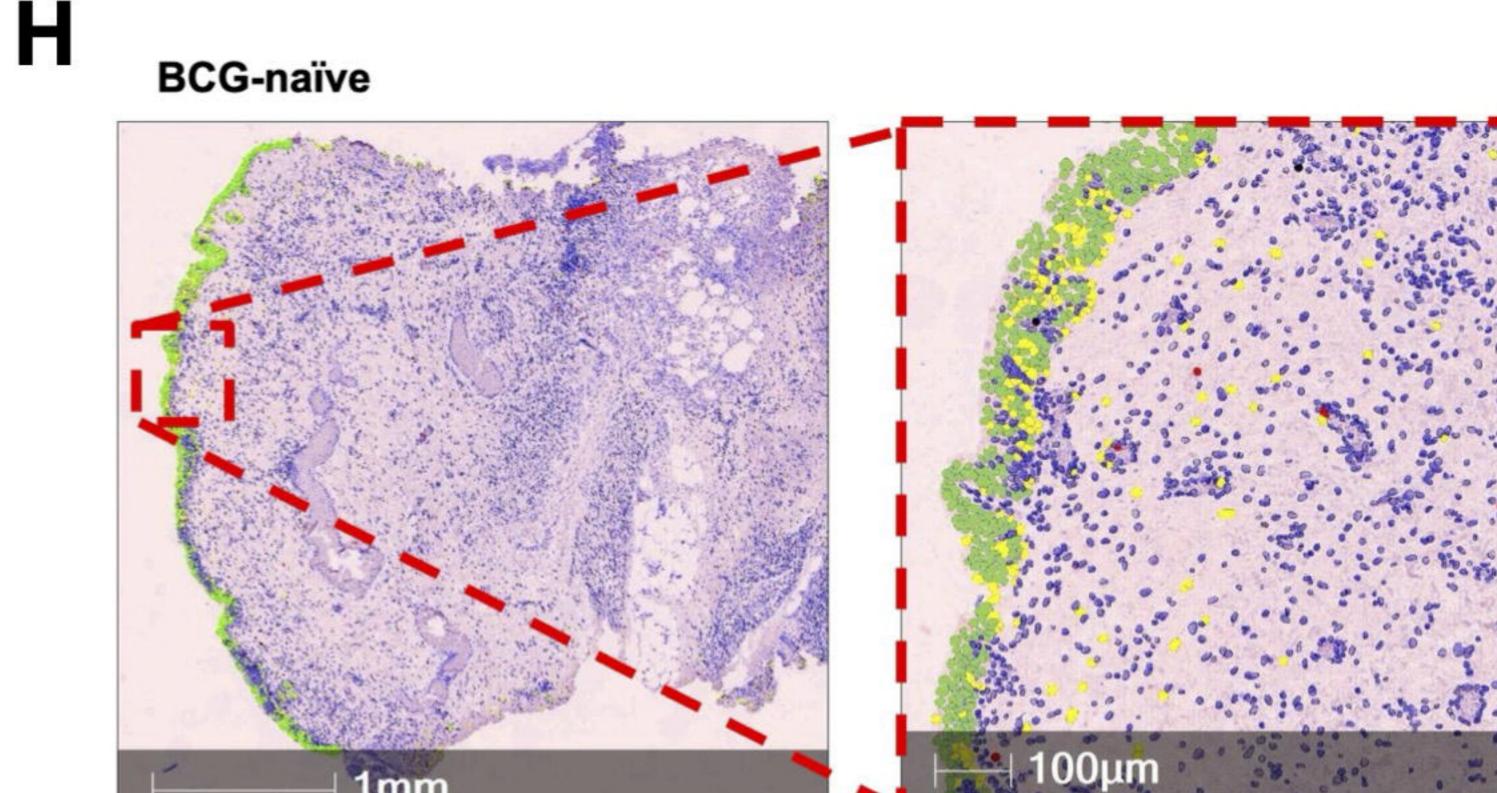




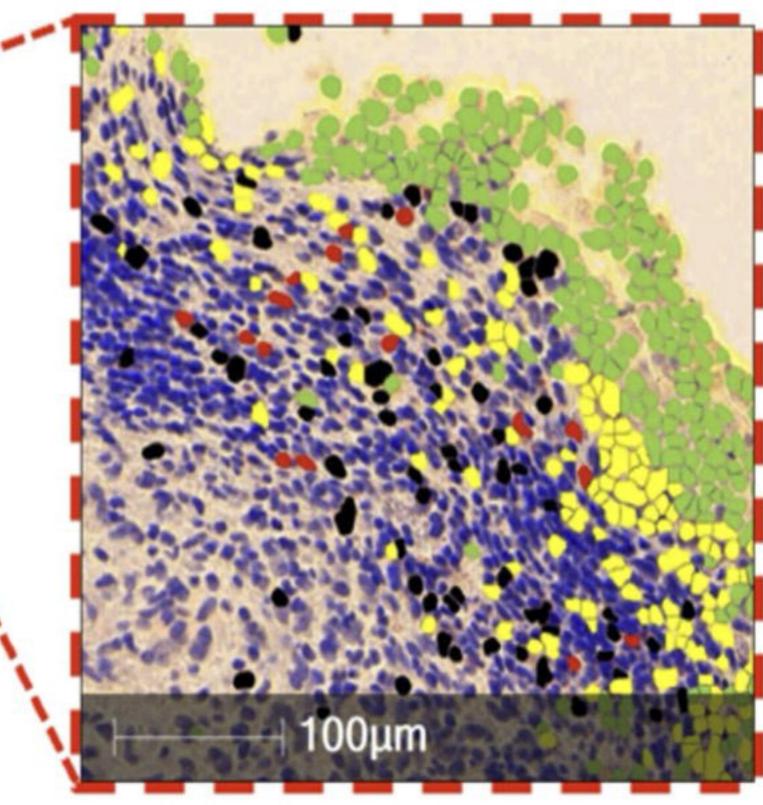
Multiplex IHC: pan-CK, HLA-E, CD3, NKG2A

D

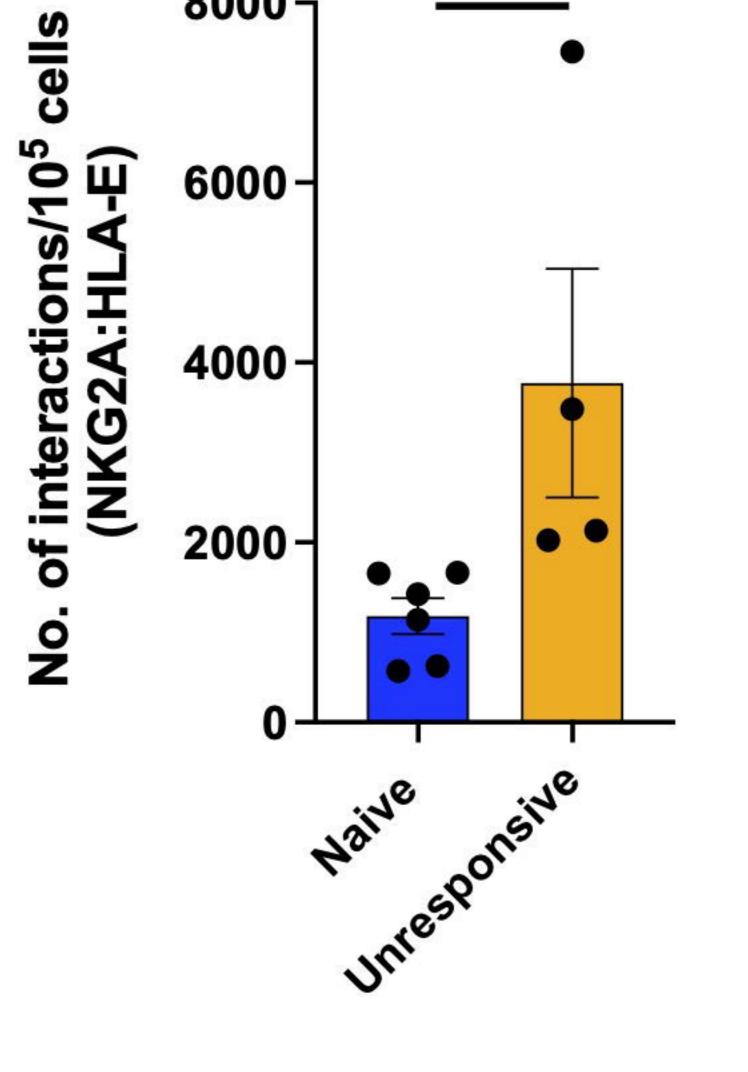




Κ

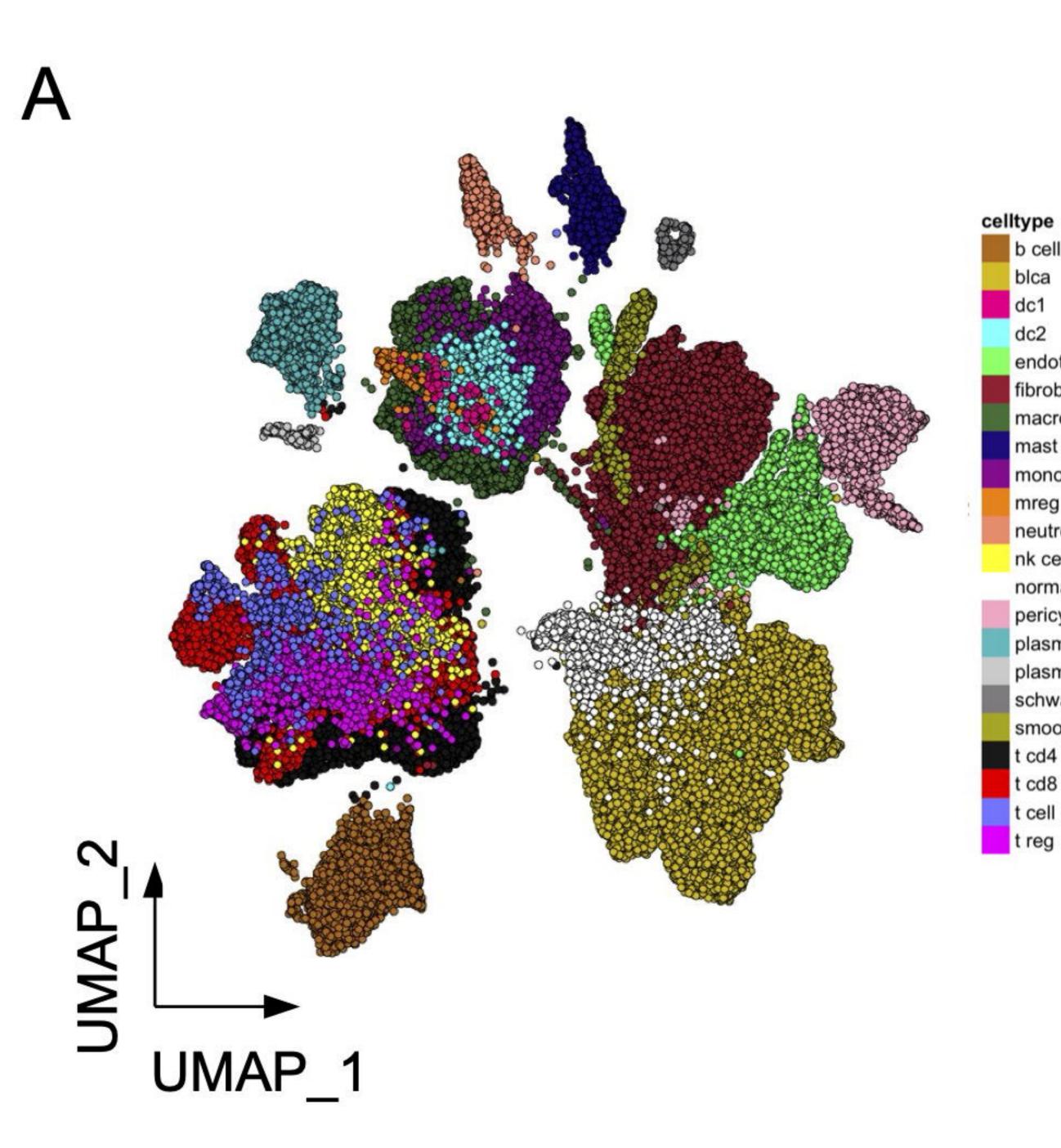


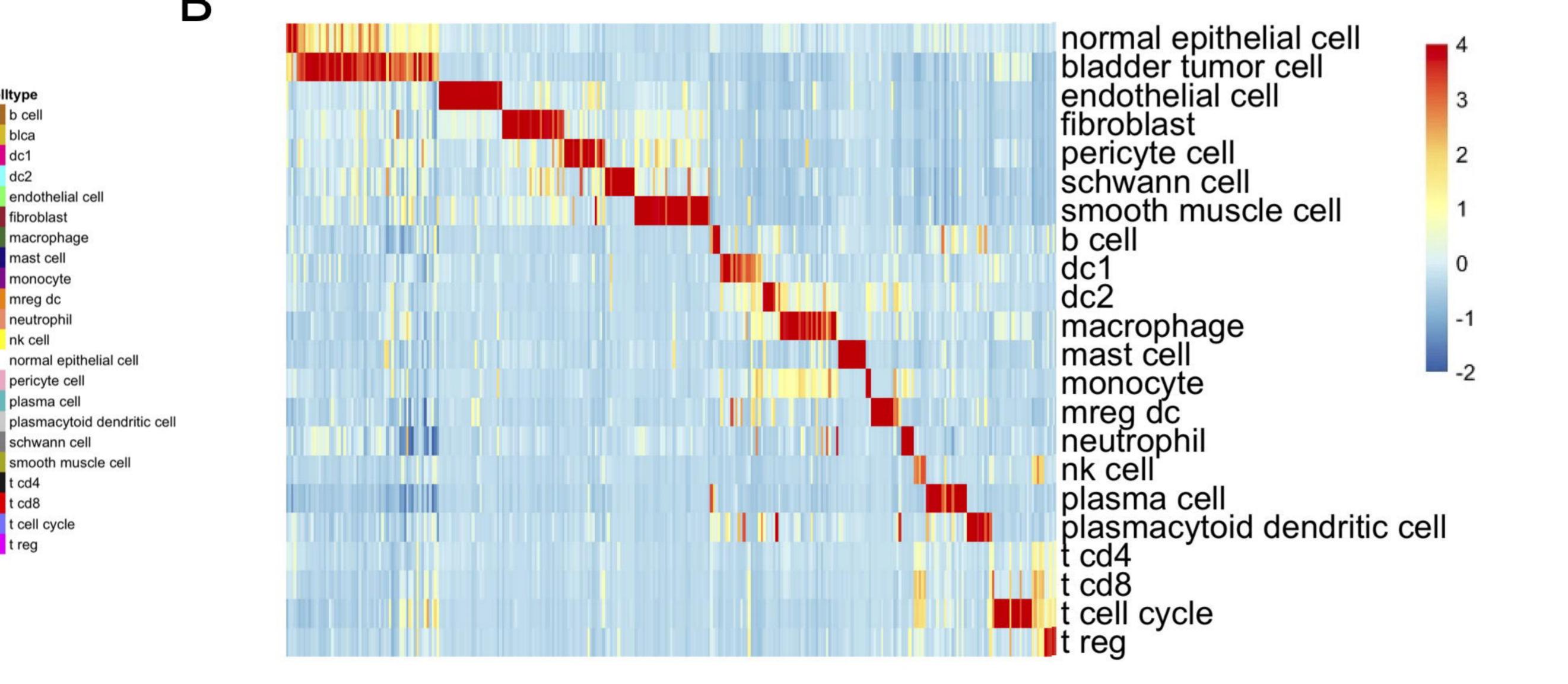
<mark>ر 8000</mark>



P=0.009

Figure 2.





B

b cell

blca

dc1

dc2

endothelial cell

macrophage

fibroblast

mast cell

monocyte

neutrophil

pericyte cell

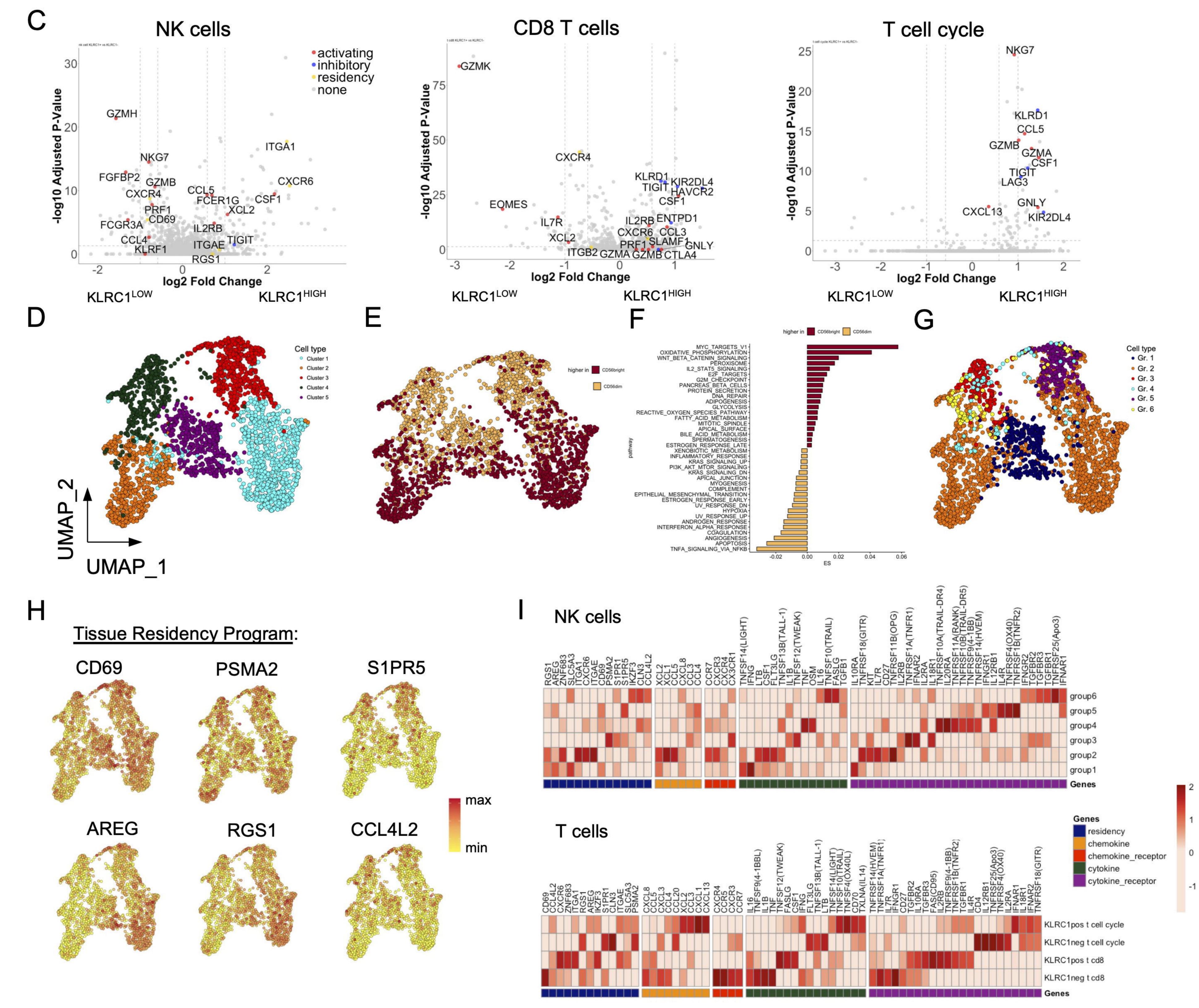
plasma cell

schwann cell

t cell cycle t reg

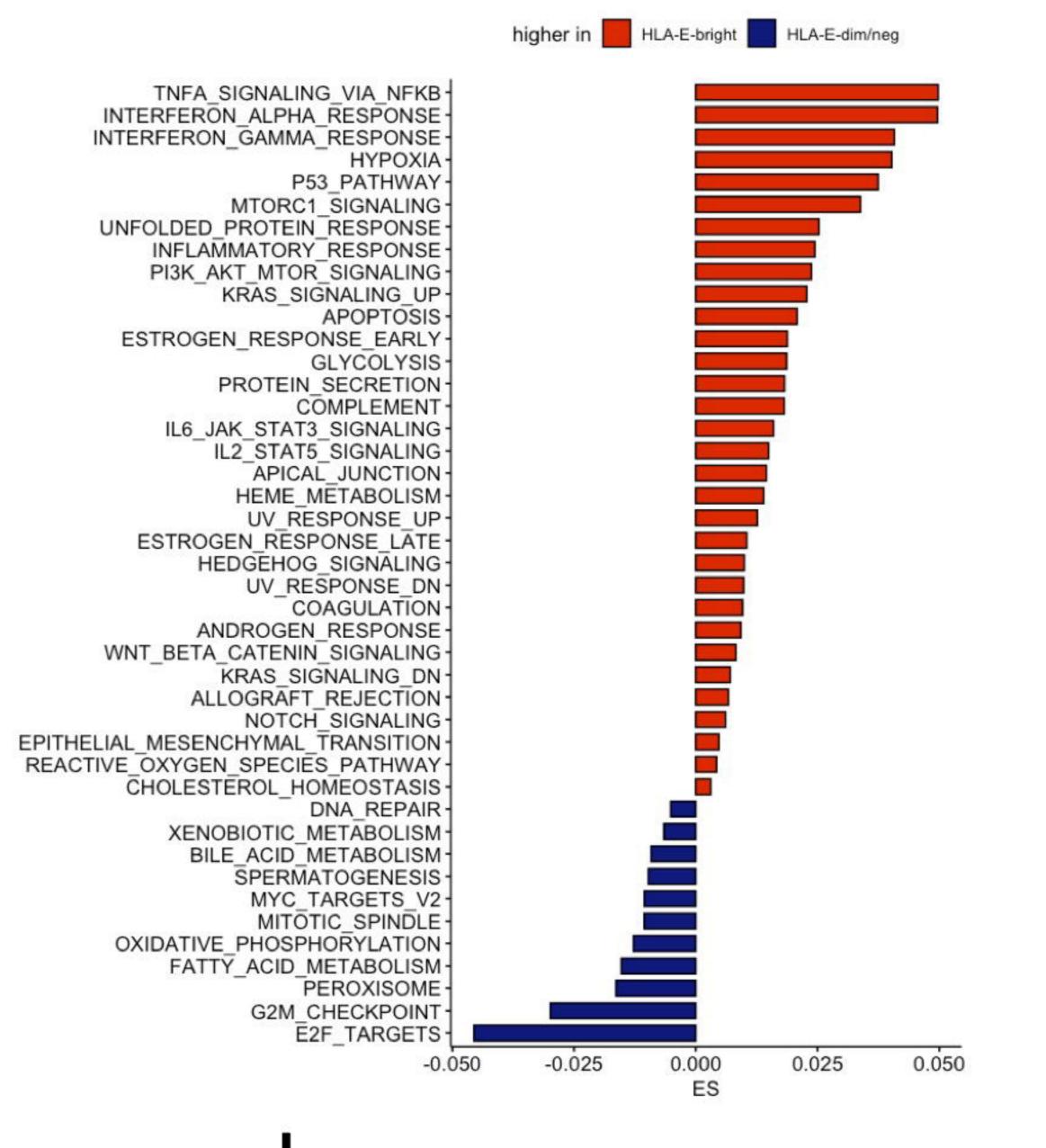
mreg dc

nk cell



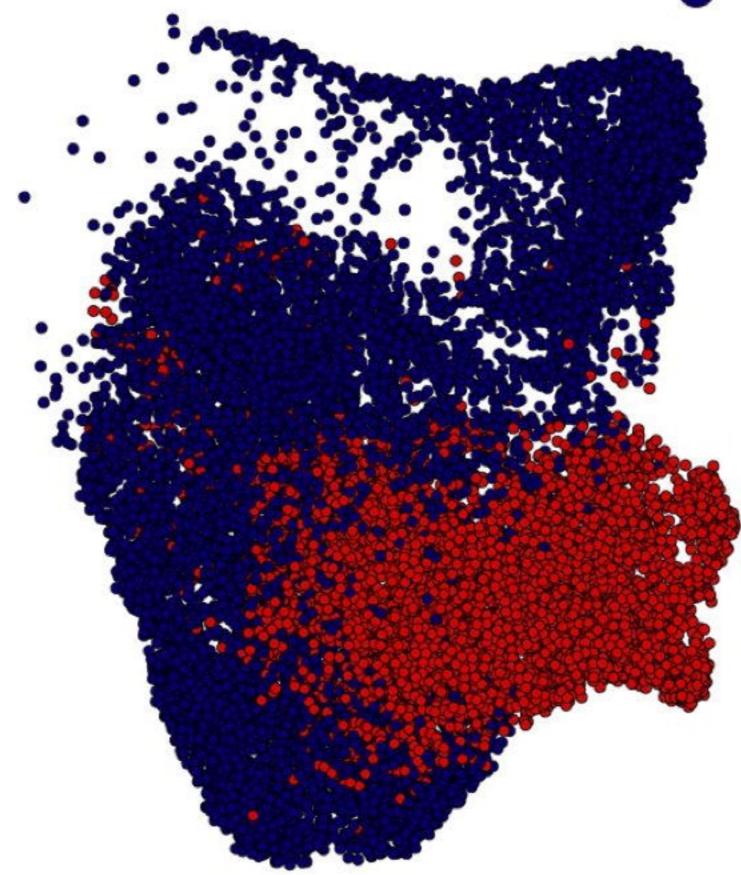
bioRxiv preprint doi: https://doi.org/10.1101/2024.09.02.610816; this version posted September 3, 2024. The copyright holder for this preprint (which was not certified by peer review) is the author/funder, who has granted bioRxiv a license to display the preprint in perpetuity. It is made available under aCC-BY-ND 4.0 International license.

Figure 3.

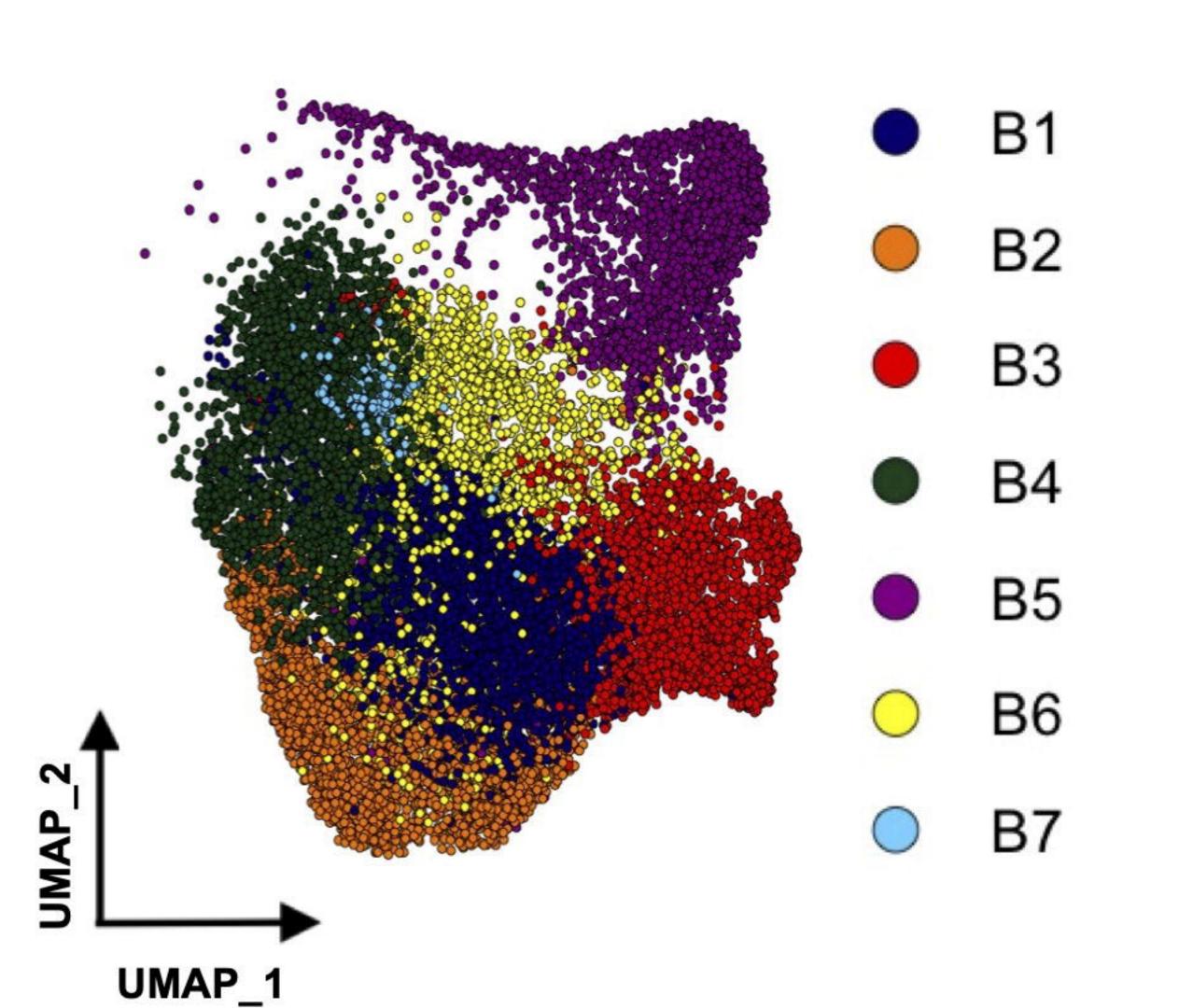


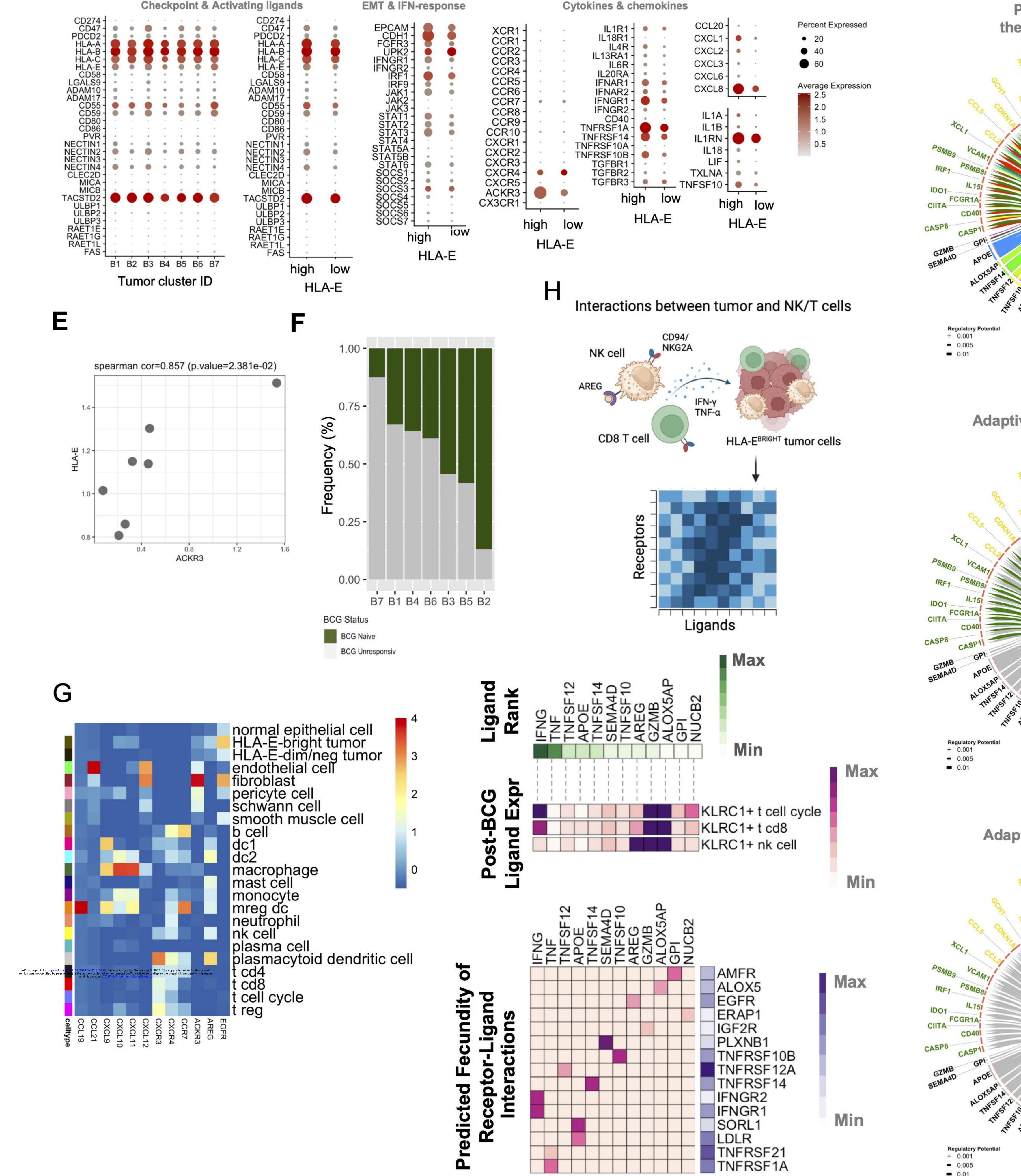
HLA-E-bright

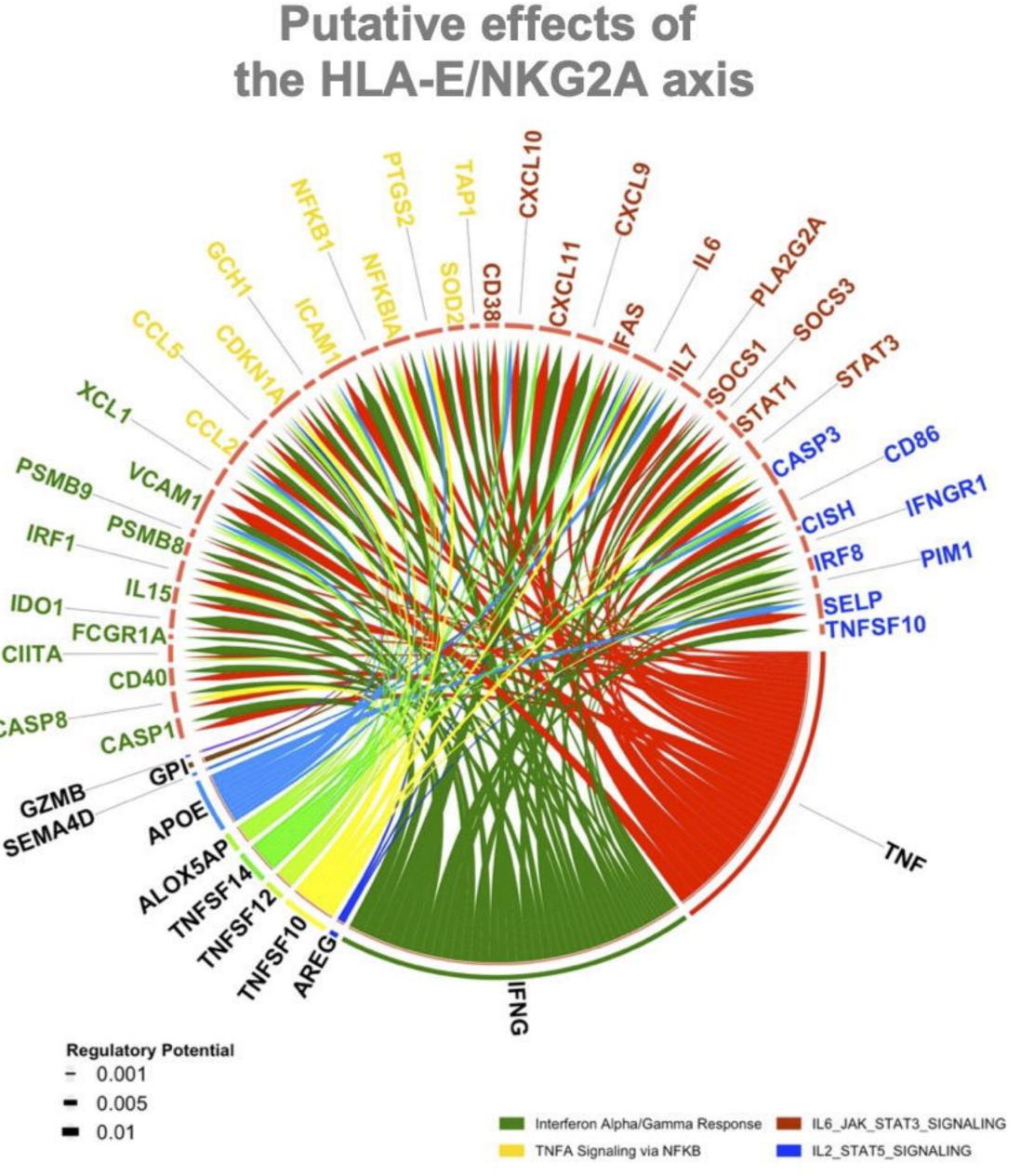
HLA-E-dim/neg



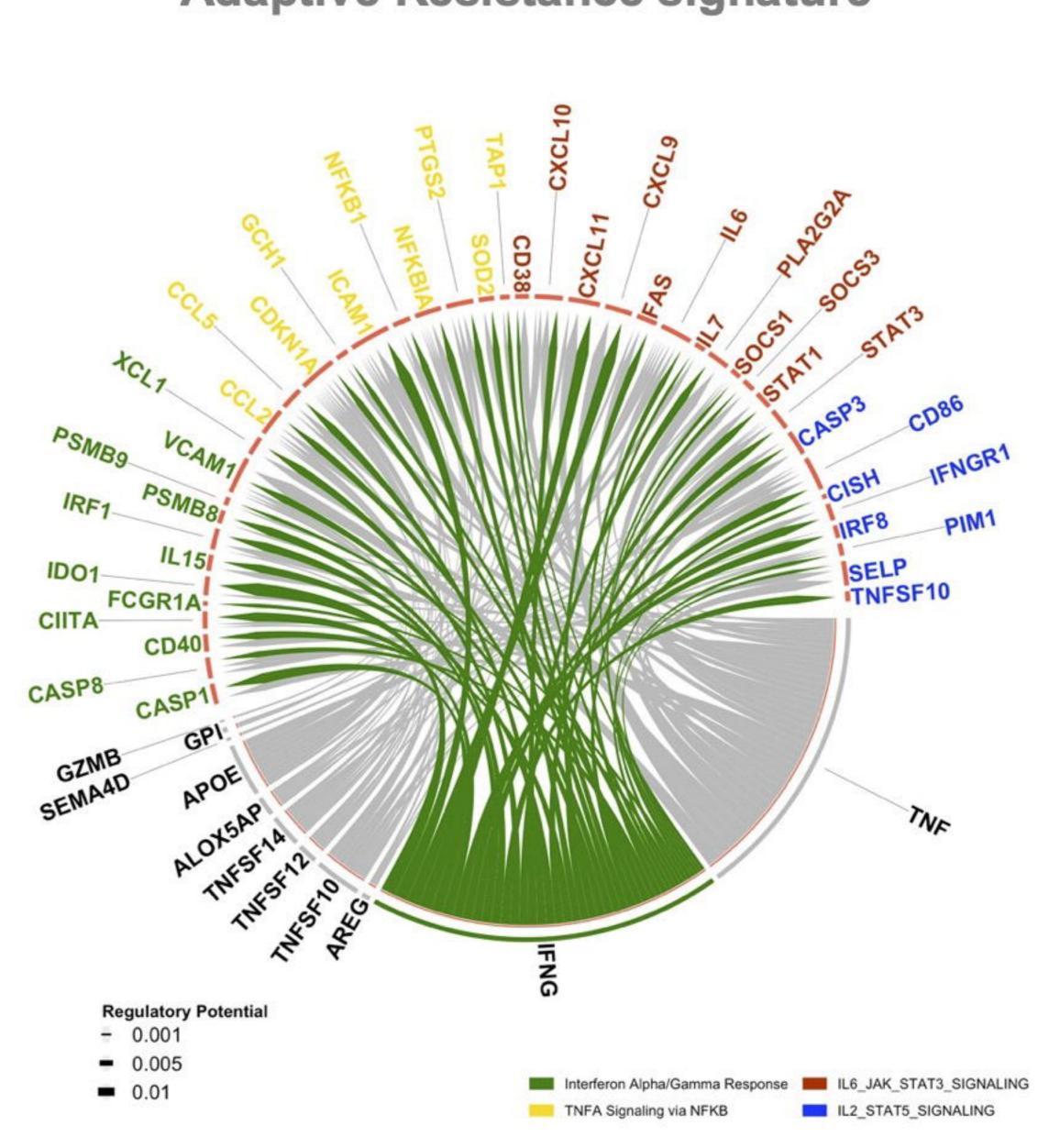
B







IFNγ-mediated Adaptive Resistance signature



AREG-mediated Adaptive Resistance signature

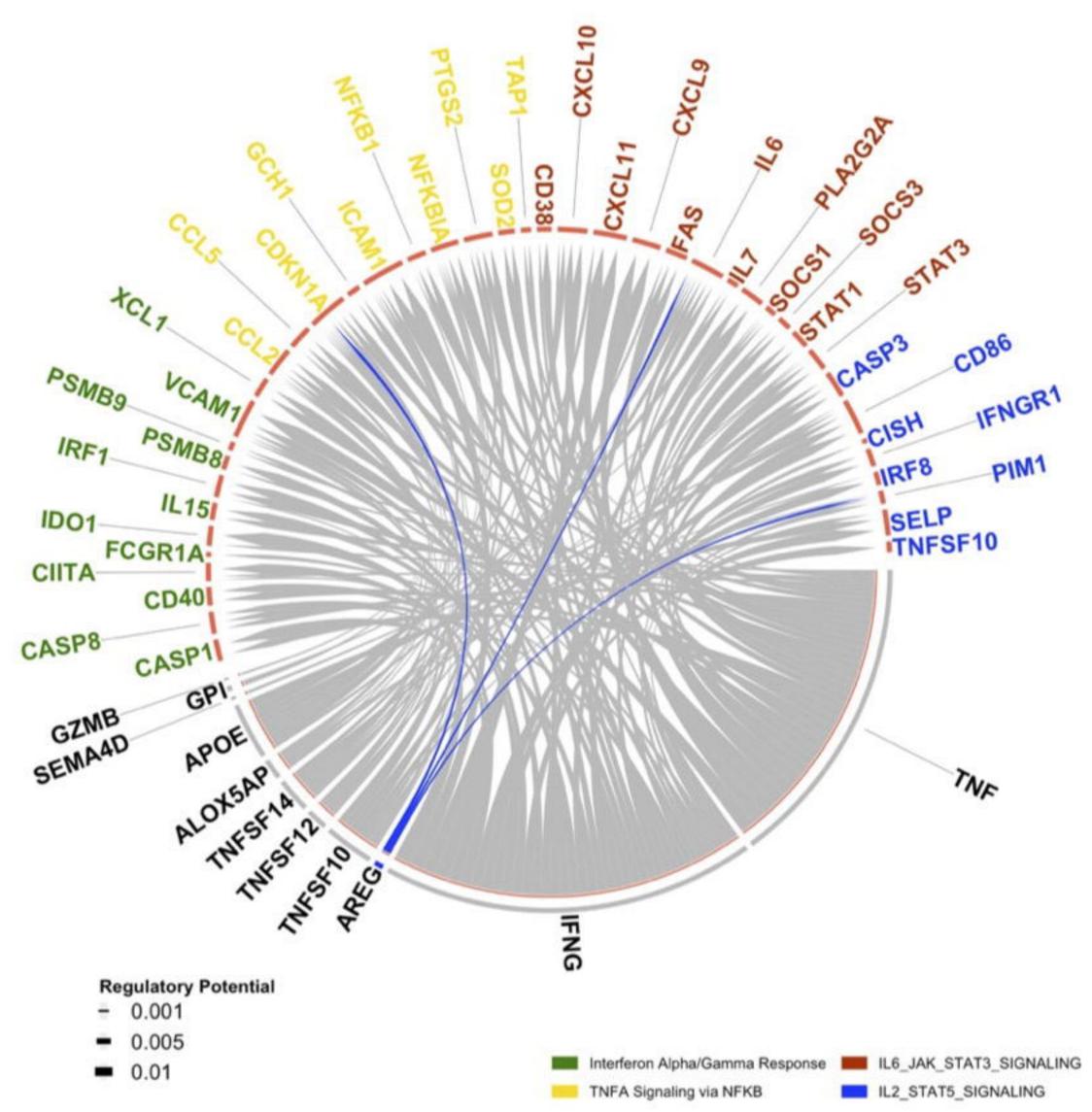
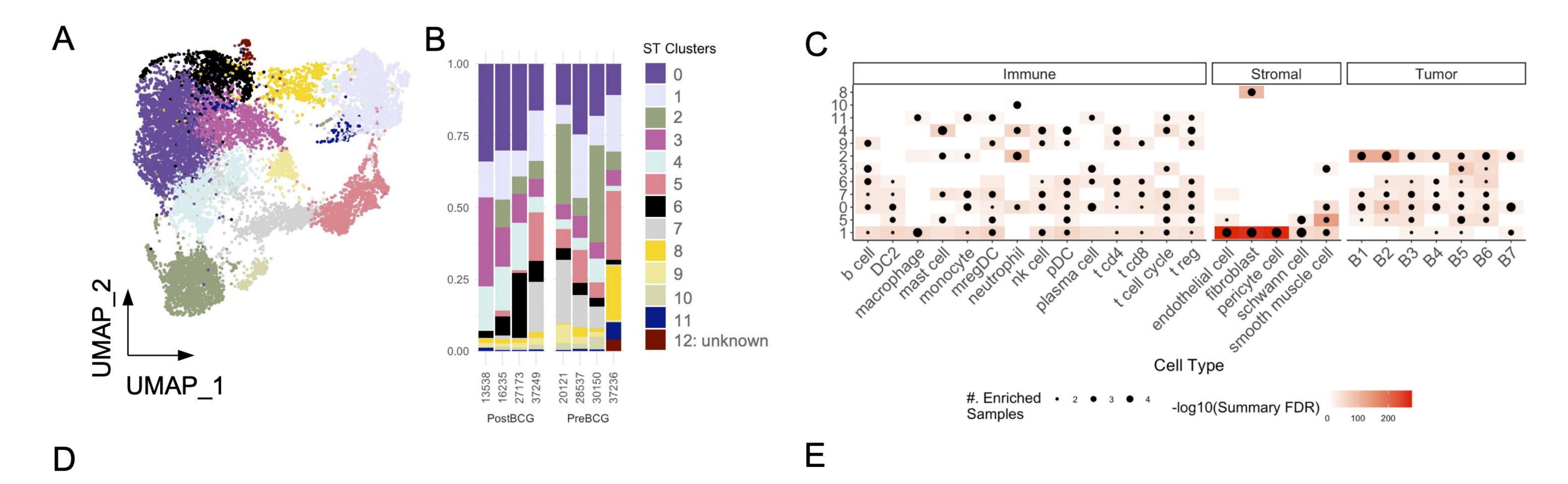
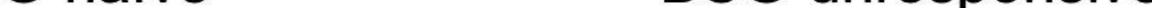


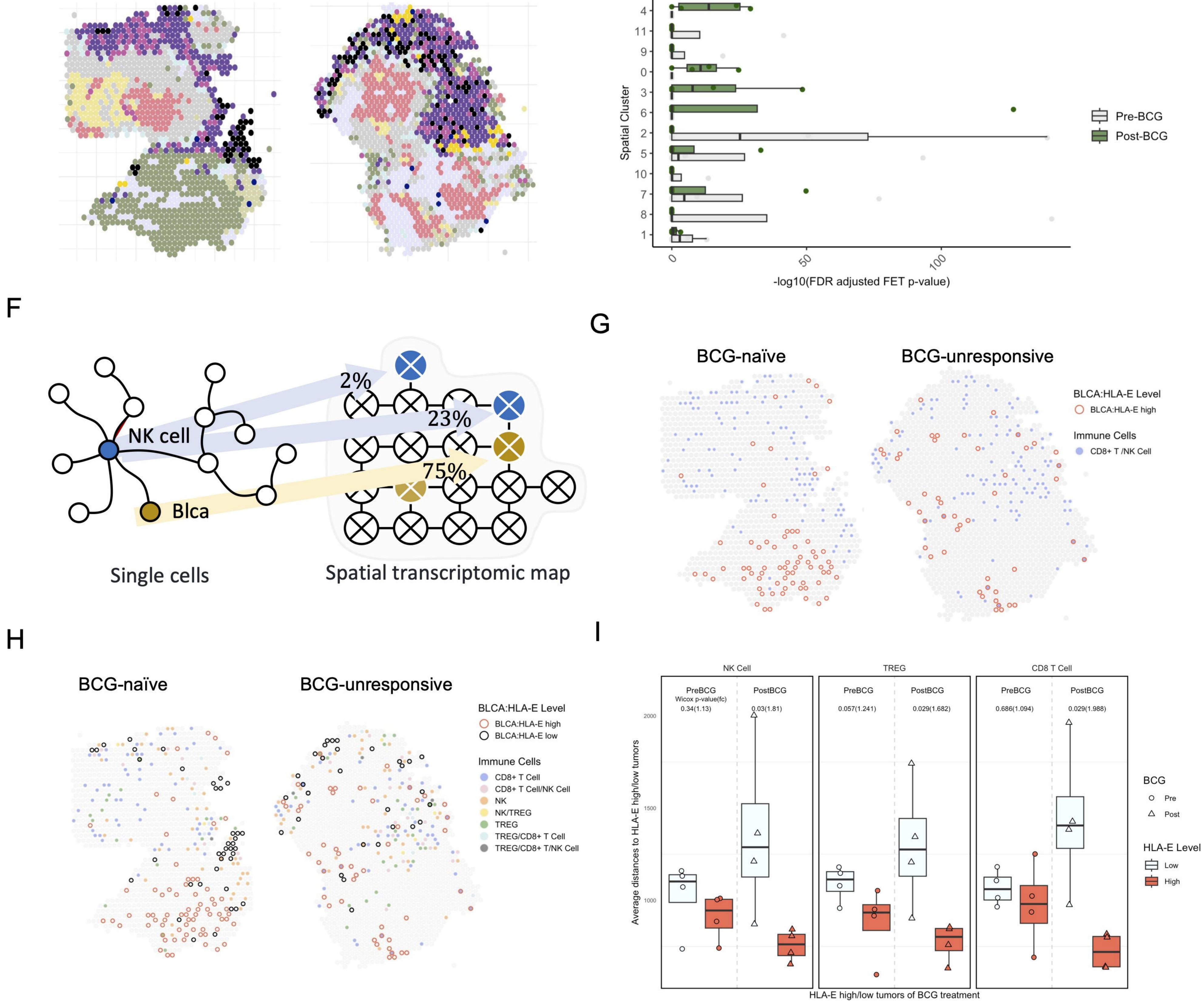
Figure 4.



BCG-naïve

BCG-unresponsive

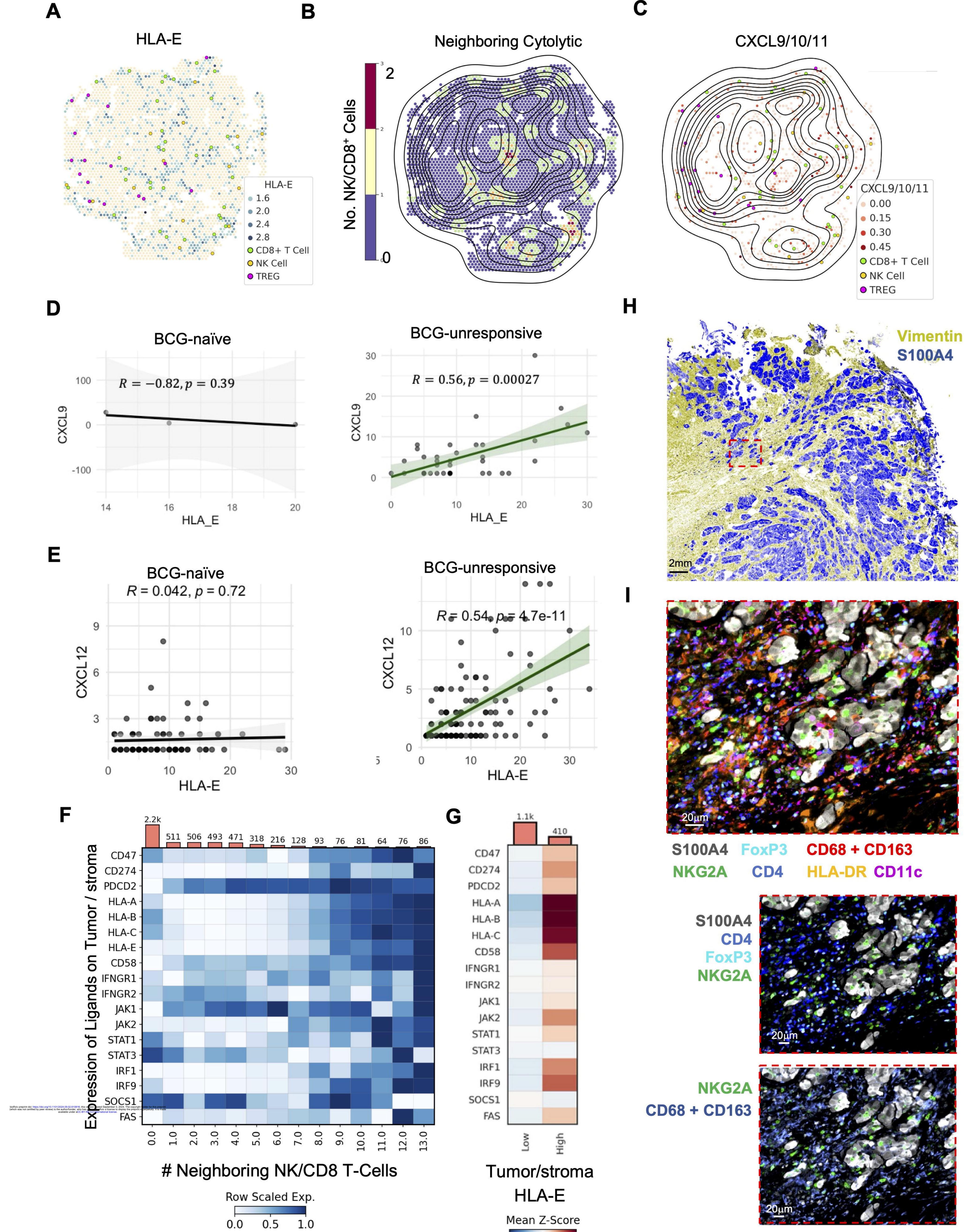


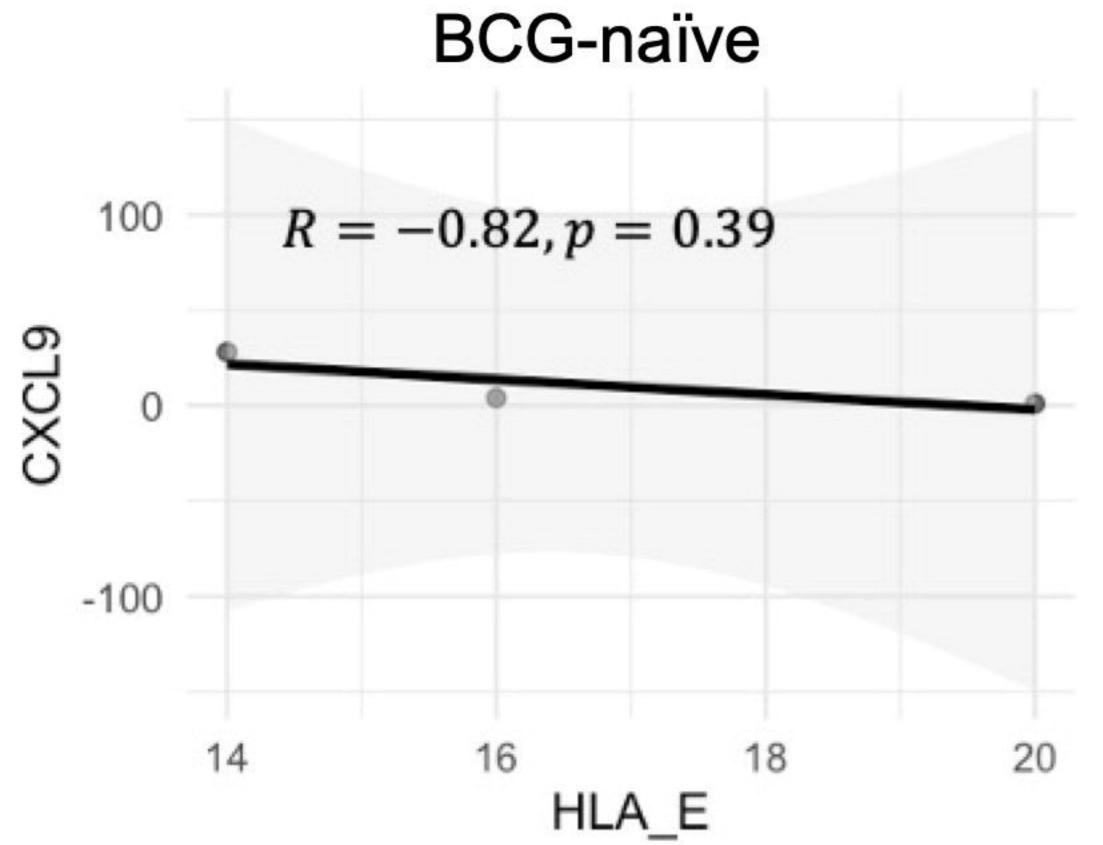


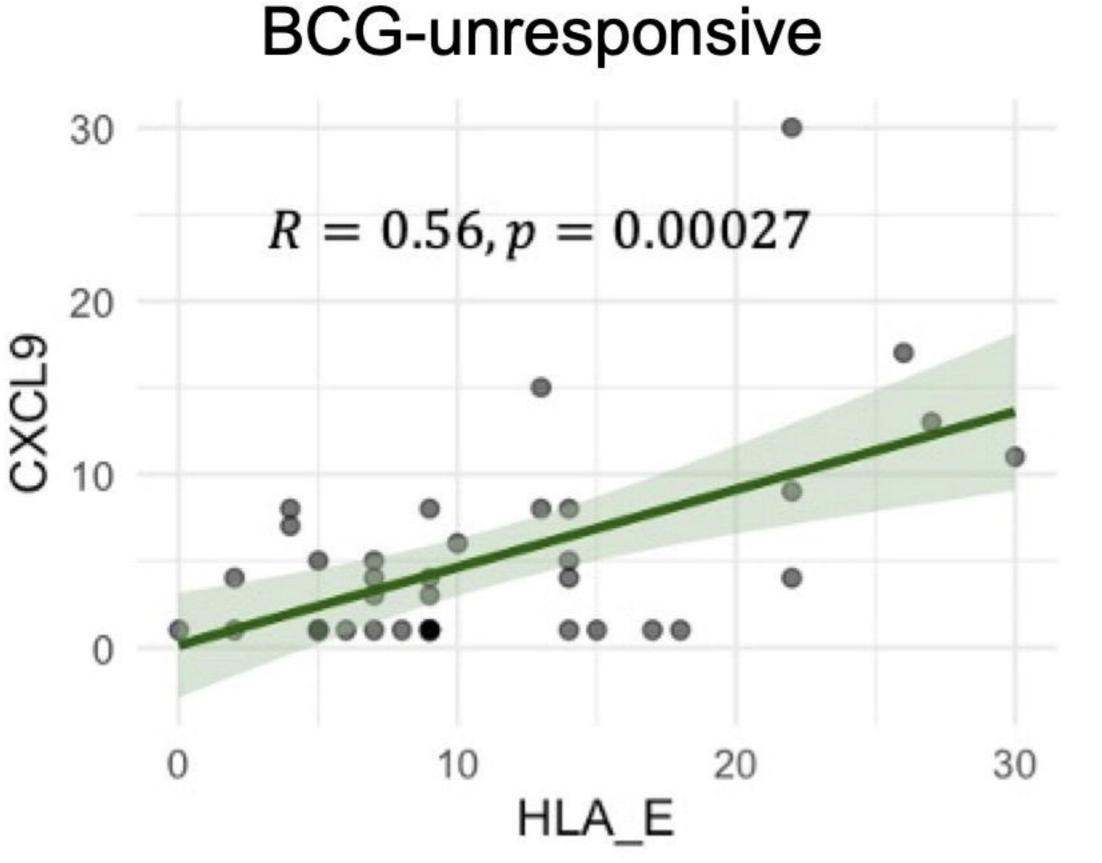


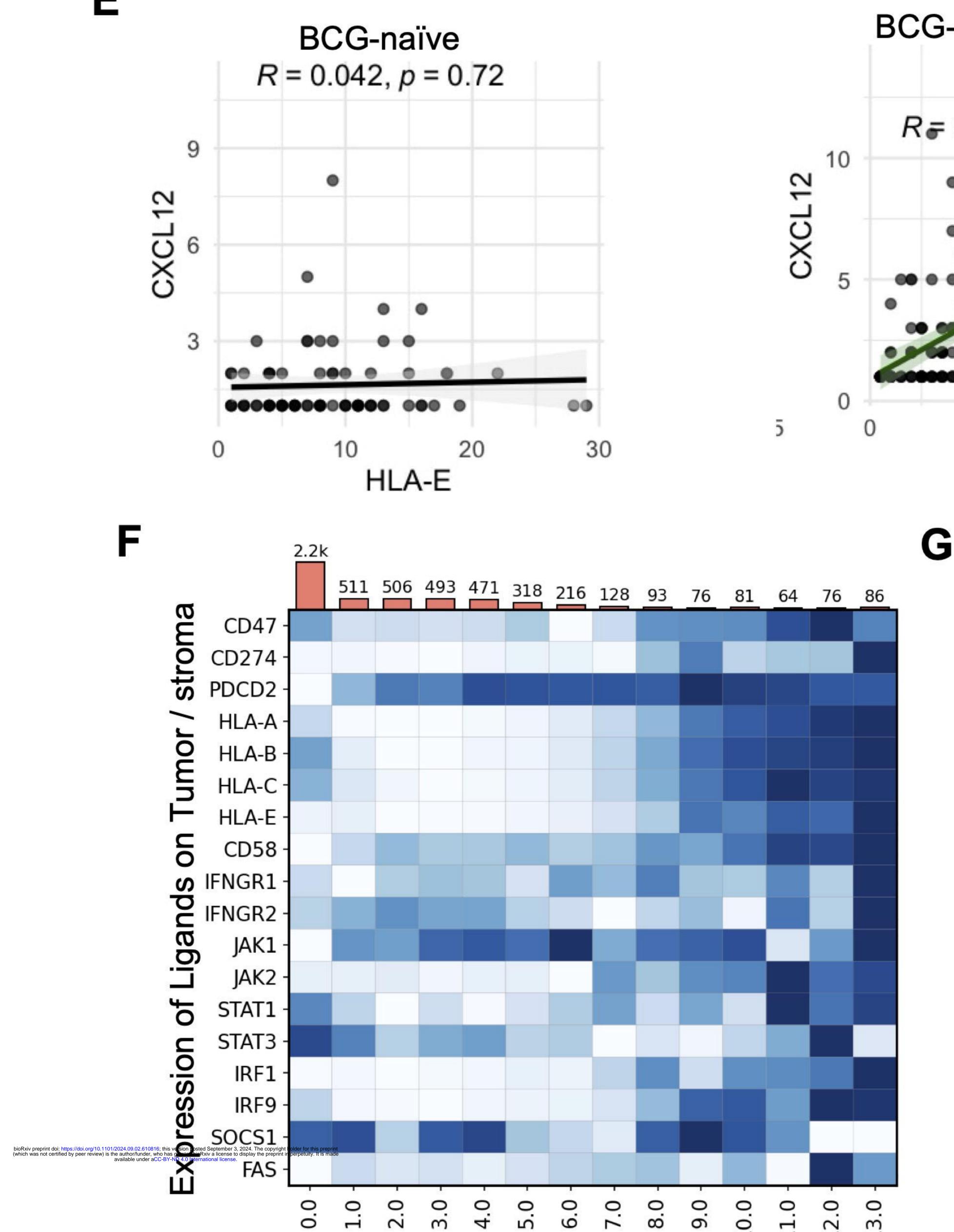
bioRxiv preprint doi: https://doi.org/10.1101/2024.09.02.610816; this version posted September 3, 2024. The copyright holder for this preprint (which was not certified by peer review) is the author/funder, who has granted bioRxiv a license to display the preprint in perpetuity. It is made available under aCC-BY-ND 4.0 International license.

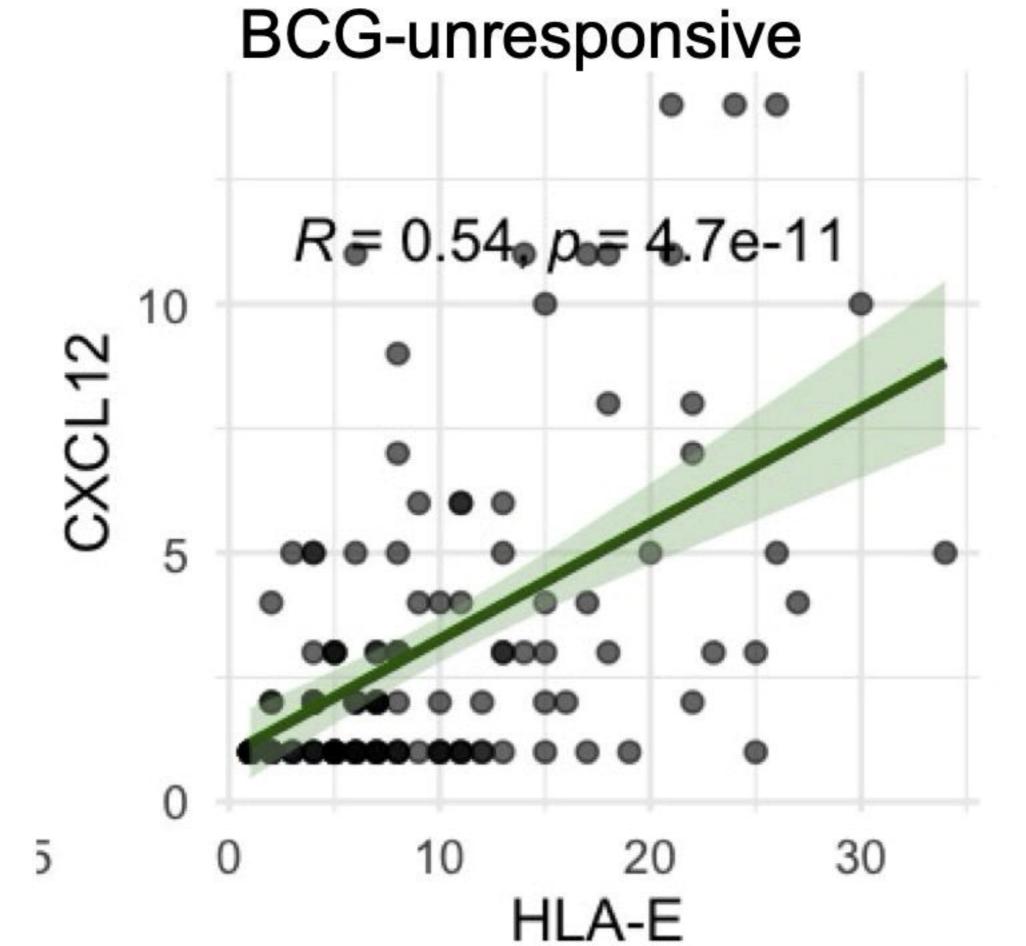
Figure 5.











 $^{-1}$

0

Figure 6.

bioRxiv preprint doi: https://doi.org/10.1101/2024.09.02.610816; this version posted September 3, 2024. The copyright holder for this preprint (which was not certified by peer review) is the author/funder, who has granted bioRxiv a license to display the preprint in perpetuity. It is made available under aCC-BY-ND 4.0 International **Protein (OLINK)** A OLINK Urine Level (NPX) 12 Pre-BCG 3rd Dose 6th Dose 1st Cysto IFN Gamma Signature **B Cell Markers** Flt3 Cytotoxic Lymphocytes IL.2RE Lymphocyte Receptors/Function CCL1 **Mount Sinai T Cell Checkpoint Modulation** CCL23 **Tumor Inflammation** CXCL Th1 Response CXCLS Lymphocyte Trafficking CXCL1 General T Cell Markers CXCL1 Receptor MCP. Stress Toxicity MCP. DNA Repair TWI P53 Pathway С **Oxidative Phosphorylation** _rAarhus₁ CCL19 Peroxisome CCL23 Hypoxia CXCL9 CXCL10 TGF Beta Sigaling CXCL11 -2 Normalized Enrichment Score BCG naïve BCG Unresponsive D Е PD-L1 HLA-E Before BCG Before BCG MFI MFI (No tumors present) 800 800 (Tumors present) MMP12 0 0 RAIL 2.00 CD45- Pt Tumo IL8 CXCL11 CXCL5 1.00 CXCL9 VEGFA VEGFR-2

BCG-Unresponsive vs BCG Responsive -log10(p-value) 1.00 -log10(p-value) 050 0.50 0.00 0.00 0.5 1.0 -2.0 -1.5 -1.0 -0.5 0 NPX values non-resp vs resp 0.0 0.5 0.0 NPX values non-resp vs resp After BCG After BCG CXCL5 (Tumors present) (No tumors present) CXCL5 CXCL1 MMP12 2.00 -log10(p-value) 0.50 TNF -log10(p-value) 001 CXCL13 CXCL11 CCL17 LAMP3 CL3 CXCL1 CAIX :4 0.00 0.00 1.2 0.0 0.5 0.0 0.4 0.8 -0.5 NPX values non-resp vs resp NPX values non-resp vs resp

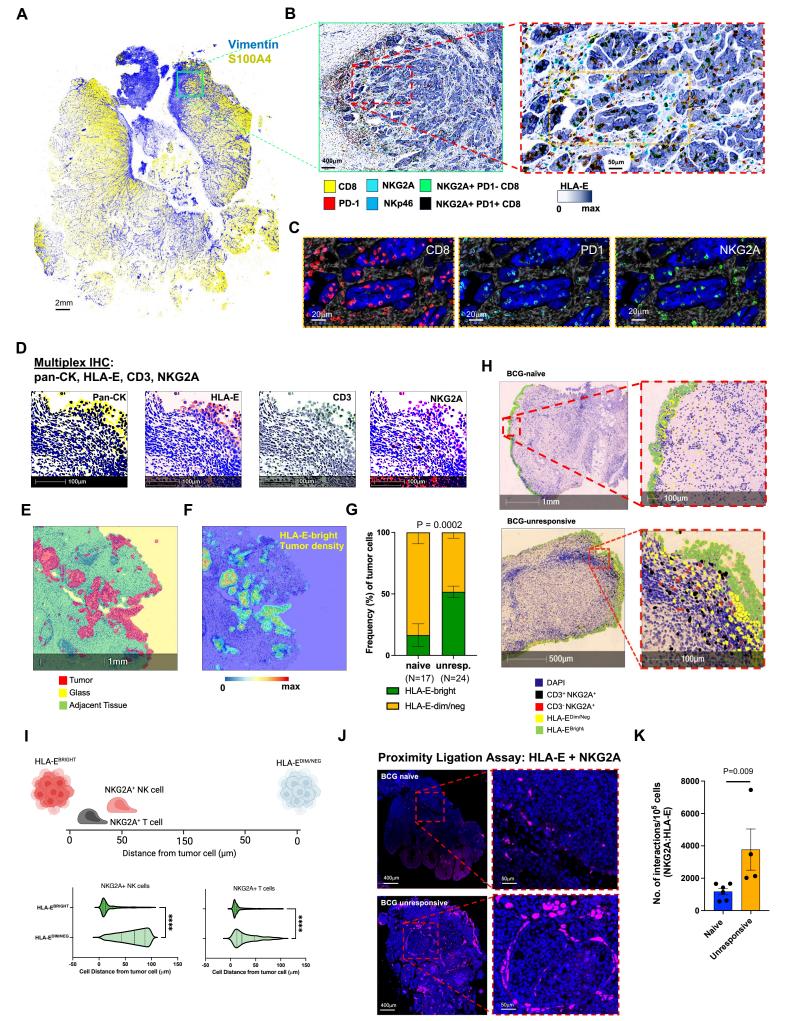
non-resp.

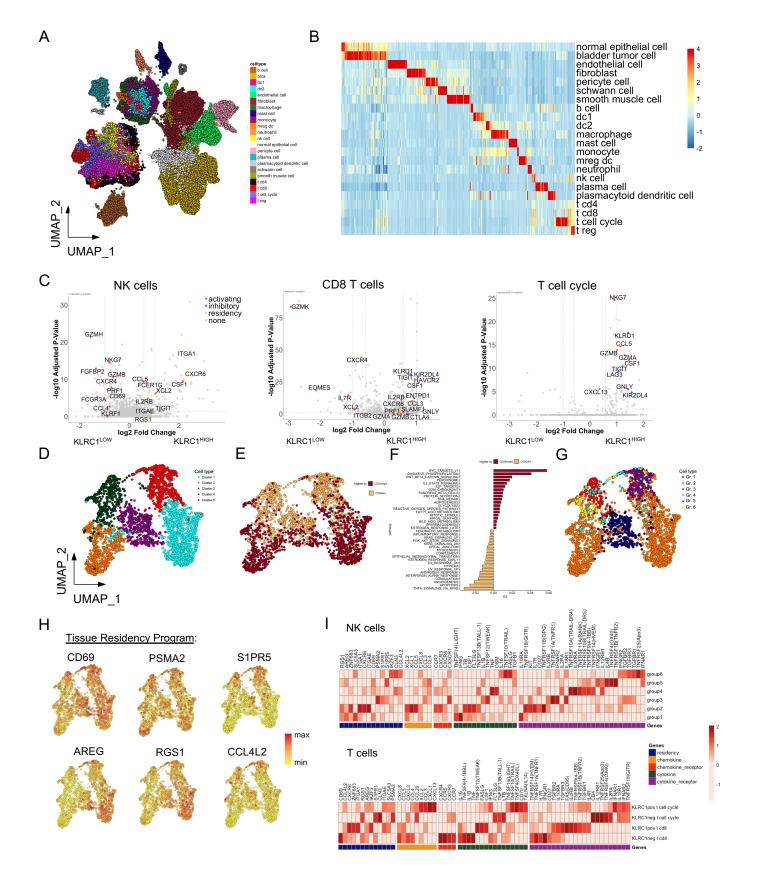
resp.

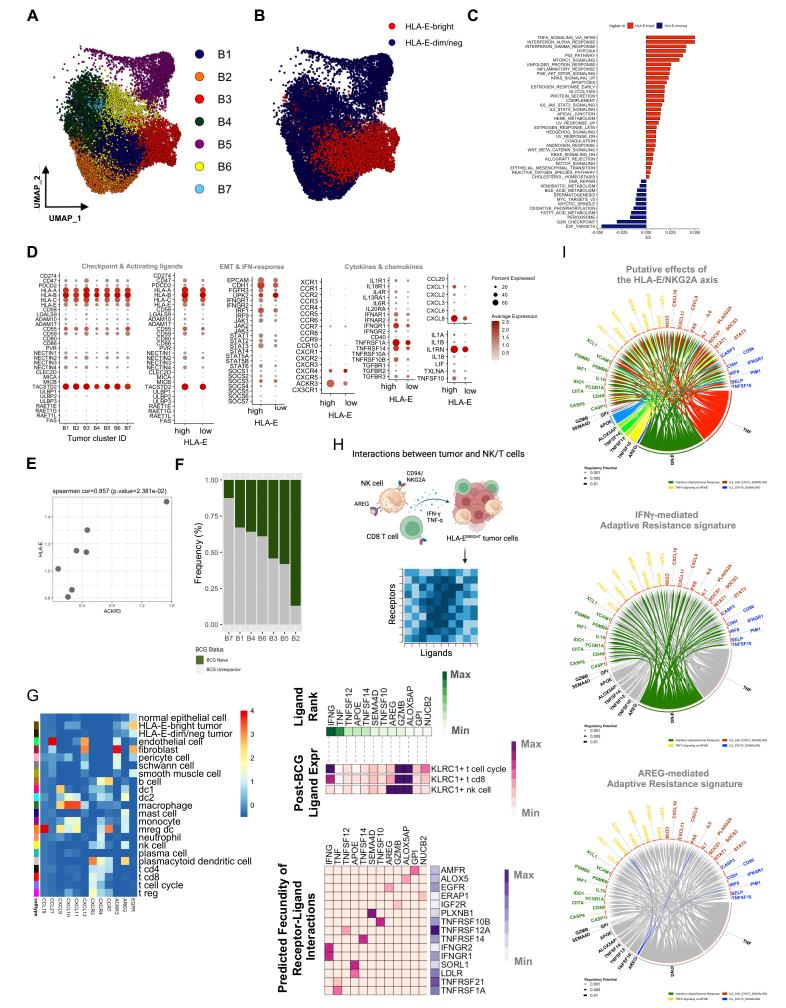
253J Laval J82 639V KU-19-19 имисз T24 5637 ŀ RT112 SW1710 P RT4 MGHU3 K562 K652/HLAE+ Ex-Vivo IFN-G Stimulation

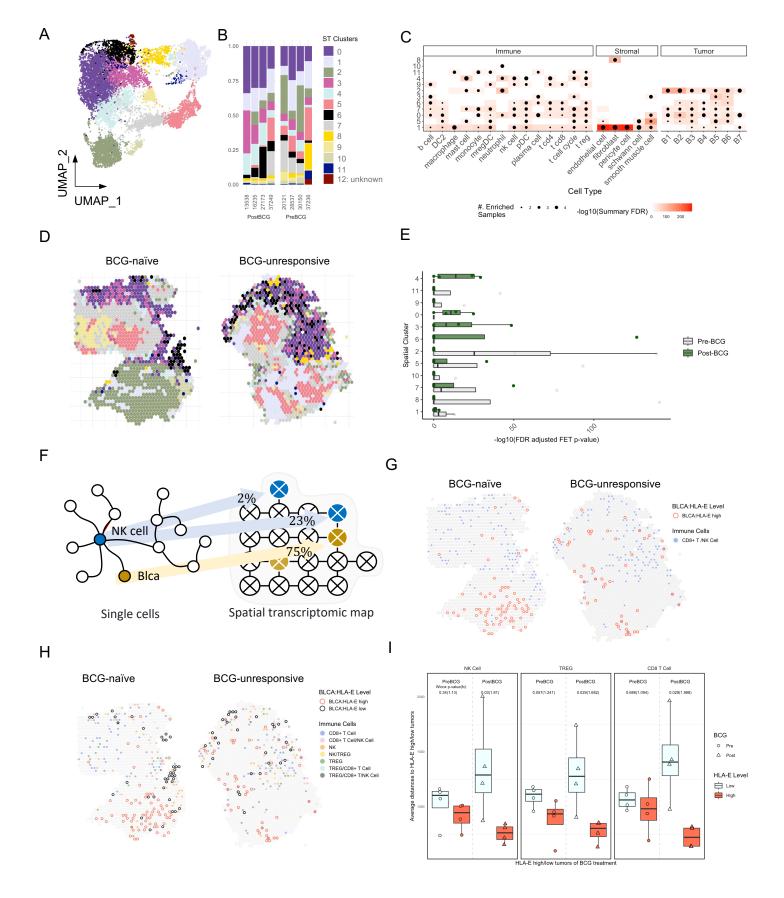
non-resp.

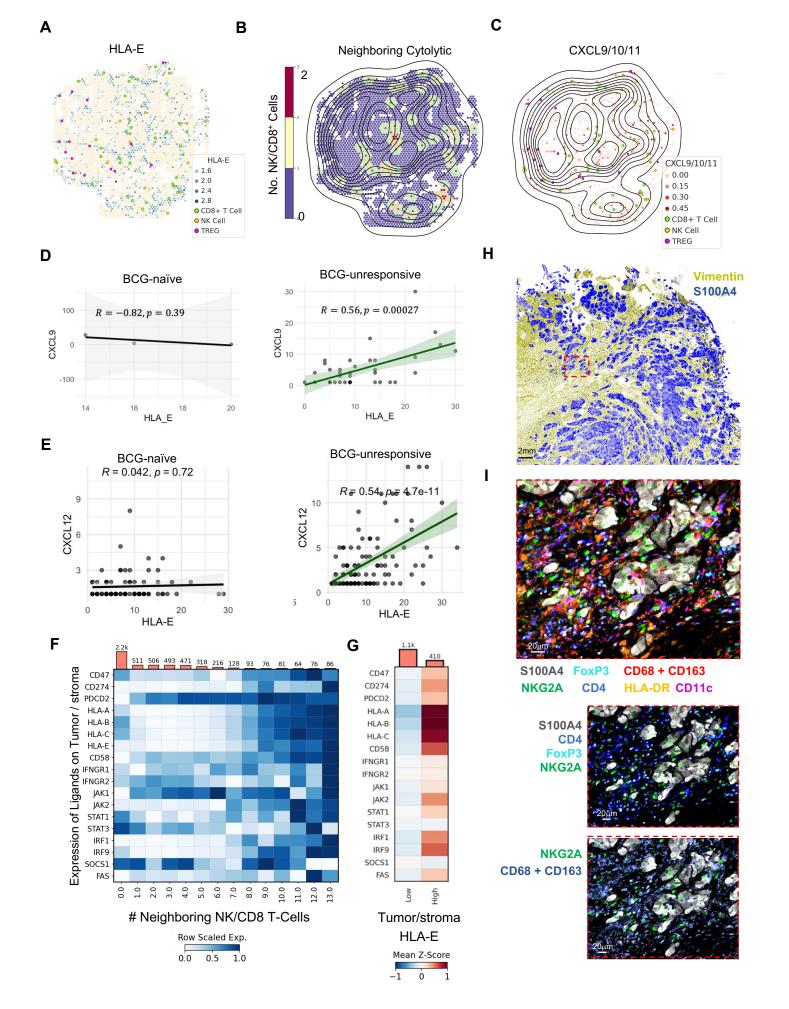
resp.

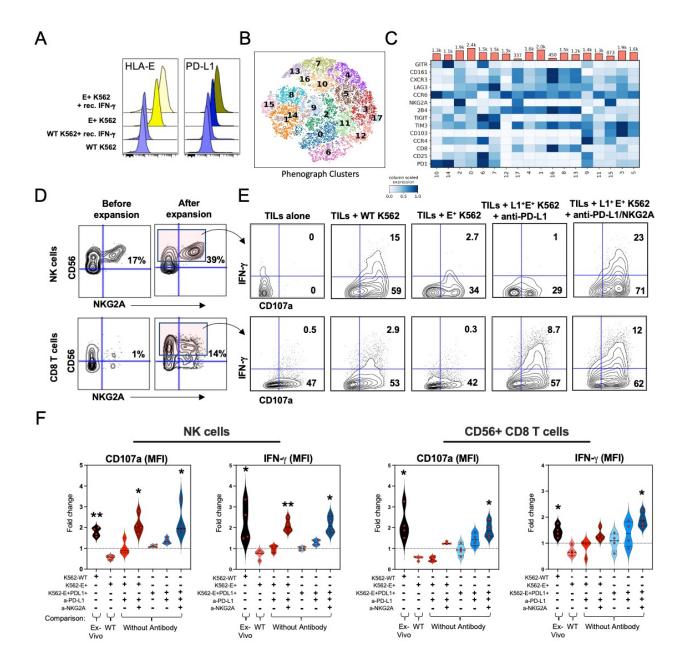












	Clinical Cohort Characteristics				
	HTG	OLINK Urine (Sinai)	Single Cell	Spatial	Cytof
n samples, patients	36, 27	42, 26	7, 6	20, 9	16, 16
Female	4	2	0	0	1
BCG Naïve	19	26	2	4	0
BCG Unresponsive	17	-	4	5	16
Median Age	64	69.5	66.9	70.6	68.5
Median Months to Recurrence	2.9	2.1	2.3	1.7	2.73
Median Months to Progression	6.7	-	14.3	23.28	4.43
Stage at Collection					
CIS	4	-	-	-	-
Tis/Ta	5	13	-	2	8
T1	10	14	4	6	5
Т2	-	-	-	-	2
ТЗ	-	-	2	-	0
Т4	-	-	_	-	1

Gene Set Names	Defining Genes
Interferon Gamma Response Signature	CCL5, CD3D, CXCL10, IL2RB, LAG3, IDO1, IL2RG, STAT1, PRF1, PDCD1, GZMA, GZMB, CD8A, CXCL9, TBX21, CD27, CD4, CD74, IFNG, CCR5, CXCL11, CXCL13, CXCR6, PTPRC
B Cell Markers	CD79A, BLNK, CD79B, CCR9, CD19, PNOC, BLK, CD22, HLA-DOB, TCL1A, CR2, SPIB, CD72, TNFRSF17, HLA-DQA1, PAX5, MS4A1, MEF2C, FCRL2
Cytotoxic CD8 T-Cells	GZMK, FLT3LG, KLRKI, KLRDI, PRF1, GZMA, CD3G, CD8B, SIGIRR, GZMB, KLRB1, CD8A, GZMH, PF4, TBX21, CD3E, NKG7, CD27, IFNG, GNLY, EOMES, GZMM, KLRF1, KLRC1, RUNX3
Cytotoxic Receptors and Function	ZNF683, SLAMF6, KLRK1, KLRD1, SLAMF7, NCR1, SH2D1B, GZMA, TYROBP, SH2D1A, GZMB, KLRB1, KIR3DL3, CLEC4C, CLEC4D, KLRC1, GZMH, NKG7, NCR3, GNLY, GZMM, KLRF1
T-Cell Checkpoint Modulation	HLA-DQA2, CD274, TNFRSF14, CD86, CARD11, CD40, AKT1, CD3D, TNFRSF9, KLRK1, LAG3, CSK, TNFRSF13C, CD276, CD80, PDCD1, CD40LG, CD3G, PDCD1LG2, PTPN6, HLA- DQB2, ADORA2A, HLA-DPB1, TNFSF4, TIGIT, HLA-DRB1, CCL19, HAVCR2, CD3E, CD27, CD5, CCL21, CD4, HLA-DQA1, VAV1, CD70, CD24, GRB2, SRC, HLA-DRA, CD28, TNFSF13B, HLA-DPA1, TNFRSF4, CTLA4, ICOS, LYN, BTLA
Tumor Inflammation	PRF1, GZMA, GZMK, CCL5, CXCL10, IFNG, CXCL9, STAT1
Th1 Polarization and Response	NFKB1, RELA, IL12B, TBX21, IL2, IFNGR1, IL12RB1, RBPJ, JAK2, TYK2, JAK1, DLL1, IFNG, STAT1, STAT4, IL12A
Lymphocyte Trafficking	CD274, FAM129C, CDH2, CXCR4, CD68, PDCD1, PDCD1LG2, PLCG2, CD40LG, HLA-DOB, MAPK11, ITGAL, CD52, HLA-DPB1, HLA-DRB1, PVR, CD4, ITGA5, HLA-DQA1, VAV1, NCAM1, HLA-C, LILRB3, CTLA4, CD83, CD86, LILRB1, HLA-DOA, LILRA3, CXCL12, ROCK2, LILRA5, ITGAX, CD8A, PLCG1, TIGIT, HLA-DMB, ITGA4, MMP9, CD28, CYBB, SELE, ICOS, CLEC4E, ICAM1, HLA-DQA2, SDC1, CEACAM3, CD96, CD80, CD22, CD84, SELL, CD209, PDPN, SIGLEC5, HLA-DRA, SIGLEC1, ITGB2, S1PR4, CD7, CD177, ITGAM, HLA-A, ITK, CD40, ITGB7, CD34, MSN, HLA-F, CD276, PTK2B, RASSF5, CD6, S1PR1, MAPK14, VCAM1, HLA-E, TREM1, HLA-DMA,
General T Cell Markers	HLA-DPA1 LCK, CD247, CD2, CD3E, CD3G, CD5, SH2D1A, TNFRSF25, TRAT1, CD96, CD6, LAMP1, CD3D, IL2RB, CD14, ZAP70
Receptor	PDCD1, HAVCR2, TNFRSF14, CD27, CD40, TLR4, KIR2DL1, ICOS, BTLA, TNFRSF9, ADORA2A, LAG3, TNFRSF4, CTLA4, TIGIT, IL2RA, TNFRSF18
Stress Toxicity	RAD17, DDIT3, TLR4, ATR, ADM, BID, CHEK2, HSP90B1, IL1B, RIPK1, CCL2, IL6, HSPA5, CD40LG, CRP, GADD45A, VEGFA, DDB2, HSP90AA1, CASP1, TNFRSF10A, PARP1, PVR, CDKN1A, TP53, TNFRSF10B, NBN, EDN1, FAS, SERPINE1, RAD51, NFAT5, ATG7, CA9, IFNG, ATG5, ATG12, XPC, CALR, GRB2, RAD9A, HMOX1, MMP9, HUS1, EPO, IL1A, CHEK1, ATM, TNF
DNA Repair (Hallmark)	TYMS, POLR1D, GTF2H1, ITPA, TAF6, TK2, SDCBP, GPX4, SMAD5, SAC3D1, UMPS, NUDT9, NME3, RPA3, NFX1, DGUOK, GTF2H3, DGCR8, DCTN4, ERCC2, TAF9, POLR2H, NME4, XPC, BOLA2_2B, DAD1, VPS37D, TMED2, NCBP2, RAE1, NUDT21, CCNO, GTF3C5, ERCC4, SUPT5H, ARL6IP1, EIF1B, ZNF707, AK3, VPS28, RAD52, TAF10, ERCC3, FEN1, SUPT4H1, PCNA, POLR2A, POLH, BCAP31, POLB, NT5C, HCLS1, SRSF6, POLR2J, REV3L, USP11, VPS37B, POLR2K, GTF2H5, ADCY6, HPRT1, TP53, PRIM1, RALA, BCAM, POLD1, CLP1, SURF1, POLD4, GMPR2, MPG, PNP, DDB1, POLR2D, RBX1, SF3A3, RFC4, ZWINT, IMPDH2, POLR2C, ADRM1, PDE6G, POLR2G, POLR1C, POLR2F, LIG1, DUT, CMPK2, SEC61A1, RFC3, GUK1, PDE4B, RAD51, GTF2F1, POLA2, STX3, TARBP2, CDA, APRT, ELL, RFC5, POM121, RPA2, POLR3C, NME1, POLR2E, AK1, NPR2, ERCC1, GSDME, TAF12, POLR21, POLA1, CETN2, POLL, ZNRD1, POLD3, RNMT, TSG101, ELOA, DDB2, UPF3B, SNAPC5, CANT1, ADA, POLR3GL, TAF13, COX17, ERCC8, AAAS, BRF2, POLE4, SSRP1, TAF1C, RFC2, SNAPC4, EDF1, ERCC5, CSTF3, GTF2B, GTF2A2, NELFCD, MRPL40, RRM2B
P53 Pathway (Hallmark)	LRMP, IRAKI, DDIT3, AKI, BAKI, ACVRIB, RGS16, ITGB4, IFI30, HBEGF, SDC1, APAF1, MXD1, SOCS1, TXNIP, VWA5A, TRAFD1, BTG2, RAD51C, CEBPA, SPHK1, DGKA, HRAS, BAX, DDB2, GADD45A, CD82, TGFB1, RRAD, ELP1, FBXW7, CYFIP2, TCHH, PTPRE, ADA, PCNA, CDH13, CD81, CASP1, POLH, AEN, SLC3A2, SEC61A1, CDKN1A, LIF, TP53, PHLDA3, FAS, NINJ1, DEF6, FOS, TSPYL2, XPC, PROCR, HDAC3, RAD9A, HMOX1, ERCC5, CCND2, POM121, FOXO3, ILIA, CCND3, TNFSF9, TRAF4, TAP1, APP, HIST1H1C, PPP1R15A, NOTCH1, BTG1
Oxidative Phosphorylation	VDAC1, ALAS1, HSD17B10, SDHA, ALDH6A1, ATP5F1, PHB2, BAX, TCIRG1, GPX4,
(Hallmark) Peroxisome (Hallmark)	CASP7, NDUFA5, POLR2F, COX17, HTRA2, SURF1, OAT, SLC25A3, DLAT, GPI HSD11B2, ABCD2, ABCB1, ERCC1, ERCC3, HRAS, CDK7, CADM1, FDPS, BCL10, ACSL1, MSH2
Нурохіа	NFKB1, VDAC1, ADORA2B, ATR, NAMPT, ADM, TXNIP, MAP3K1, F3, VEGFA, EGR1, RBPJ, MIF, IGFBP3, NCOA1, HIF1A, PLAU, TP53, EDN1, SERPINE1, FOS, CA9, PER1, NOS3, MMP9, HMOX1, LGALS3, MET, EPO, APEX1, BLM, GPI, PIM1
TGF Beta Signaling	CBL, CREBBP, LTBP1, ID1, TGFB1, SMAD5, MYC, PARP1, TGFBR3, EP300, IFNG, TGFBR1, SMAD2, TGFBR2, THBS1, SMAD3, TGFB3, MAPK3, TNF

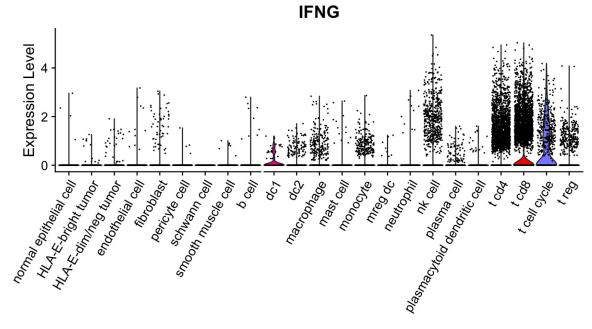
Extended data Table S1: Genes defining gene-set enrichment pathways

Channel	Merker	Clana		
Channel		Clone NA		
1	DAPI	NA T200/797		
2	CD45RO			
3	HLA-A	EP1395Y		
4	CD4	EPR6855		
5	Podoplanin	18H5		
6	CD20	SP32		
7	CD68	RM1031		
8	CD8	EPR26538-16		
9	SMA	EPR5368		
10	CD11c	FK24		
11	HLA-E	MEM-E/02		
12	CD31	WM59		
13	HLA-DR	EPR6148		
14	Granzyme B	EPR20129-217		
15	Vimentin	LN-6		
16	CD3e	EPR5361(2)		
17	CD56	EP2567Y		
18	CD34	4H11		
19	PD-L1	28-8		
20	ICOS	HK53		
21	CD57	HNK1		
22	FOXP3	2A11G9		
23	NKG2D	polyclonal		
24	Pan-Cytokeratin			
25	CD163	RM1114		
26	PAX-5	EPR3730(2)		
27	ASCT2	CAL33		
28	PD-1	CAL20		
29	CD21	EP3093		
30	GLUT1	EPR3915		
31	CD11b	M1/70		
32	Ki67	EPR3610		
33	S100A4	1F12-1G7		
34	Collagen IV	HL1351		
35	CD14	1H5D8		
36	LC3B	EPR21234		
37	CD45	EPR27167-58		
38	IFNG	IFNG/466		
39	CD79a	EP3618		
40	IDO1	EPR20374		
41	CD44	IM7.8.1		
42	NKG2A	ab96319		
43	GATA3	EPR16651		
44	CD66b	polyclonal		
45	CD138	polyclonal		
46	HIF1A	EPR16897		
47	MPO	EPR20257		
48	DNAM-1	EPR23641-137		
49	NKp46	Innate Pharma		
50	CXCR3	ab71864		
51	CD38	EPR22691-219		
52	CD16	EPR22409-124		
53	ATPA5	polyclonal		
54	CTST	polyclonal		
55	LDHA	EP1563Y		
56	HK1	EPR10134(B)		
57	MMP9	EP1254		
58	PHHH3	polyclonal		
59	BAX	ab53154		

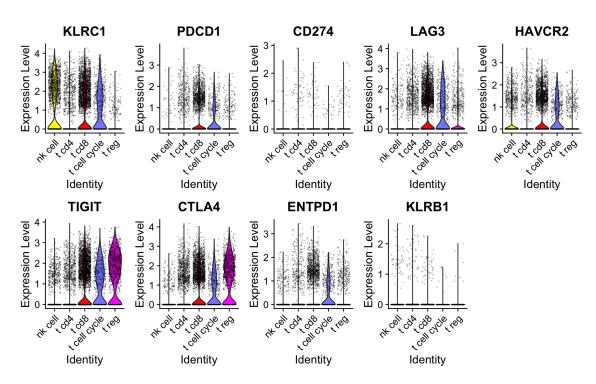
cell cluster	
	C19orf33, SNCG, MIR205HG, KRT19, KRT17, FXYD3, SYT8, SMIM22, ELF3, KRT18, CLDN4 KRT8, CD24, KRT18, TACSTD2, MGST1, FXYD3, ELF3, CLDN4, SMIM22, KLF5, KRT7, KRT19, DHRS2, S100P, GDF15, PSCA, AGR2, SERINC2, S100A14, SDC1, GATA3, KRT20, CLDN7, FOXQ1, CYBSA, AKR1C3, C19orf33, TMEM54, MDK, RARRES1, RAB25, NQO1, TMEM97, SDC4, VSIG2, RALBP1, EFNA1, CDH1, EHF, JUP, CAPS, IDH1, SPTSSB, HEBP2, SPIN72, CAMK2N1, AL158206.1, MGST2, TSTD1, MAL2, S100A13, ADIRF, HES1, PTPRF, ERBB2, TBX3, PHLDA2, RAB11FIP1, SFN, ID1, ATP1B1, GNL3, CYP4B1, TXNDC17, MARCKSL1, LSR, NR2F6, ABHD11, PLPP2, TNFRSF21, S100A16, SLPI, TSPAN13, TNFAIP2, SPIN1, NEDD4L, STAP2, KRTCAP3, CD9, BEX3, AKR1C2, EPCAM, RAB11A, PPARG, FOXA1, CTTN, GIPC1,
	ALAS1, AHR, SH3YL1, EMP2, TCEAL4, GGCT, PAFAH1B3, FBP1, NDUFS6, IGFBP3, SNHG18, GPRC5A, AP1S1, CISD3, ECHS1, TIMM13, RBM47, UQCC2, POLR2I, TSPAN6, OCIAD2, GRHL3, ARPC1A, KRT10, CENPX, CRABP2, MRPL14, DCXR, PRDX2
endothelial cell	PCAT19, SPARCL1, RAMP2, VWF, EGFL7, ECSCR, PLVAP, AQP1, TM4SF1, CLDN5, ADGRL4, CLEC14A, CAV1, CRIP2, IGFBP7, EPAS1, RAMP3, EMP1, IFI27, KLF2, SPRY1, EMCN, A2M, ENG, NPDC1, STC1, HYAL2, CAVIN1, TCF4, BCAM, IFITM2, STOM, MMRN2, ESAM, CALCRL, IFITM3, CNN3, CAVIN2, TGFBR2, IGFBP4, CD34, S1PR1, SOCS3, PECAM1, ACKR1, GJA1, CD59, SLC9A3R2, ITGA6, NNMT, PDLIM1, APP, MTUS1, TSPAN7, ADAMTS9, C2CD4B, CDH5, ADAMTS1, APOLD1, MEF2C, LMO2, YBX3, ELK3, TIMP3, CYYR1, CD93, TFPI, THBD, RNASE1, SPTBN1, HLA-DRB5, ITGA5, SOX18, GRASP, CLU, ID3
fibroblast	DCN, CCDC80, IGFBP6, COL1A2, MGP, COL6A2, C1R, PLAC9, FBLN1, CFD, PCOLCE2, SERPING1, LUM, SERPINF1, C1S, MFAP5, MFAP4, SOD3, COL6A1, PH6, OGN, GSN, CLU, SPARCL1, LTBP4, COL6A3, MMP2, EFEMP1, C3, SFRP2, SCARA6, ADH1B, GPX3, SLIT2, CALD1, TIMP2, COL3A1, SPARC, CTSK, FBN1, SPON2, PMP22, PCOLCE, CCN1, PLPP3, OLFML3, EGR1, TFPI, FBLN5, ACKR3, CD34, FBLN2, DPT, RARRES2, APOD, IGFBP5, LRP1, CCN2, ABI3BP, FGFR1, ISLR, GPNMB, AEBP1, CCN5, TIMP1, MXRA8, SOCS3, MFGE8, NNMT, IGFBP7, CEBPD, EMP1, CD248, MYC, C11orf96, AC080038.1, NFIA, FSTL1, TIMP3
pericyte cell	RGS5, PPP1R14A, BGN, TPM2, MYL9, IGFBP7, CALD1, MFGE8, COL4A1, NDUFA4L2, COL4A2, C11orf96, ACTA2, MGP, CAV1, PDGFRB, COX7A1, SOD3, COL18A1, CPE, SPARC, COL3A1, COL6A2, CAVIN3, CSRP2, CRIP2, LHFPL6, COX412, WFDC1, COL1A2, A2M, TPM1, PDGFA, TGFB111, COL6A1, SPARCL1, MEF2C, FAM162B, HIGD1B, HES4, SELENOM, IGFBP2, CNN3, FN1, FILIP1L, MAP1B, LBH, EHD2, CRYAB, TPPP3, EPS8, IFITM3, PCOLCE, GJA4, CCDC102B, PTP4A3, MY01B, NR2F2, TINAGL1, PLAC9, RRAS, CYGB, NREP, MYH11, RAMP1, AP002956.1, PLXDC1, RBPMS, SERPING1, ITGA1, LAMA4, PTMS, ACTN1, DSTN
schwann cell	NRXN1, CRYAB, GPM6B, S100B, CDH19, SCN7A, MAL, ANGPTL7, LGI4, CHL1, MPZ, GFRA3, PLP1, CADM1, MATN2, SEMA3B, ZEB2-AS1, ANK3, PMP22, AC005747.1, TMEM176B, SPARC, VWA1, PDGFA, CD9, IGFBP7, CLU, SPARCL1, FGL2, RH0B, PRNP, EPB41L2, NDRG2, CNN3, SAMHD1, PDK4, ZEB2
smooth muscle cell	CNN1, ACTG2, PCP4, DES, MYH11, PPP1R14A, TPM2, ACTA2, MYL9, SMTN, FHL1, CSRP1, MYLK, CKB, ECRG4, RAMP1, ACTC1, SORB51, TPM1, TGFB1I1, SPARCL1, PALLD, TAGLN, PDLIM3, CRYAB, CAV1, SYNPO2, SYNM, SORBS2, TNS1, HSPB6, SLMAP, RBPMS, FERMT2, SELENOM, PSD, NEXN, COXTA1, LIMS2, PTGS1, PDLIM7, CARMN, ACTN1, FN1, ACO2868.1, VWA1, CALD1, AF001548.1, MAP1B, COL6A1, LPP, LMOD1, SVIL, FLNA, PGM5, NIBAN1, PKIG, DSTN, FXYD6, CFL2, PITX1, CAVIN1, DMD, PGM5-AS1, FLNC, SLC25A4, ALDH1B1, FBX032, RBPMS2, HSPB8, LM03, TNNT2, RBF0X3, DIXDC1, KANK2, TGM2, RRAS, RARRES2, COL4A2, ILK, VCL, CLU, IGFBP7, NFIA, PPP1R12A, COL6A2, NME4, NUPR1, TCEAL4, PLEKH01, AD000090.1
b cell	IGHM, CD79A, CXCR4, IGKC, CCR7, CD37, VPREB3, ARHGAP24
dc1	LGALS2, CLEC9A, DNASE1L3, WDFY4, IDO1, XCR1, HLA-DOB, RAB7B, SERPINF2, S100B, NAPSB, BATF3, P2RY6, WFDC21P, C1off54, SLAMF8, CPVL, CADM1, ASB2, IRF8, SHTN1, PADI2, LYZ, C1orf162, NAAA, HCK, SPI1, SLAMF7, LY86, VMO1, HLA-DQB1, PLEK, ANPEP, FGD2, HLA-DQA1, MPEG1, AIF1, MNDA, CLEC7A, HLA-DR6, HLA-DPB1, PTPRE, HLA-DPA1, LGALS9, RGS10, HLA-DMB, HLA-DRA, FGL2, HLA-DRB1, HLA-DMA, CD86, CPNE3, SMCO4, SNX3, RAB32, CXCL16, BCL2A1, PPT1, BASP1, LST1, GCA, ITGAX, RNASE6, AP1S2, ADA2, TAP1, RGCC, TGFBI, ITGB2, PARVG, AC004687.1, SELPLG, LSP1, COTL1, SERPINB9, CD40, CD83, CTSZ, BID, SEMA4A, GNA15, ASAP1, C20orf27, SAMHD1, UNC119, CCDC88A, PLEKHO1, RGS19, PYCARD, PDLIM7, SERPINB1, ATG3, LIMD2, LCP1, EVI2B, SEPTIN6, TYMP, HLA-DRB5, LSM6, FNBP1, CCND1, PAK1, FAM49B, TNFAIP8, WAS, HCLS1, CD48, NFKBID, TMEM14A, PRCP, PSMB9, SNX10, PPA1, UCP2, DUSP4, DNAJC4, ICAM3, CST7, RNH1, ANXA6, PSME2, NET1, SERPINF1, AC101618.1, GLIPR1, NME4, RNASET2, SGK1, DBNL, MRPL23, VASP, TPP1, FMNL1, ACTN1, CKLF, CFL1, CYB5R3, RHOG, CORO1A, SYNGR2, GPR183, LTB, MZT2A, CAP1, CDK2AP2, GNG5, SERPINB6, GMFG, GPSM3, CRIP1, GABARAP, PLAUR, AP251, DUSP2, CTSS, HLA-F, FGGRT, NR4A2, LAPTM5, CD53, RGS2, GTF3C6, BUD23, CD37, MSN, CD52
dc2	LST1, AIF1, HLA-DQB1, TYROBP, FCER1A, HLA-DQA1, CD1C, FCER1G, HLA-DMB, MS4A6A, C1orf162, SPI1, CLEC10A, GPR183, CD86, NAPSB, JAML, HLA-DPB1, HLA-DMA, HLA-DRB6, LYZ, CD1E, PKIB, LY86, HLA-DRB1, HLA-DPA1, CPVL, RNASE6, MNDA, LGALS2, IGSF6, HCK, HLA-DRA, HLA-DQA2, HLA-DQB2, PLD4, FCGR2B, CALHM6, CXCL16, COTL1, NR4A3, OLR1, CLEC7A, ITGB2, AXL, RGS10, BCL2A1, LGALS9, PAK1, PLAUR, AP1S2, TYMP, CD83, LSP1, ALOX5AP, YWHAH, EVI2B, FAM49B, RGS1, PLSCR1, RGS2, PYCARD, CST7, GPSM3, MACROH2A1, RNASET2, HCLS1, BASP1, CD53, SAMSN1, CORO1A, LAPTM5, CXCR4, GMFG
macrophage	AIF1, C1QC, C1QA, C1QB, TYROBP, FCER1G, FCGR2A, MS4A7, MS4A6A, CD14, APOE, SPI1, APOC1, MSR1, FCGR3A, MS4A4A, TGFBI, CSF1R, LST1, CTSZ, HLA-DQA1, SPP1, CD163, CTSB, DAB2, HLA-DPB1, ADAP2, HLA-DMB, TREM2, ITGB2, LAPTM5, LGMN, CD4, CCL3, RNF130, HLA-DQB1, C1orf162, OLR1,
mast cell	TPSB2, TPSAB1, CPA3, IL1RL1, RHEX, LTC4S, GATA2, FCER1G, CTSG, HDC, VWA5A, KIT, MS4A2, CLU, ALOX5AP
monocyte	AIF1, TYROBP, FCER1G, LST1, LYZ, S100A8, S100A9, SERPINA1, BCL2A1, PLAUR, IL1B, C5AR1, CTSS, G0S2, FCN2, MNDA, SPI1, OLR1, SOD2, TYMP, COTL1, MS4A6A, CSTA, SAMSN1, MS4A7, EREG, CD14, C1orf162, CLEC7A, ITGB2, SRGN, LAPTM5 LAMP3, CCL22, CCL19, NCCRP1, EBI3, CCL17, TVP23A, AOC1, IDO1, CD200, FSCN1, CFP, CCR7, WFDC21P, RASSF4, TMEM176A, CD86,
mreg dc	POGLUT1, BIRC3, CDE19, NCORF, LEIS, CDE17, TVF25A, ROET, IDOT, CDE0, TSCH7, GF7, CGF7, CGF7, KN3D47, TMELMTAG, CDE0, POGLUT1, BIRC3, CD40, IL411, TMEM176B, BCL2A1, TBC1D4, RAMP1, NRP2, CD83, MIR155HG, GPR183, LSP1, HLA-DQA1, SAMSN1, IRF4, BASP1, TYROBP, HLA-DQB1, LAD1, IL7R, TXN, KDM2B, HLA-DPB1, MARCKSL1, HLA-DQA2, KYNU, HLA-DRA, NUB1, RFTN1, DUSP5, SYNGR2, ANXA6, RELB, MTHFD2, MGLL, RGS1, LGALS9, HLA-DPA1, TYMP, ERICH1, CSTA, ID2, GRSF1, SPI1, NABP1, CRIP1, KIF2A, HLA-DRB1, PPA1, VOPP1, CFLAR, SOCS1, NFKB1, HMGN3, TNFAIP8, COTL1, CTSH, STK4
	G0S2, CSF3R, TREM1, LUCAT1, S100A8, IL1R2, SLC11A1, NAMPT, CXCL8, BCL2A1, S100A9, IVNS1ABP, TPI1, ZFAS1
	NKG7, GNLY, CCL5, CTSW, CST7, GZMB, TYROBP, PRF1, CD7, GZMA, HCST, KLRD1, CD247, TRDC, PTPRC, KLRC1, CCL4 MZB1, DERL3, CD79A, FKBP11, JCHAIN, IGHG3, TNFRSF17, IGLC2, ITM2C, CD27, PIM2, IGHA1, SEC11C, ANKRD28, SLAMF7, PRDX4, IGHG1, JSRP1, XBP1, IGLC3, IGKC, POU2AF1, CD38, IGHG2, ST6GAL1, TPD52, SPCS3, SDF2L1, ANKRD36BP2, DNAJB9, SPAG4, EAF2, ERLEC1, IGHA2, CRELD2, RNU2-63P, TXNDC15, DTNB, TXNDC5, HERPUD1, KLF13, IGHGP, PRDM1, IGHG4, IGLV3-1, PDE4B, PLPP5, ISG20, GLRX, SSR3, RN7SL2, RN7SL1, NUCB2, MANF, CYTOR, ICAM3, CFLAR, SELENOS
	PLAC8, PLD4, SCT, LILRA4, LRRC26, PTCRA, SPIB, TCL1A, SMPD3, IRF4, NAPSB, LILRB4, DERL3, GZMB, MZB1, IRF7, BCL11A, JCHAIN, MYBL2, IRF8, C12orf75, GPR183, CLIC3, LDLRAD4, SELL, EGLN3, ITM2C, NR4A3, ALOX5AP, THEMIS2, CXCR3, RNASE6, TSPAN13, OPN3, CCDC50, SLC15A4, PPP1R14B, SEC61B, AC004687.1, AREG, FCER1G, DUSP5, SLC7A5, TYROBP, CXCR4, HERPUD1, NR3C1, GNA15, CREM, SERPINF1, ZC3HAV1, N4BP2L1, RGS1, RGS2, TCF4, MS4A6A, HLA-DRB1, PIM2, HLA-DRA, NPC2, LTB, PLP2, HLA-DPB1, ZNF331, CD83, RNASET2, HLA-DMA, SRGN, YPEL5, CTSB, HLA-DPA1, CD37, RPL7, UCP2, NR4A2, HLA-D0B1, LSP1
	CD2, CD3D, LTB, IL7R, IL32, CD52, TRAC, TRBC2, CD3E NKG7, CD3D, CCL5, GZMA, TRBC2, CD2, TRAC, CD3G, CD8A, CTSW, LINC01871, HCST, CD3E, CST7, CD52, CD7, IL32, GZMB, PTPRC, CCL4,
t cd8	NNGF, CD3D, CCE3, GZMA, TRBCZ, CD2, TRAC, CD3G, CD3A, CTSW, LINCOT871, HCS1, CD3E, CS17, CD52, CD7, IE32, GZMB, PTPRC, CCL4, CORO1A, TRGC2, IL2RG, ALOX5AP, LCK, RGS1, TRBV28, RAC2, KLRD1
t cell cycle	C12of7, 5, CTSW, PSMB9, CD247, CRIP1, MCM7, HMGB1P5, NUD11, DU1, ANP32E, TNFRSF18, TBC1D10C, SKA2, DER, P1PN22, DDX39A, PCED1B-AS1, IL2RG, GNG2, CKLF, CALM3, CBX5, SLA, CCL5, LCP1, BUB3, PSMB8, OXNAD1, DNMT1, CCDC167, ANP32B, TUBBP1, PSIP1, IL32, RPA3, HCST, CYTOR, PTPRC, LSP1, GMFG, SEPTIN1, CD52, ANXA6, RANBP1, HOPX, PAXX, CST7, LBH, ICAM3, ITM2A, IFI16, HLA-F, EVL, ACAP1, ALOX5AP, CKS2, LIMD2, FYN, CBX3, NAP1L4, MZT2A, MT2A, IFI27L2, COTL1, CD53, HCLS1, STK17B, ID2, RGS1, SAMSN1, FXYD5, LAPTM5
treg	LTB, CD3D, TIGIT, IL32, TNFRSF4, TRAC, CD2, TNFRSF18, TRBC2, SPOCK2, CTLA4, CD27, CD3E, FOXP3, CD7, BATF, IL2RG, TRBC1, IL2RA, CARD16, TBC1D4, CORO1A, LCK, RGS1, IL7R, PTPRC, CD3G, ICOS, RAC2, PCED1B-AS1, CYTOR, CD52

Cluster ID	Cell count:
normal epithelial	3458
HLA-E-bright tumor	5461
HLA-E-dim/neg tumor	9256
endothelial cell	3135
fibroblast	7630
pericyte cell	1963
schwann cell	186
smooth muscle cell	660
b cell	3675
dc1	80
dc2	599
macrophage	5271
mast cell	1015
monocyte	1871
mreg dc	150
neutrophil	519
nk cell	2580
plasma cell	1301
plasmacytoid dendritic cell	171
t cd4	8548
t cd8	5491
t cell cycle	629
t reg	1675
	65,324

Extended data Table S4: Annotated scRNAseq clusters with numbers of cells



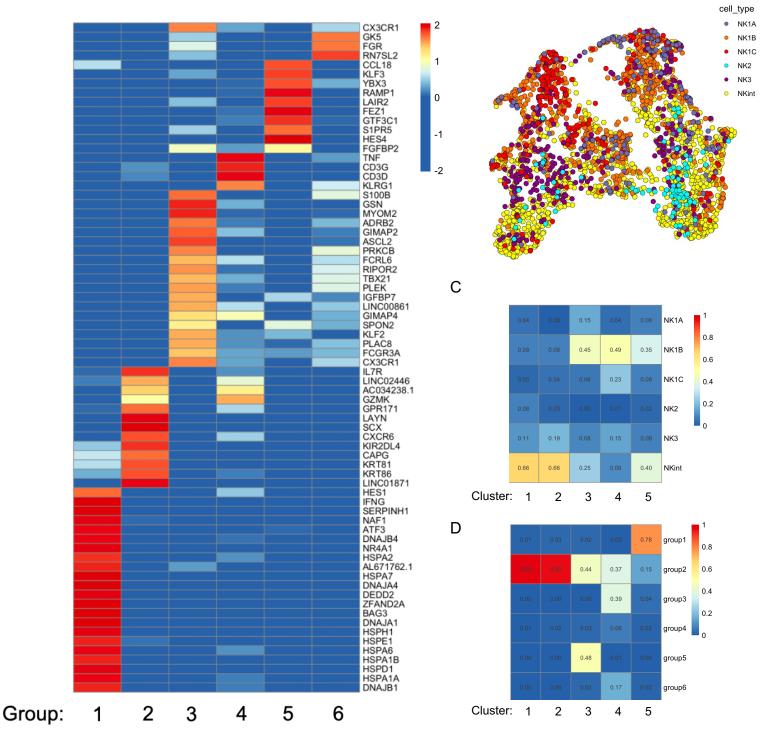
В

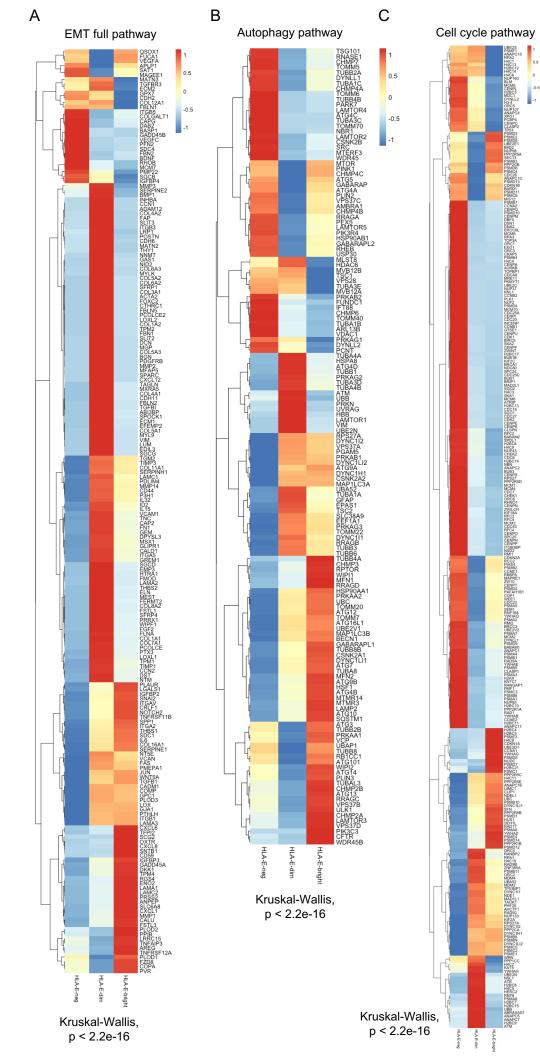


Extended data Figure S1: Cellular sources of IFN-y in NMIBC by scRNAseq

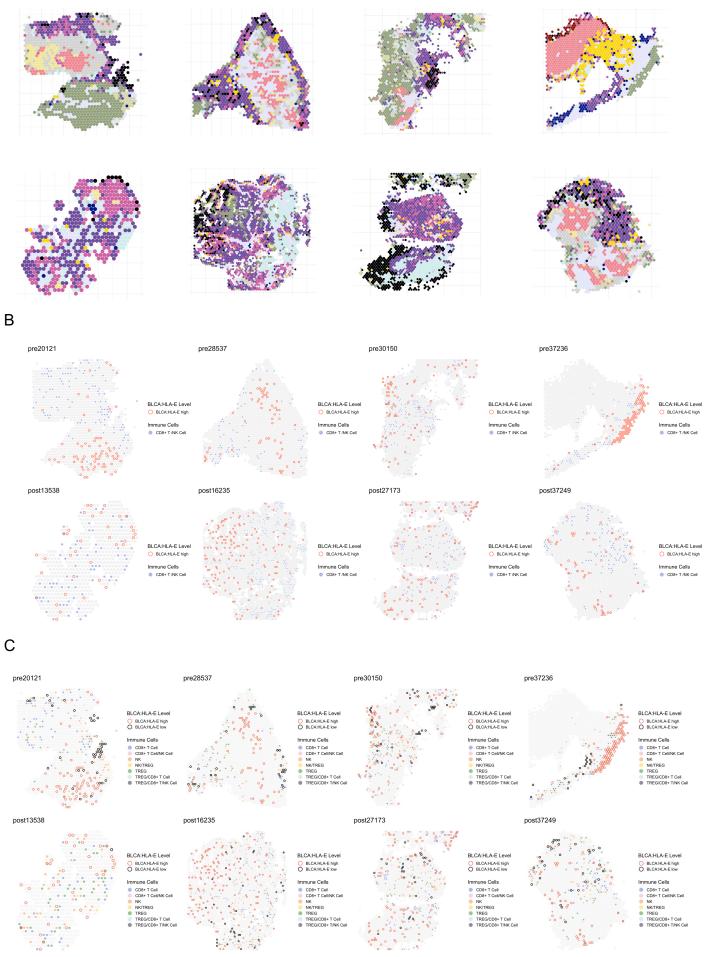
А

В

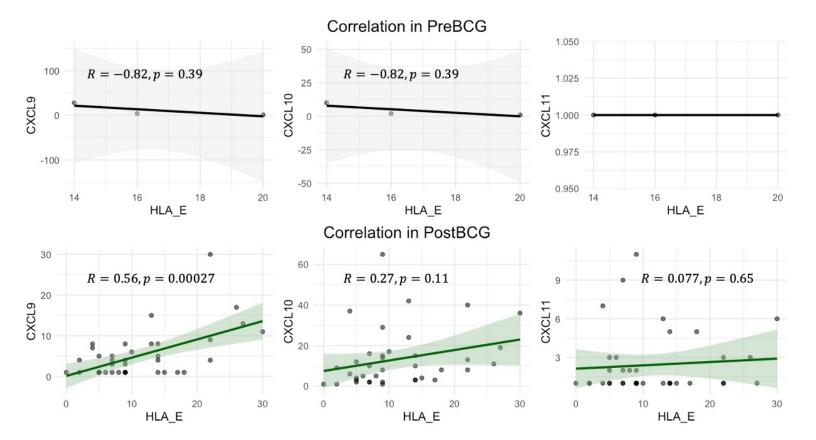




Extended Data Fig. S3



Extended Data Fig. S4



	Clinical Cohort Characteristics				
	HTG	OLINK Urine (Sinai)	Single Cell	Spatial	Cytof
n samples, patients	36, 27	42, 26	7, 6	20, 9	16, 16
Female	4	2	0	0	1
BCG Naïve	19	26	2	4	0
BCG Unresponsive	17		4	5	16
Median Age	64	69.5	66.9	70.6	68.5
Median Months to Recurrence	2.9	2.1	2.3	1.7	2.73
Median Months to Progression	6.7		14.3	23.28	4.43
Stage at Collection					
CIS	4			_	_
Tis/Ta	5	13		2	8
T1	10	14	4	6	5
T2					2
Τ3			2		0
T4					1

Table 1.